IEKP-K17/2003-19

A Front-End electronics configuration system for CMS subdetectors and Observability of an MSSM Higgs boson in the 4-b final state

Zur Erlangung des akademischen Grades eines
DOKTORS DER NATURWISSENSCHAFTEN
von der Fakultät für Physik der Universität (TH)
Karlsruhe

genehmigte

DISSERTATION

von

DEA Philippe Gras
aus Straßburg

Tag der mündlichen Prüfung: 18.07.2003

Referent: Prof. Dr. Thomas Müller, Institut für Experimentelle Kernphysik

Korreferent: Prof. Dr. Daniel Denegri, Commission à l’Energie Atomique - Département d’Astrophysique, de Physique des Particles, de Physique Nucléaire et de l’Instrumentation Associée, Gif-sur-Yvette, France

Contents

Introduction

The Standard Model explains the mass of the particles with the Higgs mechanism. This mechanism requires the existence of at least one Higgs boson. Nevertheless it does not predict the mass of this boson. The Standard Model, which has been confirmed experimentally with an amazing accuracy, needs to be extended in order to describe the physics beyond $\sim 1\,TeV$ energy. Its Minimal Supersymmetric extension (MSSM) contains five Higgs bosons: two CP-even (h, H), one CP-odd (A) and two charged bosons ($H^{\pm}$). In the MSSM, the coupling with $b\bar{b}$ quark pairs of the pseudoscalar Higgs boson A and of the heavier neutral scalar Higgs boson H is enhanced by the vacuum expectation value ratio, $\tan\beta$. At the Large Hadron Collider (LHC), for $\tan\beta \gtrsim 10$, because of the enhancement of the $A/H\,b\,\bar{b}$ coupling, the four-b final state is the dominant A/H Higgs boson channel. Nevertheless the backgrounds for this channel are also considerable and a detailed study is required to determine if the signal can be seen on top of them. Large A boson mass values ($m_A \gtrsim 300\,GeV$), for which a substantial $(m_A, \tan\beta)$-region is not covered by any channel yet foreseen at the LHC collider, is particularly interesting to look at.

The data that will be collected by the Compact Muon Solenoid (CMS) experiment will depend on the parameters of its Front-End (FE) readout electronics. Therefore the history of the readout electronics configuration must be stored. Moreover when the data will be analysed, one should be able to retrieve easily the FE parameter values that were used when the data were produced. Because of the huge number of electronics channels of the CMS detector, 54.5 millions channels, the amount of parameters to store is substantial. For those reasons the configuration system of the FE electronics must be designed with special care in order to optimise the storage space and to ease data retrieving. The configuration of the FE electronics must be done online, for instance at the beginning of a run. The control of this configuration system must be integrated in the general control system of the experiment. The FE electronics system which has been designed has been tested during a beam test of the Tracker subdetector. Further developments for the control of this beam test have also been performed.

After a review of the Standard Model and of its Minimal Supersymmetric extension, the CMS experiment at the LHC collider and the prospect in CMS of a Higgs discovery will be introduced. The configuration system of CMS readout electronics will then be presented. Finally the observability in CMS of A/H Higgs bosons in the four-b final state [1, 2] will be studied.

Chapter 1

The Standard Model and its Minimal Supersymmetric extension

1.1 The Standard Model

The idea that matter is composed of indivisible elementary parts originated from Leucippus (V^{th} century BC). His disciple Democritus of Abdera (c. 460–c. 370 BC) called those elementary parts "atomos", which means "indivisible." In 1900, Max Planck extended this idea to light, stating that light is made of elementary particles called photons. Quantum mechanics was born. Every measurable quantity is a multiple of an elementary unit called a quantum.

In the 1960's a model, namely the "Standard Model" (SM), describing the components of matter and explaining the forces (also called "interactions") was introduced . In this model each interaction is mediated by a particle, called a gauge boson[1]. They are three kinds of elementary particles: quarks, leptons and gauge bosons; in addition the SM is expected to have one spin-0 boson, the Higgs, responsible for generating particle masses.

There are three families of leptons:

$$\begin{pmatrix} \nu_{e^-} \\ e^- \end{pmatrix} \quad \begin{pmatrix} \nu_{\mu^-} \\ \mu^- \end{pmatrix} \quad \begin{pmatrix} \nu_{\tau^-} \\ \tau^- \end{pmatrix} \quad \underbrace{\begin{pmatrix} 0 \\ -1 \end{pmatrix}}_{\text{electric charge}}$$

three families of quarks:

$$\begin{pmatrix} u \\ d \end{pmatrix} \quad \begin{pmatrix} c \\ s \end{pmatrix} \quad \begin{pmatrix} t \\ b \end{pmatrix} \quad \underbrace{\begin{pmatrix} +2/3 \\ -1/3 \end{pmatrix}}_{\text{electric charge}}$$

and the gauge bosons are:

$$\gamma \quad W^+ \quad Z^0 \quad g$$

[1]Boson comes from Bose-Einstein's statistics, those followed by integer-spin particles. On the contrary to Fermions (half-integer spin particles obeying Fermi's statistics), two bosons can be in the same state.

To each of these particles corresponds an antiparticle, the mirrored particle with an opposite charge. γ , Z^0 are their own antiparticles because they have a no charge and are invariant under space-inversion.

The quarks have never been observed as free particles and it is believed that it is to not possible to isolate them. This assumption is motivated by the nature of the interaction between quarks, called the strong interaction or QCD (Quantum Chromo-Dynamics). Indeed this force increases with the distance between the quarks. Trying to separate two coupled quarks will result in the creation of a new quark pairs, resulting in two coupled-quark pairs. The quarks can be depicted as the ends of a string, which is stretched; if the string breaks off there are two new ends. Most of the matter mass comes from the quarks. Quarks can couple in $q\bar{q}$ pairs to give particles called *mesons*. Mesons can be found in cosmic rays – and this is how the first ones were observed. Otherwise they are produced in accelerators, in many species, some, like pions, very numerously. Quarks can also couple in triplets to give *baryons*, for instance the proton is made of a u, u, d quark combination and the neutron is made of u, d, d.

The Standard Model includes three forces:

- electromagnetic interaction mediated by the photon, γ (responsible for electric and magnetic forces) of spin 1 and mass zero
- weak interaction mediated by the weak gauge bosons, W^+, W^-, Z^0 (responsible for β–decay). Those bosons have a spin 1 and they are massive ($80 \sim 90\,GeV$)
- strong interaction mediated by gluons (8), g (responsible for nucleus cohesion). They have a spin 1 and are massless. They are carrying colour.

The two first interactions form the "electroweak" interaction. The Standard Model does not include gravitation.

By unifying Einstein's (1879-1950) special relativity and quantum mechanics P. A. M. Dirac (1902-1984) created the *Quantum field Theory*. Dirac has described the electron motion with a 4-component field, called spinor.

A particle can be defined by its physical properties, such as its electrical charge, but also its leptonic charge, baryonic charge, etc.. At the time t, the small region around a point $\vec{x}$ will contain some electrical charge, some leptonic charge some baryonic charge, etc.. Therefore a charge density can be defined for each space point. Moreover these charges can be expressed as a function of the 4 variables, x, y, z, t. Quantum field equations are actually expressed in terms of the "square root" of this function: "square root" means here that if $\rho(\vec{x}, t)$ is the density function, its "square root" is a function $\varphi(\vec{x}, t)$ such that $\rho \equiv \varphi\varphi^*$. It should be noted here, that $\varphi(\vec{x}, t)$ is defined up to a phase $\alpha(\vec{x}, t)$, which has no physical meaning. Such a phase is called "local gauge", local means that it depends on the $(\vec{x}, t)$ coordinate. The function $\varphi(\vec{x}, t)$ is called a field. For a proper understanding of quantum physics, the Fourier transform of $\varphi(\vec{x}, t)$ must be introduced. This Fourier transform $\psi(\vec{k}, t)$ is then interpreted as an operator, this process is called second quantisation: see for instance [3] for more details.

One feature of Einstein's relativity theories (both special and generalised) is the derivation of gravity properties from the assumption of the independence of the physics laws with respect to the frame of reference: theory is not changed by a coordinate transformation. Properties of the other interactions can also be derived by independence from transformation, called symmetries. Furthermore, the German mathematician Amalie Emmy Noether (1882-1935 [4]) has shown that to each symmetry invariance corresponds the conservation of a physical quantity. For instance, the conservation of the momentum corresponds to the invariance under space translations.

The three interactions and their corresponding gauge bosons derive from the invariance under local gauge transformations. A particle is defined by a few quantum numbers which are conserved. According to Noether's theorem, the conservation of each of these quantum numbers results from a symmetry. If a symmetry is not exact then the corresponding quantum number is no more absolutely conserved. It is believed that the physics is described by a symmetry group and that particles can be seen as unitary representations of this group[2].

Let's define $SU(n), n \geq 2$ as the multiplicative group of unitary[3] $n \times n$ matrices with a determinant equal to 1 [5,6]. We will also define $U(1)$ as the set $\{e^{i\theta}, \theta \in [0, 2\pi[\}$.

Fermions can be described by a field with four components called spinor.

The strong interaction is described by a SU(3) group, the electroweak interaction by a $SU(2) \times U(1)$ group. The Standard Model is then said to obey the symmetry:

$$G = SU(3)_C \times SU(2)_L \times U_Y(1) \tag{1.1}$$

As for the physical optics and fluid mechanics, the principle of least action can be used to describe the particle physics. The formalism developed by the French mathematician Lagrange (1736-1813 [7]) for the classical mechanics shows all its power when applied to particle physics. The physics can be formulated by a function called the Lagrangian (more correctly Lagrangian density) $\mathcal{L}$, which will have the symmetries of the physics, and a unique equation:

$$\frac{\partial}{\partial x_\mu}\left(\frac{\partial \mathcal{L}}{\partial(\partial\phi/\partial x_\mu)}\right) - \frac{\partial \mathcal{L}}{\partial \phi} = 0 \tag{1.2}$$

Equation name	Description	Equation	Lagrangian, $\mathcal{L}$
Maxwell	describes electromagnetic fields	$\partial_\mu F^{\mu\nu} = j^\nu$	$-\frac{1}{4}F_{\mu\nu}F^{\mu\nu} - j^\mu A_\mu$
Klein-Gordon	describes motion of free spin-0 particles	$(\partial_\mu\partial^\mu - \frac{1}{2}m^2)\phi = 0$	$\frac{1}{2}(\partial_\mu\phi)(\partial^\mu\phi) - \frac{1}{2}m^2\phi^2$
Dirac	describes motion of free spin-$\frac{1}{2}$ particles (e.g. an electron)	$(i\gamma^\mu\partial_\mu - m)\psi = 0$	$i\overline{\psi}\gamma^\mu\partial_\mu\psi - m\overline{\psi}\psi$

Table 1.1: Equivalent Lagrangians of selected physics equations. Inserting the Lagrangian into Euler-Lagrange equation (1.2) gives the original equation.

Table 1.1 shows the Lagrangian corresponding to some standard physics equations. These three simple Lagrangians can be used to interpret the terms of more complex Lagrangians.

[2] A d-dimensional unitary representation of a group G is a homomorphism from G to the group of unitary matrices of dimension $d \times d$. The representation Γ is said irreducible if the matrices $\Gamma(T)$, $T \in G$ cannot be decomposed into submatrices of the form $\begin{pmatrix} \Gamma_{11}(T) & \Gamma_{12}(T) \\ 0 & \Gamma_{22}(T) \end{pmatrix}$.

[3] A matrix is said to be unitary if $A^+A = 1$, with A^+ the hermitian adjoint of A, $A^+ = (A^*)^T$.

1.1.1 Deriving interactions from gauge symmetries

In 1954 C. N. Yang and R. L. Mills extended electromagnetism local gauge invariance formalism to strong interaction [8]. By requiring a non-abelian local gauge invariance of the Lagrangian, they were lead to introduce a new field.

Requiring a local gauge invariance of the free Lagrangian,

$$\mathcal{L} = i\bar{\psi}\gamma^{\mu}\partial_{\mu}\psi \tag{1.3}$$

leads us to introduce a field, $F^{a}_{\mu\nu}$ and change the Lagrangian expression to:

$$\mathcal{L} = \bar{\psi}\gamma^{\mu}(i\partial_{\mu} - gT_{a}F^{a}_{\mu})\psi \quad \underbrace{-\frac{1}{4}F^{a}_{\mu\nu}F^{\mu\nu}_{a}}_{\substack{\text{gauge field} \\ \text{kinematic energy}}}$$

with:

$$F^{a}_{\mu\nu} = \partial_{\mu}F^{a}_{\nu} - \partial_{\nu}F^{a}_{\mu} - g f^{a}{}_{bc}F^{b}_{\mu}F^{c}_{\nu} \tag{1.4}$$

and T_a, the generator of the local gauge symetry group.

The field F^{a}_{μ} can be interpreted as the field of a boson. This boson is called "gauge" boson. It is the mediator of the interaction between the fermions.

1.1.2 Quantum Chromodynamics

As it has been already mentioned in section 1.1, the proton is made of quarks u,u,d. The Δ^{++} baryon, discovered by Fermi and its collaborators in 1951 [9], is made of a quark combination u,u,u, where the three quarks have a spin $\frac{1}{2}$. The Pauli principle would be violated if no additional quantum number is introduced to distinguish the three up quarks of the Δ^{++} baryon. This quantum number is called colour and has three possible values identified by the "primary colour" names red (R), green (G) and blue (B). However only one state of the proton is observed, therefore there must exist some rule forbidding 5 of the 6 possible colour combinations of proton quarks. This can be achieved by requiring invariance under rotation in R,B,G space. The proton is then a linear combination of the $u_R u_G d_B$, $u_B u_R d_G$, $u_G u_B d_R$ states. Pions, which are made of a quarks-antiquark pair are linear combination of $q_R\bar{q}_R$, $q_G\bar{q}_G$, $q_B\bar{q}_B$ states.

The theory describing strong interactions has been called *Quantum Chromodynamics*, or shortly *QCD*, after the quantum number name, "colour". Strong interactions are mediated by gluons.

By the mechanism described in section 1.1.1, requiring $SU(3)$ symmetry of the Lagrangian introduces a gauge field $F^{a}_{\mu\nu}$, which will be denoted here as $G^{a}_{\mu\nu}$ ("G" stands for gluon field) and gives the Lagrangian:

$$\mathcal{L}_1 = \bar{q}i\gamma^{\mu}\partial_{\mu}q - g(\bar{q}\gamma^{\mu}T_a q)G^{a}_{\mu} - \frac{1}{4}G^{a}_{\mu\nu}G^{\mu\nu}_{a}$$

where $G^{a}_{\mu\nu} \equiv F^{a}_{\mu\nu}$ is given by (1.4). T_a is the generator of the $SU(3)$ group. q is the quark colour triplet,

$$\begin{pmatrix} \psi_R \\ \psi_G \\ \psi_B \end{pmatrix}$$

1.1.3 Electroweak interaction

A particle which travels in the direction of its spin is said to have a positive helicity or, in other words, to be right-handed. A particle which travels in the opposite direction is said to have a negative helicity or to be left-handed. In the massless approximation only left-handed neutrinos and right-handed antineutrinos can be involved in weak interactions. $P_R \equiv \frac{1}{2}(1+\gamma^5)$ (resp. $P_L \equiv \frac{1}{2}(1-\gamma^5)$) is the right-handed (resp. left-handed) projector. The helicity concept can be extended to massive particles. This extension is called chirality: the positive-chirality, or right-handed, component of a massive particle u is $P_R u$. Negative-chirality component is defined similarly with P_L. More generally only the left-handed component of a particle takes part in weak interactions with an exchange of electric charge (charged current interactions).

A. Salam, S. Weinberg and S. L. Glashow show that electromagnetic and weak interactions can be obtained by requiring invariance of the fermion field under a transformation of $SU(2)_L \times U(1)$, where $SU(2)_L$ is the set of $SU(2)$ transformation acting only on the left-handed part of the field [10–12].

From the point of view of electroweak interactions, Leptons and quarks can then be grouped in left-handed doublets and right-handed singlets of the $SU(2)$ group:

$$\begin{pmatrix} \nu_l \\ l \end{pmatrix}_L \text{ and } l_R \qquad \text{for leptons, } l = e, \mu, \tau$$
$$\begin{pmatrix} u_i \\ d_i \end{pmatrix}_L, \; u_{iR} \text{ and } d_{iR} \qquad \text{for quarks, } u_i = u, c, t \quad d_i = d, s, b$$

By requiring $SU(2)_L \times U(1)$ invariance of the massless-fermion Lagrangian one obtains the following expression for the Lagrangian:

$$\begin{aligned} \mathcal{L}_2 \;=\; & \bar{\psi}_R \gamma_\mu (i\partial_\mu - \tfrac{g'}{2} Y B_\mu)\psi_R \\ + \; & \bar{\psi}_L \gamma_\mu (i\partial_\mu - \tfrac{g}{2}\vec{\sigma}\cdot\vec{W}_\mu - \tfrac{g'}{2} Y B_\mu)\psi_R \\ - \; & \tfrac{1}{4} B_{\mu\nu} B^{\mu\nu} \\ - \; & \tfrac{1}{4} F_{\mu\nu} F^{\mu\nu} \end{aligned} \tag{1.5}$$

with ψ_R (respectively ψ_L), the right-handed (respectively left-handed) component of the field and $\vec{\sigma} = (\sigma_1, \sigma_2, \sigma_3)$ the Pauli matrices:

$$\sigma_1 = \begin{pmatrix} 0 & 1 \\ 1 & 0 \end{pmatrix} \quad \sigma_2 = \begin{pmatrix} 0 & -i \\ i & 0 \end{pmatrix} \quad \sigma_3 = \begin{pmatrix} 1 & 0 \\ 0 & -1 \end{pmatrix}$$

This Lagrangian does not contain mass terms for fermions and bosons. Adding a $-\bar{\psi} m \psi$ term like in the free-fermion Lagrangian will lead to a Lagrangian which is not anymore gauge invariant. Furthermore it will not be anymore renormalizable, which means interactions cannot be calculated in perturbation theory. The mass can be introduced while keeping the Lagrangian renormalizable with the help of a scalar field and a so called Higgs mechanism.

1.1.4 Breaking the gauge symmetry: the Higgs mechanism

Boson masses will be generated by coupling the gauge bosons to a complex scalar field, denoted as ϕ, associated to a potential $V(\phi)$:

$$V(\phi) = \mu^2 \phi^\dagger \phi + \lambda(\phi^\dagger \phi)^2 \quad \text{with } \mu^2 < 0, \; \lambda > 0$$

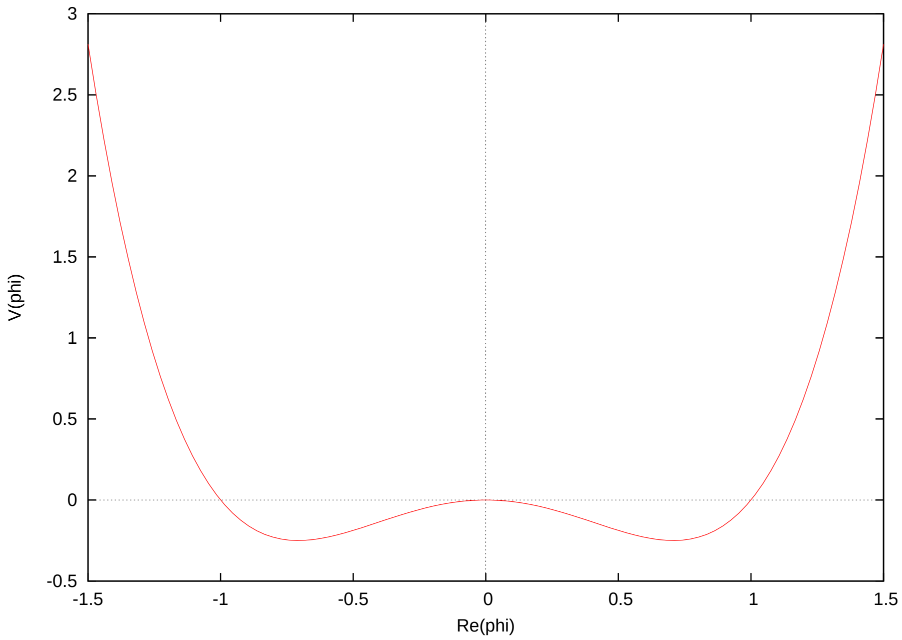

Figure 1.1: Higgs potential for a field of dimension two, $\phi \in \mathbb{C}$, $\lambda = 1$, $\mu^2 = -1$

Figure 1.1 shows what this potential looks like. This potential is invariant under $U(1)$ and $SU(n)$, $n \geq 2$ transformations. However, if this potential is developed about one of its minima, then the resulting development is no more symmetric. This is called spontaneous symmetry breaking.

The interaction with the $SU(2)_L \times U(1)$ gauge field will be included in the Lagrangian with the term,

$$(D^\mu\phi)^+(D_\mu\phi)$$

Therefore the following term is added to the Lagrangian:

$$\begin{aligned} \mathcal{L}_3 &= (\partial^\mu\phi + i\frac{g}{2}\vec{\sigma}\cdot\vec{W}^\mu\phi + i\frac{g'}{2}YB^\mu\phi)^+(\partial_\mu\phi + i\frac{g}{2}\vec{\sigma}\cdot\vec{W}_\mu\phi - \frac{g'}{2}YB_\mu\phi) \\ &\quad -V(\phi) \end{aligned} \tag{1.6}$$

Gauge invariance of $\mathcal{L}_3$ requires ϕ to be a multiplet of $SU(2)\times U(1)$. The simplest choice is to take an isospin doublet with weak hypercharge $Y = 1$:

$$\phi = \begin{pmatrix} \phi^+ \\ \phi^0 \end{pmatrix} \quad \phi^+,\ \phi^0 \in \mathbb{C}$$

The set of minima, $\{\phi|\phi^+\phi = -\frac{\mu^2}{2\lambda}\}$ of $V(\phi)$ is invariant under $SU(2)\times U(1)$ gauge symmetries. One minimum must be chosen for the development of the Lagrangian. We will take:

$$\phi_0 = \sqrt{\frac{1}{2}} \begin{pmatrix} 0 \\ \mathrm{v} \end{pmatrix}$$

with $\mathrm{v}^2 = -\frac{\mu^2}{\lambda}$. v is called *vacuum expectation value*. Actually another choice than 0 for charged component ϕ^+ of ϕ_0 would generate an undesirable mass for the photon [9].

ϕ can be parametrised around ϕ_0 by $\vec{\theta} = (\theta_1, \theta_2, \theta_3) \in \mathbb{R}^2$and $h \in \mathbb{R}$ by:

$$\phi = \sqrt{\frac{1}{2}} e^{i\vec{\sigma}\cdot\vec{\theta}(x)/v} \begin{pmatrix} 0 \\ \mathrm{v} + h(x) \end{pmatrix}$$

Developing this expression for small $\vec{\theta}$ and h shows that this expression is general enough to parametrise ϕ.

If the Lagrangian was not invariant under local gauge symmetry then $\vec{\theta}$ would turn out to be the fi elds of three massless particles, called Goldstone's bosons [13, 14]. Because of $SU(2)$ gauge invariance the $e^{i\vec{\sigma}\cdot\vec{\theta}(x)/\mathrm{v}}$ phase will cancel in the Lagrangian. What is called *the Higgs mechanism* [15–17] is precisely this cancellation, which discards the Goldstone bosons. We can therefore write without loss of generality:

$$\phi = \begin{pmatrix} 0 \\ \mathrm{v} + h(x) \end{pmatrix} \tag{1.7}$$

Introducing this parametrisation of ϕ in the expression (1.6) of $\mathcal{L}_3$ leads to:

$$\begin{aligned} \mathcal{L}_3 = & \frac{1}{2} \left| \partial_\mu \begin{pmatrix} 0 \\ \mathrm{v} + h(x) \end{pmatrix} + i\frac{g}{2}\vec{\sigma}\cdot\vec{W}_\mu \begin{pmatrix} 0 \\ \mathrm{v} + h(x) \end{pmatrix} + i\frac{g'}{2} B_\mu \begin{pmatrix} 0 \\ \mathrm{v} + h(x) \end{pmatrix} \right|^2 \\ & -\frac{1}{2}\mu^2 |\mathrm{v} + h(x)|^2 - \frac{\lambda}{4} |\mathrm{v} + h(x)|^4 \end{aligned}$$

with the notation $|A_\mu|^2 = (A_\mu)^+(A_\mu) = (A^\mu)^*(A_\mu)$ and $|\phi|^2 = \phi^+\phi$. After development of $\mathcal{L}_3$ and identifi cation of the terms like $\frac{1}{2} m_\psi |\psi|^2$ with mass terms of a particle described by the fi eld ψ, one fi nds that $\mathcal{L}_3$ contains the terms of the following particles:

Higgs boson	with fi eld $h(x)$			and mass	M_H	$=$	$\sqrt{2\lambda}$
W^+ boson	with fi eld W_μ^+	$=$	$\frac{W_\mu^1 - iW_\mu^2}{\sqrt{2}}$	and mass	M_{W^+}	$=$	$\frac{1}{2}\mathrm{v}g$
W^- boson	with fi eld W_μ^-	$=$	$\frac{W_\mu^1 + iW_\mu^2}{\sqrt{2}}$	and mass	M_{W^-}	$=$	$\frac{1}{2}\mathrm{v}g$
Z^0 boson	with fi eld Z_μ^0	$=$	$\frac{g'B_\mu + gW_\mu^3}{\sqrt{g^2+g'^2}}$	and mass	M_Z	$=$	$\frac{1}{2}\mathrm{v}\sqrt{g^2+g'^2}$
photon	with fi eld A_μ	$=$	$\frac{gB_\mu - g'W_\mu^3}{\sqrt{g^2+g'^2}}$	and mass	M_A	$=$	0

Fields Z_μ and A_μ are usually parametrised by:

$$\begin{aligned} Z_\mu &= -\sin\theta_w B_\mu + \cos\theta_W W_\mu^3 \\ A_\mu &= \cos\theta_w B_\mu + \sin\theta_w W_\mu^3 \end{aligned}$$

θ_W is called the Weinberg angle or weak mixing angle. For each of the three Goldstone bosons which were "absorbed" by the gauge, one degree of freedom was lost. On the other three gauge bosons have acquired a mass and have therefore a new degree of freedom, a longitudinal polarisation (which a massless particle does not have).

This Higgs mechanism can also generate the masses of the fermions.

1.1.5 Lepton masses

As for the weak gauge boson masses, the fermion masses can be generated by coupling their fields with the Higgs field. This coupling can be written in the following term, which must be added to the Lagrangian:

$$\mathcal{L}_4 = -G\,[\bar{L}\phi R + \bar{R}\phi L]$$

where ϕ is the Higgs field. R denotes the right-handed particle (singlet), $\bar{R}$ its antiparticle. L denotes the left-handed particle doublet, $\bar{L}$ the doublet of their antiparticle. G is the coupling constant of the singlet R with the doublet L. Let's take the example:

- $R = e_R$
- $L = \begin{pmatrix} \nu_e \\ e \end{pmatrix}_L$

$$\mathcal{L}_4 \quad = \quad -G_e\left[\begin{pmatrix} \bar{\nu}_e & \bar{e} \end{pmatrix}_L \phi e_R + \bar{e}_R \phi \begin{pmatrix} \nu_e \\ e \end{pmatrix}_L\right]$$

We obtain after replacing ϕ by its development (1.7):

$$\mathcal{L}_4 \quad = \quad -\frac{G_e}{\sqrt{2}}v(\bar{e}_L e_R + \bar{e}_R e_L) - \frac{G_e}{\sqrt{2}}\bar{e}_L h(x) e_R - \frac{G_e}{\sqrt{2}}\bar{e}_R h(x) e_L \tag{1.8}$$

Using the projector properties, $P^2_{L(R)} = P_{L(R)}$, $\bar{P}_{L(R)} = P_{R(L)}$ and $P_L + P_R = Id$, it can be easily shown that:

$$\bar{e}e = \bar{e}_L e_R + \bar{e}_R e_L$$

Therefore we recognise in the first $\mathcal{L}_4$ term a spin-$\frac{1}{2}$ free particle mass term (see Table 1.1 on page 5). We have generated the electron mass:

$$m_e = \frac{G_e}{\sqrt{2}}$$

Note that the theory does not predict G_e, therefore m_e stays a free parameter of the Standard Model. The second and third terms of (1.8) correspond to the coupling of the electron to the Higgs boson. Nevertheless this coupling is quite weak and negligible compared to the coupling of W bosons to the Higgs.

1.1.6 Quark masses:

The now well-known procedure can be used to produce the quark masses. While no mass was generated for the upper component of the lepton doublet, the neutrino, mass must be generated for the upper part of the quark doublet. For this purpose, the Lagrangian must also be developed about

$$\phi = \begin{pmatrix} v \\ 0 \end{pmatrix}$$

We then obtain (see for instance [18] for a detailed calculus development):

$$\mathcal{L}_5 = -G_d^{ij}\begin{pmatrix} \overline{u}_i & \overline{d}'_i \end{pmatrix}_L \begin{pmatrix} v+h(x) \\ 0 \end{pmatrix} d_{jR} - G_u^{ij}\begin{pmatrix} \overline{u}_i & \overline{d}'_i \end{pmatrix}_L \begin{pmatrix} 0 \\ v+h(x) \end{pmatrix} u_{jR} + h.c.$$

This Lagrangian is called *Yukawa Lagrangian.* The doublet $\begin{pmatrix} u_i & d'_i \end{pmatrix}$ is an electroweak eigenstate, which is related to the mass eigenstates by the 3×3 CKM matrix [19–21]:

$$\begin{pmatrix} d' \\ s' \\ b' \end{pmatrix} = V_{CKM} \begin{pmatrix} d \\ s \\ b \end{pmatrix}$$

After proper diagonalisation, $\mathcal{L}_5$ simplifi es in (see for instance [22]):

$$\mathcal{L}_5 = -m_{d_i}\overline{d}_i d_i \left(1+\frac{h(x)}{v}\right) - m_{u_i}\overline{u}_i u_i \left(1+\frac{h(x)}{v}\right)$$

with m_{d_i}, m_{u_i} being the masses of d_i and u_i quarks.

1.2 Beyond the Standard Model

1.2.1 Why look for a theory beyond the Standard Model?

Although the Standard Model has been verifi ed with extreme precision ($\sim 0.1\%$) by the experiments, it has its limits [23]:

- the origin of the symmetry group $SU(3)_C \times SU(2)_L \times U(1)_Y$ is not explained.
- it does not include gravity. A unifi ed description of all interactions would be desirable.
- it contains many free parameters, especially Higgs and fermion masses
- m_H is instable under radiative corrections. This issue is known as the hierarchy problem of the Higgs sector

Let's have a look at the last point. The Feynman diagrams represented in fi gure 1.2 introduce a radiative correction to the μ parameter of the Higgs potential:

$$\mu^2 = \mu^2(\Lambda_{cut\ off}) + \Delta\mu$$
$$\Delta\mu \sim \frac{n_W g_2^2 + n_H \lambda^2 - n_f h_f^2}{16\pi^2}\Lambda_{cut\ off}$$

Figure 1.2: μ radiative corrections

For $\Lambda_{cut\,off} \gtrsim 1\,TeV$, v can be kept of the order the W boson mass in agreement with experiment only if a fine tuning of the parameters leads to a cancellation between $m(\Lambda_{cut\,off})^2$ and $\Lambda^2_{cut\,off}$. This fine tuning is *unnatural* and not satisfactory. Two possibilities are known to go beyond the $1\,TeV$ cut off:

- the Higgs field is a condensate of fermions. This is the approach of the Technicolour models
- each right diagram of figure 1.2 is cancelled by a left diagram of the same figure. This can be achieved if for each fermion there corresponds a boson with the same coupling to the Higgs. The cancellation will then be explained by a "natural" symmetry between fermions and bosons. This is the approach of the Supersymmetry models.

We will focus on the Supersymmetry approach in the following sections.

1.2.2 The Minimal Supersymmetric extension to the Standard Model

The Supersymmetric (SUSY) models unify fermion and boson descriptions by introducing a symmetry between these particles [24–26]. The SUSY generators, denoted as Q_α, $Q_{\dot\alpha}$, transform fermions in bosons and vice-versa:

$$F \xrightarrow{Q_\alpha} B \qquad B \xrightarrow{Q_{\dot\alpha}} F$$

The definition of the SUSY algebra structure contains, in addition to commutation relations, anticommutation relations like:

$$\begin{aligned} \left\{Q_\alpha, Q_\beta\right\} &= 0 \\ \left\{Q_\alpha, \bar{Q}_{\dot\beta}\right\} &= \sigma^\mu_{\alpha\dot\beta} P_\mu \end{aligned} \tag{1.9}$$

with,

$$P_\mu = \left(H, \vec{P}\right) \text{ and } \sigma_\mu = (I, \vec{\sigma})\,,\ \vec{\sigma} \text{ being the Pauli matrices}$$

As relation (1.9) shows, coordinate transformations intervene in the algebra structure. Gravity can be obtained by requiring a local SUSY invariance: the resulting model is called *Supergravity*.

normal particles		Supersymmetric partners		mass eigenstate
family	particle	family	weak interaction eigenstate	
quarks	$q = u,d,s$ c,b,t	squarks	$\tilde{q}_L, \tilde{q}_R$	$\tilde{q}_1, \tilde{q}_2$
leptons	$l = e, \mu, \tau$	sleptons	$\tilde{l}_L, \tilde{l}_R$	$\tilde{l}_1, \tilde{l}_2$
neutrinos	$\nu = \nu_e, \nu_\mu, \nu_\tau$	sneutrinos	$\tilde{\nu}$	$\tilde{\nu}$
gluon	g	gluino	$\tilde{g}$	$\tilde{g}$
W-boson	$W^{\pm}$	wino	$\tilde{W}^{\pm}$	charginos $\tilde{\chi}_1^{\pm}, \tilde{\chi}_2^{\pm}$
charged Higgs	H_1^-, H_2^+	higgsinos	$\tilde{H}_1^-, \tilde{H}_2^+$	
photon	γ	photino	$\tilde{\gamma}$	neutralinos $\tilde{\chi}_i^0, i = 1\ldots3$
Z-boson	Z^0	zino	$\tilde{Z}^0$	
neutral Higgs	H_1^0, H_2^0	higgsinos	$\tilde{H}_1^0, \tilde{H}_2^0$	

Table 1.2: MSSM particles

SUSY Lagrangian can be constructed with the help of two additional fields called *Superfields* and denoted θ, $\bar{\theta}$ [27–30]. The SUSY model extending the SM by adding a minimal set of new arbitrary parameters is called the Minimal Supersymmetric extension to the Standard Model or shortly MSSM. The particle spectrum of MSSM is given in table 1.2. A new quantum number is introduced, the R-parity:

$$R = (-1)^{2S+3B+L}$$

with S, B, L respectively the spin, the baryon number and the lepton number. For SM particles, R is equal to $+1$, for SUSY ones, it is equal to -1. If the R-parity is conserved then SUSY particles cannot decay into SM ones and the lightest SUSY particle, denoted as LSP, is stable.

The MSSM contains two Higgs doublets as we will now describe.

1.2.3 Higgs sector of the Minimal Supersymmetric Extension to the Standard Model

MSSM requires the two $Y = -1$ and $Y = +1$ Higgs doublets [31–33]. The $Y = -1$ doublet, we will denote $\phi_d = (\phi_d^0, \phi_d^-)$, generates the down-type quarks, whilst the $Y = +1$ doublet, $\phi_u = (\phi_u^+, \phi_u^0)$, generates the up-type quarks. About the potential minimum the Higgs fields can be written:

$$\phi_d = \frac{1}{\sqrt{2}} \begin{pmatrix} v_d \\ 0 \end{pmatrix} \qquad \phi = \frac{1}{\sqrt{2}} \begin{pmatrix} 0 \\ v_u \end{pmatrix}$$

with,

$$\mathrm{v}_d^2 + \mathrm{v}_u^2 = \mathrm{v}^2$$

Breaking the Higgs symmetry, similarly to what was done for SM in the section 1.1.4 gives five physical Higgs bosons:

a charged Higgs pair,

$$H^{\pm} = \phi_d^{\pm} \sin\beta + \phi_u^{\pm} \cos\beta$$

a pseudoscalar Higgs,

$$A = \sqrt{2}(\mathrm{Im}(\phi_d^0)\sin\beta + \mathrm{Im}(\phi_u^0)\cos\beta)$$

two scalar Higgs h, H eigenstates of the following mass matrix M_0 in the base $(\sqrt{2}\mathrm{Re}(\phi_d^0) - v_d, \sqrt{2}\mathrm{Re}(\phi_u^0) - v_u)$:

$$M_0^2 = \begin{pmatrix} m_A^2 \sin^2\beta + m_Z^2 \cos^2\beta & -(m_A^2 + m_Z^2)\sin\beta\cos\beta \\ -\left(m_A^2 + m_Z^2\right)\sin\beta\cos\beta & m_A^2\cos^2\beta + m_Z^2\sin^2\beta \end{pmatrix}$$

The eigenvalues of M_0^2 are the squared masses of h and H. h is defined as the lighter particle. By diagonalising M_0^2 we obtain:

$$\begin{aligned} m_h^2 &= \frac{1}{2}\left(m_A^2 + m_Z^2 - \sqrt{(m_A^2 + m_Z^2)^2 - 4m_Z^2 m_A^2 \cos^2(2\beta)}\right) \qquad (1.10) \\ m_H^2 &= \frac{1}{2}\left(m_A^2 + m_Z^2 + \sqrt{(m_A^2 + m_Z^2)^2 - 4m_Z^2 m_A^2 \cos^2(2\beta)}\right) \end{aligned}$$

We will denote α the angle of the rotation which diagonalises M_0^2 (eigenvectors $(\cos\alpha, \sin\alpha)$ and $(-\sin\alpha, \cos\alpha)$). Hence h and H can be written:

$$\begin{aligned} h &= -(\sqrt{2}\mathrm{Re}(\phi_d^0) - \mathrm{v}_d)\sin\alpha + (\sqrt{2}\mathrm{Re}(\phi_u^0) - \mathrm{v}_u)\cos\alpha \\ H &= (\sqrt{2}\mathrm{Re}(\phi_d^0) - \mathrm{v}_d)\cos\alpha + (\sqrt{2}\mathrm{Re}(\phi_u^0) - \mathrm{v}_u)\sin\alpha \end{aligned}$$

At tree level only two parameters are required to parametrise the Higgs sector. The usual choice is:

- the pseudoscalar Higgs mass m_A
- the ratio of the vacuum expectation values $\tan\beta = \frac{\mathrm{v}_u}{\mathrm{v}_d}$

The other Higgs masses can then be written:

$$\begin{aligned} m_{H^\pm}^2 &= m_A^2 + m_W^2 \\ m_{h,H}^2 &= \frac{1}{2}\left(m_A^2 + m_Z^2 \pm \sqrt{(m_A^2 + m_Z^2)^2 - 4m_Z^2 m_A^2 \left(\frac{1 - \tan^2\beta}{1 + \tan^2\beta}\right)^2}\right) \end{aligned}$$

The following constraint on m_h can be deduced from (1.10):

$$m_h \leq m_Z\,|\cos(2\beta)|$$

Nevertheless this constraint is only valid at tree level.

Higgs mass eigenstate	$t\bar{t}$ coupling	$b\bar{b}$ coupling
MSSM h	$\frac{gm_t}{2m_W}\frac{\cos\alpha}{\sin\beta}$	$-\frac{gm_b}{2m_W}\frac{\sin\alpha}{\cos\beta}$
MSSM H	$\frac{gm_t}{2mW}\frac{\sin\alpha}{\sin\beta}$	$\frac{gm_b}{2m_W}\frac{\cos\alpha}{\cos\beta}$
MSSM A	$\frac{gm_t}{2m_W}\cot\beta\gamma_5$	$\frac{gm_b}{2m_W}\tan\beta\gamma_5$
Standard Model Higgs	$\frac{gm_t}{2m_W}$	$\frac{gm_b}{2m_W}$

Table 1.3: Neutral Higgs couplings [32]. $\tan\beta$ is the vacuum expectation value ratio and α denotes the mixing angle between weak and mass eigenstates. γ_5 indicates a pseudoscalar coupling.

Coupling to weak bosons

At tree level, A and $H^{\pm}$ do not couple to VV, with $\mathrm{V} = W, Z$. Nevertheless, h and H couple to VV with the strengths:

$$g_{h\mathrm{VV}} = g_{\mathrm{V}} m_{\mathrm{V}} \sin(\beta-\alpha), \quad g_{H\mathrm{VV}} = g_{\mathrm{V}} m_{\mathrm{V}} \cos(\beta-\alpha) \tag{1.11}$$

with,

$$g_{\mathrm{V}} = \begin{cases} g & \text{for } \mathrm{V} = W \\ \frac{g}{\cos\theta_W} & \text{for } \mathrm{V} = Z \end{cases}$$

Coupling of two neutral Higgs to a weak boson is given by $g_{h/H,A,Z}(p_{h/H} - p_A)$ with:

$$g_{hAZ} = \frac{g}{2}\frac{\cos(\beta-\alpha)}{\cos\alpha}, \quad g_{HAZ} = -\frac{g}{2}\frac{\sin(\beta-\alpha)}{\cos\theta_W} \tag{1.12}$$

Yukawa coupling

ϕ_u^0 couples exclusively to up-type quark and ϕ_d^0 to down-type quarks. The Yukawa Lagrangian can be written:

$$\mathcal{L}_Y = -G_t[\bar{t}P_L t\phi_u^0 - \bar{t}P_L b\phi_u^+] - G_b[bP_L b\phi_d^0 - \bar{b}P_L t\phi_b^-] + h.c.$$

The couplings being proportional the quark masses, the Higgs bosons couple mainly with the heaviest quarks: with t for the up-type quarks and with b for the down-type quark. The couplings to fermion pairs is given in table 1.3.

Coupling to a τ lepton pair has the same expression as coupling to a bottom pair with m_b replaced by m_τ.

Charged Higgs coupling to fermion pairs is given by:

$$\begin{aligned} g_{H^- t\bar{b}} &= \frac{g}{\sqrt{2}m_W}(m_t \cot\beta P_R + m_b \tan\beta P_L) \\ g_{H^-\tau^+\nu} &= \frac{g}{\sqrt{2}m_W}(m_\tau \tan\beta P_L) \end{aligned}$$

Decoupling limit

For $m_A \gg m_Z$, we get:

$$\begin{aligned} m_h^2 &\simeq m_Z^2 \cos^2 2\beta \\ m_H^2 &\simeq m_A^2 + m_Z^2 \sin^2 2\beta \\ \cos^2(\beta-\alpha) &\simeq \frac{m_Z^4 \sin^2 4\beta}{4m_A^2} = O\left(\left(\frac{m_Z}{m_A}\right)^4\right) \end{aligned}$$

This limit is called the decoupling limit [34]. Indeed it can be shown that in this limit below the scale of m_A the effective Higgs sector is reduced to h, which then behaves like a SM Higgs.

In the decoupling limit, H is weakly coupled to VV and h is weakly coupled to AZ: see (1.11) and (1.12).

New physics is waiting for us beyond $\sim 1TeV$. This energy region, which has never been explored, will be observed at the LHC collider, which is under construction.

Chapter 2

LHC and CMS

2.1 The LHC project

The Higgs mechanism does not predict the mass of the boson it introduces. If the Standard Model describes the physics up to the GUT scale, then the Higgs boson mass must be less than $189\,GeV$[1] [35]. The combination of precise electroweak measurements excludes a Higgs boson with a mass more than $211\,GeV$ at a 95% confidence level [36]. LEP data have excluded a Higgs boson with a mass less than $114.4\,GeV$[1] [37]. To probe the complete allowed mass region a more powerful machine is needed. In 1994, the LHC project was approved. It consists of a proton-proton collider accelerating the colliding protons to the energy of $14\,TeV$ in their centre of mass. This collider will allow us to probe the Higgs boson masses from the limit given by LEP II up to the theoretical limit of $\sim 1\,TeV$. LHC will not only allow us to discover or exclude the SM Higgs boson, but it will also permit us to test theories beyond the Standard Model like SUSY models.

In addition to proton collisions the LHC will run few months a year with ion beams (e.g. lead beams). Collision of nuclei will allow us to produce quark-gluon plasma, the matter which composed our universe when it was younger than $10^{-10}s$.

Four experiments will be set up on the LHC machine:

- ATLAS and CMS are omni-purpose detectors designed for a large variety of physics investigations. Especially, they will look for Higgs bosons and physics beyond the standard model
- ALICE which will study heavy ion collisions
- LHCb dedicated to B-physics.

The LHC collider will be set up in the tunnel of the LEP, the former CERN big collider, a tunnel of $27\,km$ circumference situated about $100\,m$ underground between the Geneva Airport and the French Jura. The four experiments will be set up in four caverns distributed on the tunnel ring as illustrated in figure 2.1. Just to give a scale, ATLAS experiment's main cavern is $55500\,m^3$ big.

All particle beams first pass through the linear accelerator LINAC 2. Out of LINAC 2, protons are accelerated further in the most faithful machine of CERN, the $26\,GeV$ proton synchrotron PS (see figure 2.2), which has been serving science since 1959. The

[1] At 95% confidence level

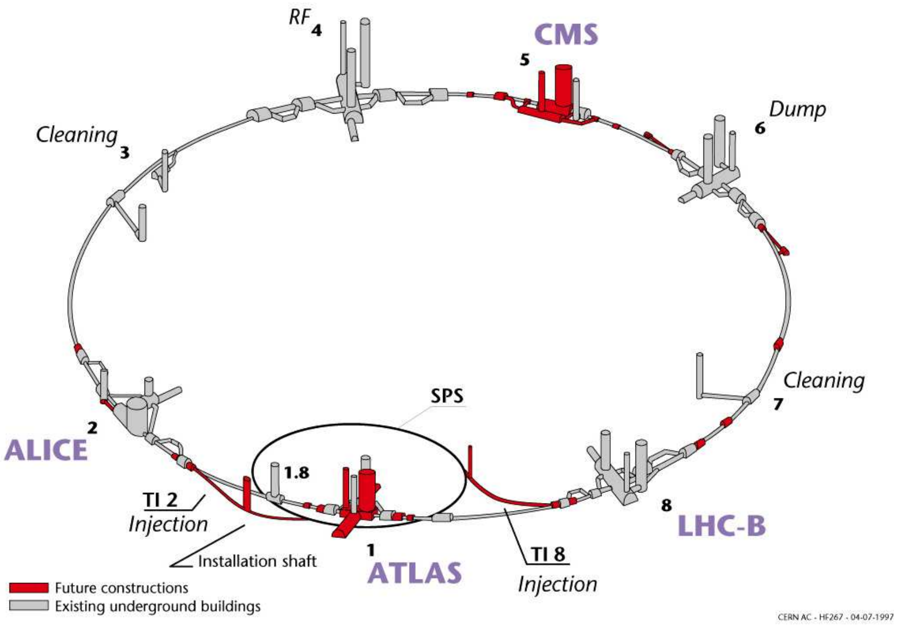

Figure 2.1: LHC tunnel and the four experiment. The tunnel of the former collider LEP is reused. New caverns have been dug for CMS and ATLAS because of the size of these detectors much bigger than the LEP ones.

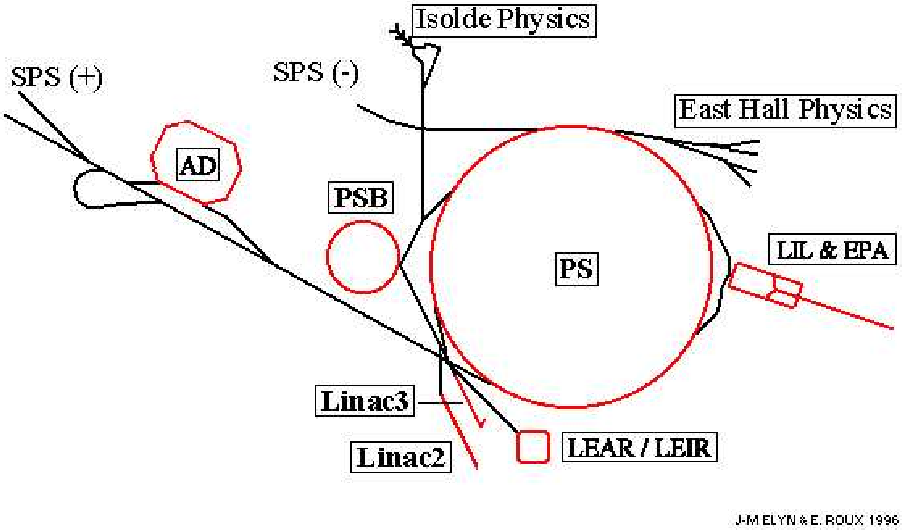

Figure 2.2: The Proton Synchrotron complex.

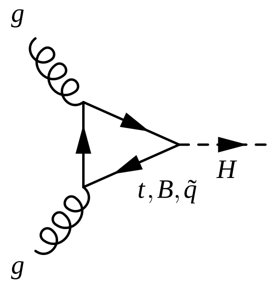

Figure 2.3: Feynman diagrams contributing at leading order to production of the SM Higgs boson by gluon fusion

super proton synchrotron SPS, first operated in 1976, will bring the proton momentum from $26\,GeV$ out of the PS to $450\,GeV$ before the beam is injected in LHC which will bring the protons to their final energy of $\sim 7\,TeV$. The ion itinerary is identical except that the beam is formed in the LINAC 3.

Once their nominal energy is reached, bunches of protons will collide at the experimental points and then Higgs bosons will be certainly produced. All the difficulty will be to detect them as the probability to produce them and having a detectable decay mode is $\sim 10^{-14}$.

2.2 Observing the Higgs boson at LHC

SM Higgs boson

At the LHC pp collider, the standard model Higgs boson is mainly produced in the gluon fusion channel, $pp \to gg \to H$. The Feynman diagrams contributing at leading order to this process are shown in figure 2.3 [38].

Branching ratios of the SM Higgs boson decays are shown in function of the Higgs boson mass in figure 2.4. Up to $\sim 130\,GeV$ the Higgs boson decay is dominated by the decay in a bottom quark pair. Because of the background level, this mode can only be exploited when the Higgs boson is produced associated with a $t\bar{t}$ pair [39] or a W boson: see figure 2.5. From $\sim 140\,GeV$ WW and ZZ are the dominant decay modes. Above the $2 \cdot m_W$ threshold from where the W boson can be produced on the mass shell, the ZZ mode is disfavoured in favour of WW mode. However it recovers rapidly (while going to higher Higgs boson mass) since it is then itself produced on the mass shell. From the $2 \cdot m_t$ threshold $t\bar{t}$ decay comes rapidly in the game. However it never exceeds $\sim 20\%$ of the total decay rate. This limitation can be explained by the dependence of the WW and ZZ decay widths on m_H^3, while $t\bar{t}$ decay depends only on m_H [40].

Although its branching ratio is modest, thanks to its signature which is cleaner than the di-b-jet one, the $\gamma\gamma$ channel is a good candidate for the discovery of a Higgs boson with a moderate mass. However this channel needs a lot of integrated luminosity. The significance is better than $5 \cdot \sigma$ for $120 < m_H < 140\,GeV$ with $\gtrsim 30\,fb^{-1}$ integrated luminosity [41]. This channel requires a narrow $\gamma\gamma$ mass peak to be distinguished from

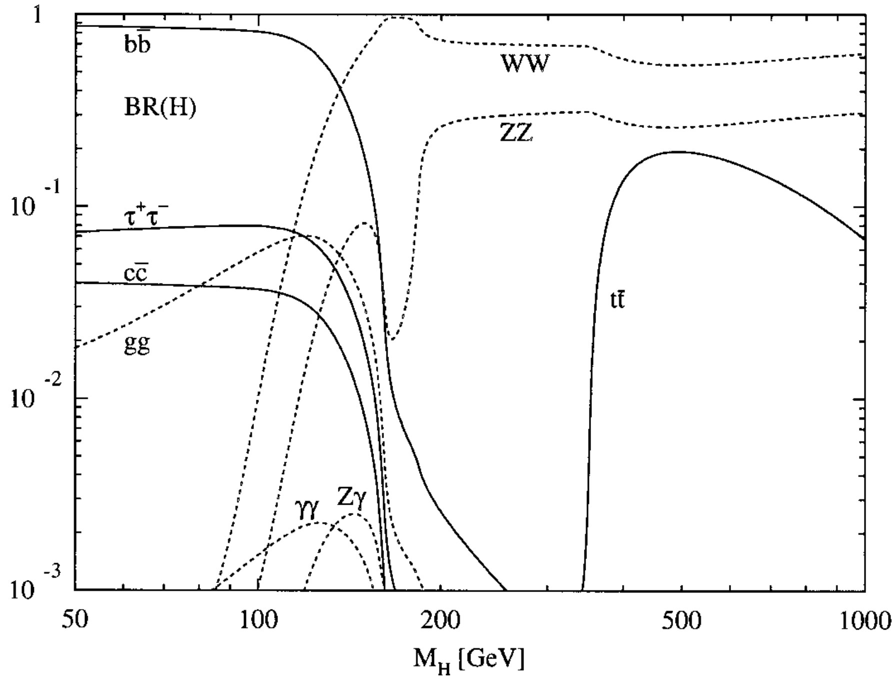

Figure 2.4: Branching ratios of SM Higgs boson decays [40].

the backgrounds which are ~ 10 times larger: a special effort has been put on the resolution of the CMS electromagnetic calorimeter.

For a SM Higgs boson with a mass between $\sim 130 GeV$ and $\sim 500 GeV$ the four lepton channel, $H \rightarrow ZZ, ZZ^* \rightarrow 4l^{\pm}$ provides an excellent signature. For a Higgs boson mass above $\sim 500 GeV$ the weak boson fusion channel $qq \rightarrow qqH$ is quite promising.

MSSM Higgs bosons

In the decoupling limit and at tree level, the light MSSM Higgs boson have the same properties as the SM Higgs boson and thereby the observation channels are $b\bar{b}$ and $\gamma\gamma$ decay modes described for the SM. For the heavy Higgs bosons, high $\tan\beta$ values ($\gtrsim 10$ for neutral ones, $\gtrsim 20$ for charged ones) are more favourable because of enhancement with $\tan\beta$ of couplings with fermions. The most promising channels to discover the charged Higgs bosons are $gb \rightarrow tH^{\pm}$ with $H^{\pm} \rightarrow \tau\nu$. For high $\tan\beta$ ($\gtrsim 10$), the neutral heavy Higgs bosons are mainly produced by bottom quark fusion. The Higgs boson is then associated to two bottom quarks and decays principally in a $b\bar{b}$ pair ($\sim 90\%$), a τ pair, a μ pair or a neutralino pair when the mass threshold of the latter is reached. For sufficiently large $\tan\beta$ a heavy neutral MSSM Higgs boson can be discovered in $\tau\tau bb$ [43–45] and $\mu\mu bb$ [46] modes. The four b mode will be studied in this thesis. For lower $\tan\beta$ values, if sleptons and neutralinos are light enough sparticle decay mode may cover the range $200 \lesssim m_A \lesssim 450 GeV$ [47–49]. The $5 \cdot \sigma$ discovery contour for the heavy Higgs bosons is shown in figure 2.6.

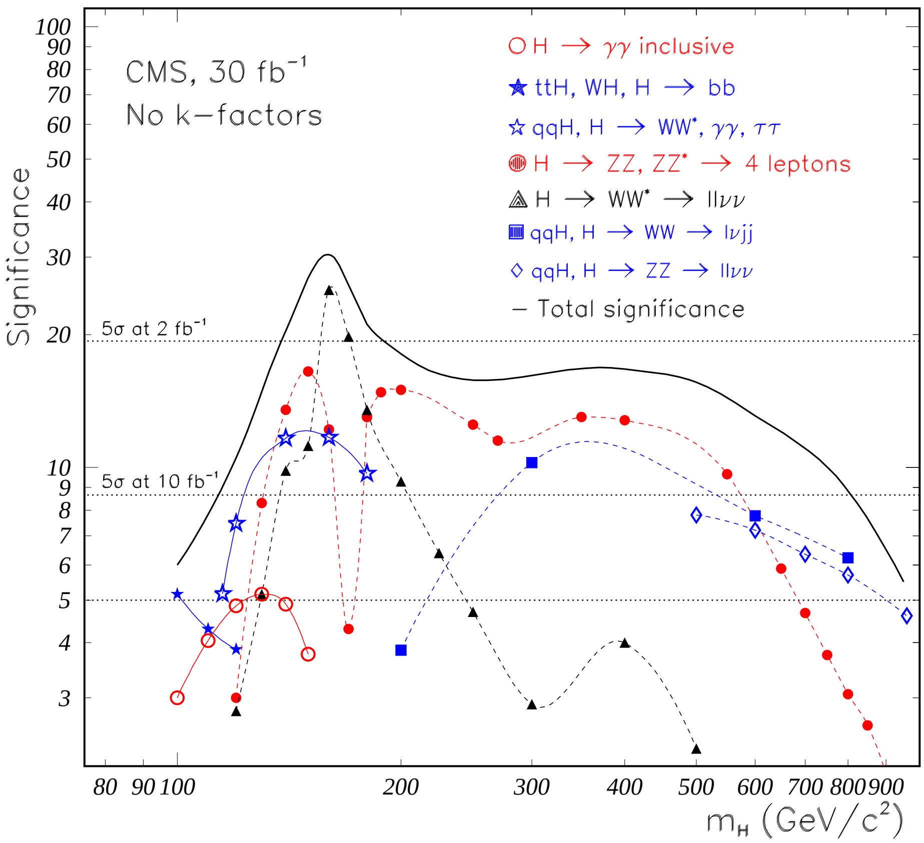

Figure 2.5: Expected statistical significance for the SM Higgs boson at CMS for 30 fb^{-1} integrated luminosity [42].

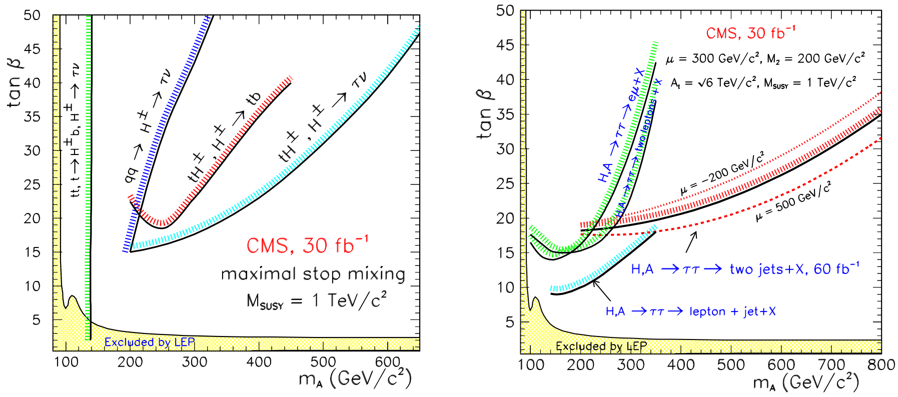

(a) charged higgs

(b) neutral heavy Higgs

Figure 2.6: Expected $5 \cdot \sigma$ discovery contour of the heavy MSSM Higgs bosons for a $30\,fb^{-1}$ integrated luminosity. $H/A \rightarrow \tau\tau \rightarrow 2\ jets + X$ corresponds to $60\,fb^{-1}$ integrated luminosity. [41, 42, 50].

2.3 CMS detector overview

The Compact Muon Solenoid is a $21.5\,m$ long detector with a $15.0\,m$ diameter. It weighs $12,500$ tons. It is made of 5 main components:

- a solenoid providing a high magnetic fi eld, gives us an accurate momentum measurement and an effi cient muon trigger
- a tracker including a pixel detector and a microstrip silicon detector
- an electromagnetic calorimeter with a very good resolution
- a sampling hadron calorimeter
- a highly effi cient muon detector system

Figure 2.7 shows the CMS detector with its different parts.

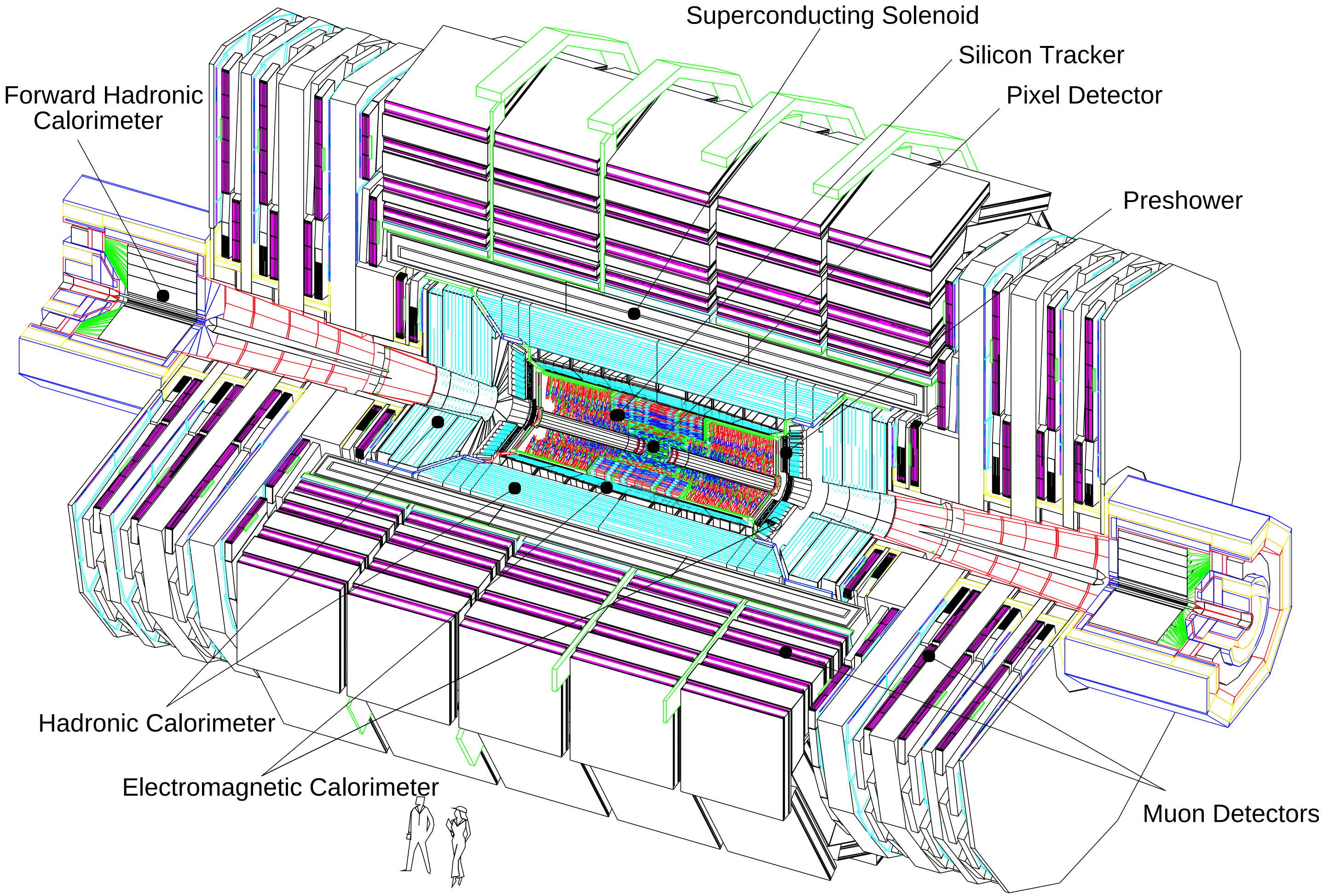

Figure 2.7: The CMS detector and its different parts.

Before describing the different parts of CMS, we will define the coordinate frame which is used at CMS.

Space coordinates

The following conventional frame will be used as the lab frame in this study:

(O,x,y,z)	direct orthonormal frame:
O	centre of the detector
z-axis	along the beam
x-axis	in the horizontal plane, pointing toward the $collider$ centre
y-axis	points up

In addition the following definitions will be used:

transverse plane (x,y)	plane orthogonal to the beam
φ	azimuth, i.e. angle with x-axis in the transverse plane
η	pseudo-rapidity[2] defined by $\frac{1}{2} \cdot \ln \frac{|\vec{p}|+p_z}{|\vec{p}|-p_z}$

2.4 CMS Magnet

The momenta of charged particles are measured from the curvature of their trajectory in a magnetic field. An intense magnetic field is necessary to measure momenta with high precision using a relatively compact detector. A $4\,T$ magnetic field is produced by a superconducting solenoid. The tracker, the electromagnetic calorimeter and the main part of the hadron calorimeter are inside the solenoid. The return yoke serves also as absorber for the muon detector. See figure 2.7.

2.5 CMS Tracker

Identification of bottom jets ("*b*-tagging") is based on the decay of bottom particles near (order of *mm* to *cm*) the primary vertex (see 4.4.3). Thereby it is crucial to reconstruct accurately tracks close to the interaction point. This requirement is fulfilled with a pixel silicon detector. The pixel detector is made of 2 barrels (3 at high luminosity) at radii of $4\,cm$ and $7\,cm$ at low luminosity ($4\,cm$, $7\,cm$ and $10\,cm$ at high luminosity) and 2 or 3 disks in each endcap covering radii from $6\,cm$ to $15\,cm$. Rapidity up to $\eta = 2.4 \pm 0.2$ are covered for tracks originating from the centre of the interaction region[3].

The pixels of the detector are made of $n+$ implants on a n-doped layer. A p-stop ring isolates each pixel from the neighbouring pixels. The bulk is of n-type. The pixel layout is shown in figure 2.8. In the sensor the $4\,T$ magnetic field drifts the holes and

[2] This variable is preferable to polar angle because a pseudo-rapidity difference $\Delta\eta$ is a Lorentz invariant under a boost in z-direction, this is important since in hadron colliders the collision centre of mass is boosted with an unknown speed.

[3] The ± 0.2 error corresponds to a displacement of the interaction point of 1σ.

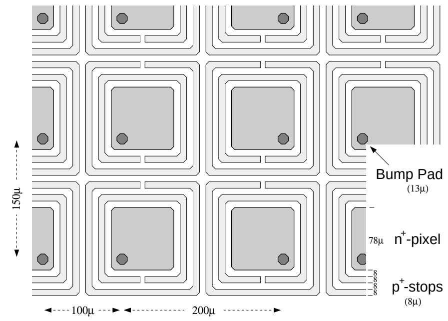

Figure 2.8: Layout pixel detector sensor [51].

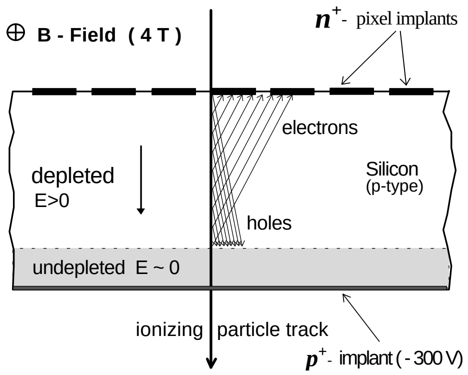

Figure 2.9: Charge sharing induced by Lorentz angle in the pixel detector [51].

the electrons stemming from the ionisation that the detected particle triggered with a $\sim 28^o$ Lorentz angle. Due to this Lorentz angle, the charge is shared by two pixels. This phenomenon is indicated in figure 2.9. Thanks to this drift charge sharing a resolution of $10 \sim 15\,\mu m$ can be achieved, despite the $150\mu m$ pixel size.

The particle tracks are reconstructed with the pixel detector and a silicon strip detector. The strip detector is divided in four parts [52]:

- an inner barrel, made of 4 barrel layers and 3 disks at each end
- an outer barrel, made of 6 barrel layers
- two end-caps, made of 9 disks

The silicon strip detector covers the pseudorapidity region $|\eta| \leq 2.5$. The operating principle is similar to the one of the pixel detector. The sensors are made of p+ strips on a n-type bulk: see figure 2.10. The silicon strip detector is made of a combination of single-sided and double-sided detectors. Double-sided detectors are built with two back-to-back single-sided ones tilted with a small stereo angle. This angle allows us to obtain the position along the strip direction.

Single track momentum resolution is given for an isolated muon in figures 2.11 and 2.12 . The impact parameter resolution is plotted in figure 2.13.

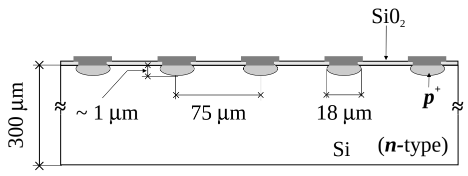

Figure 2.10: Sketch of a strip silicon sensor cross-section [51].

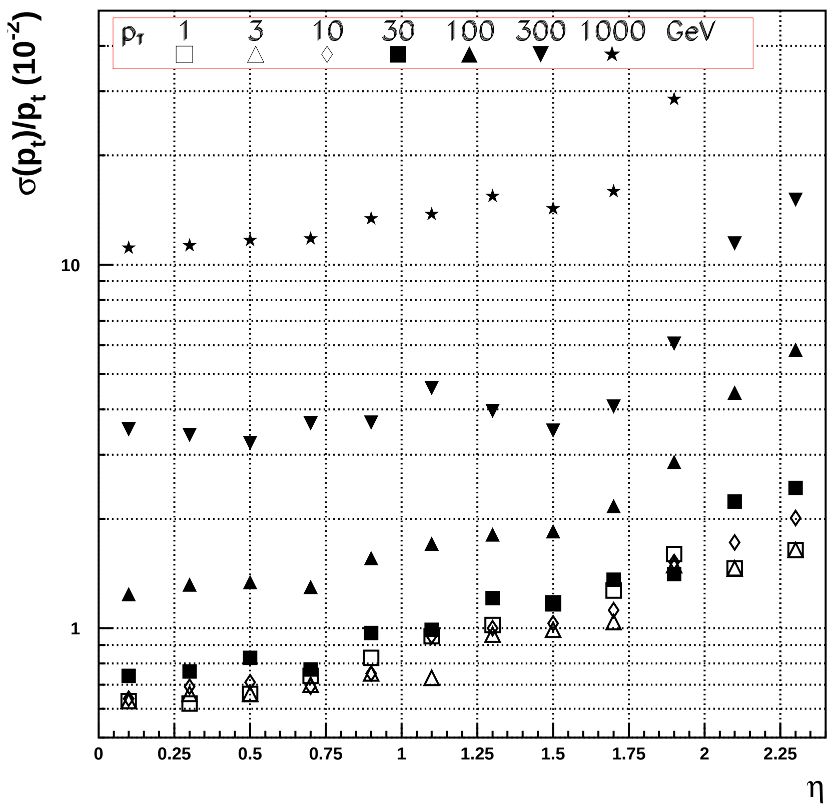

Figure 2.11: Transverse momentum resolution of the tracker in function of the pseudo-rapidity for isolated muons of different transverse momentum values [52].

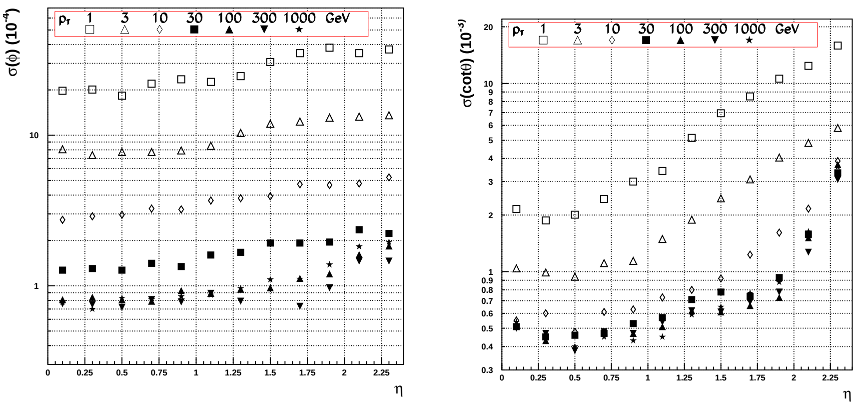

(a) Azimutal angle resolution.

(b) Resolution of the cotangent of the polar angle.

Figure 2.12: Angle resolution of the tracker in dependence on the pseudorapidity for isolated muons of different transverse momentum values [52].

While the tracker measures the trajectory and momentum of the particles with a minimum of disturbance, the calorimeter will measure their energy by absorption, that is by “destroying” completely the particle.

2.6 CMS electromagnetic calorimeter

The electromagnetic calorimeter (ECAL) [53] is made of 76832 lead tungstate crystals [54], $PbWO_4$. The energy deposited through ionisation by charged particules directly or from electromagnetic shower is converted to light via the fast luminescence of the $PbWO_4$ crystals. This produced light is collected and amplified by a photodetector. Because of low PbWO4 light yield photodetectotr with gain are needed. Avalanche photodiodes (APD) are used for the barrel and fine-mesh photomultipliers, which are less sensitive to radiation, for the endcaps.

The typical dimension of the crystals is $21.8 \times 21.8 \times 230\,mm^3$ for the barrel and $29.6 \times 29.6 \times 210\,mm^3$ for the endcaps. ECAL extends up to $|\eta| < 3$. The region up to $|\eta| = 1.48$ is covered by the barrel and the regions $|\eta| \in [1.48, 3]$ are covered by the two endcaps. The barrel offers a granularity $\Delta\eta \times \Delta\varphi = 0.0175 \times 0.0175$. In the endcaps the granularity increases progressively with $|\eta|$ from $\Delta\eta \times \Delta\eta = 0.021 \times 0.021$ to $\Delta\eta \times \Delta\varphi = 0.050 \times 0.050$. Resolution of the ECAL is shown in figure 2.14. The curve denoted as “noise” includes contribution of electronic noise and of pileup. The one denoted as “intrinsic” contains the shower containment and a constant term of 0.55%. The one labelled “photo” is the contribution of photostatistics.

For energy from $1\,GeV$ to $1\,TeV$, the resolution can be parametrised by [53]:

$$\left(\frac{\sigma}{E}\right)^2 = \left(\frac{a}{\sqrt{E}}\right)^2 + \left(\frac{\sigma_n}{E}\right)^2 + c^2$$

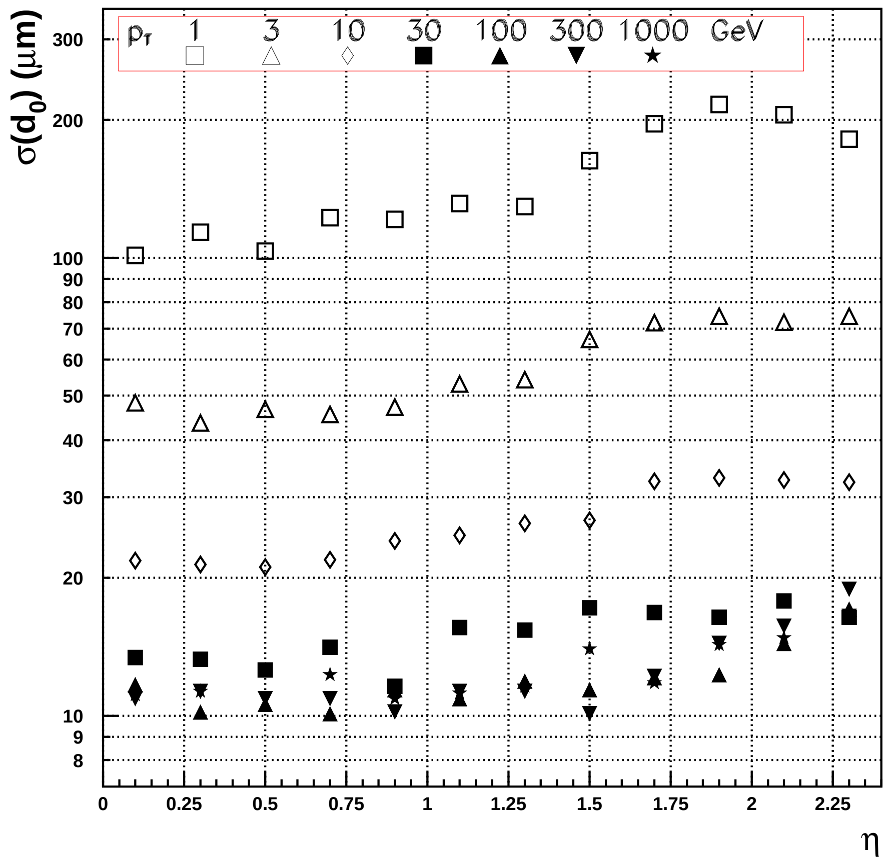

Figure 2.13: Impact parameter resolution of the tracker in function of the pseudo-rapidity for isolated muons of different transverse momentum values [52].

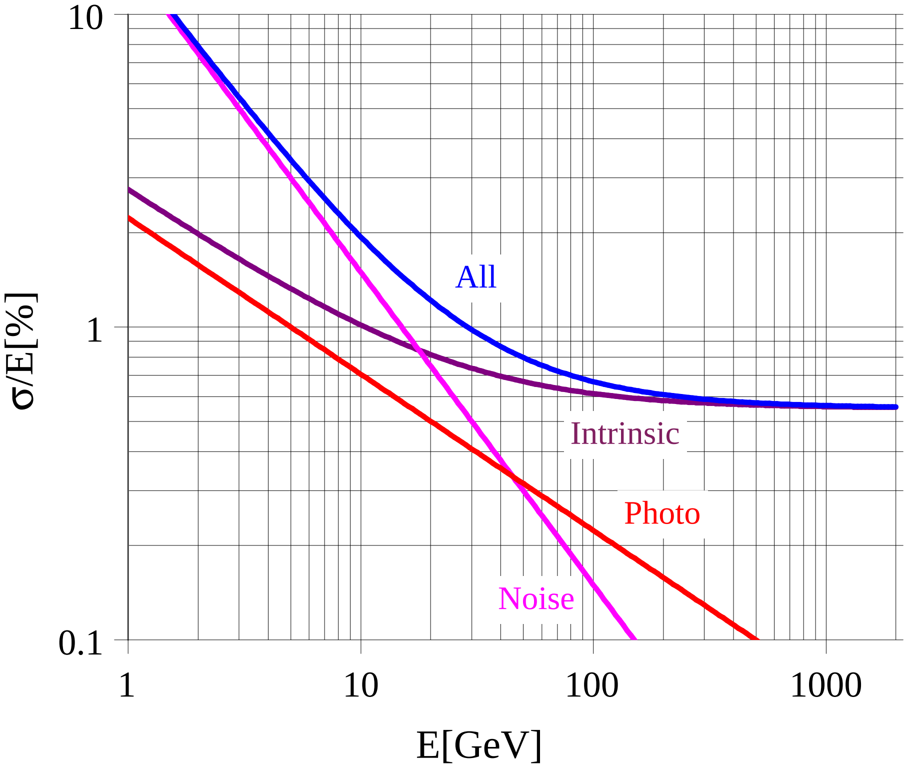

Figure 2.14: ECAL resolution at low luminosity [53].

Contribution	Barrel ($\eta = 0$)	Endcap ($\eta = 2$)
Stochastic (containment)	1.5%/√E	1.5%/√E
Photostatistics	2.3%/√E	2.3%/√E
Preshower sampling	–	5%/√E
Total stochastic term	**2.7%/√E**	**5.7%/√E**
Constant (containment etc.)	< 0.2%	< 0.2%
Longitudinal non-uniformity	0.3%	0.3%
Calibration	0.4%	0.4%
Total constant term	**0.55%**	**0.55%**
Electronics noise (at start-up)	150 MeV	750 MeV (E_T = 200 MeV)
Leakage current noise (low luminosity)	30 MeV	–
Pileup noise (low luminosity)	30 MeV	175 MeV (E_T = 45 MeV)
Total noise (low luminosity)	**155 MeV**	**770 MeV (E_T = 205 MeV)**
Electronics noise (at start-up)	150 MeV	750 MeV (E_T = 200 MeV)
Leakage current noise (high luminosity)	110 MeV	–
Pileup noise (high luminosity)	95 MeV	525 MeV (E_T = 140 MeV)
Total noise (high luminosity)	**210 MeV**	**915 MeV (E_T = 245 MeV)**

Table 2.1: Contributions to the ECAL energy resolution in barrel and endcap (5×5 crystal array), at low and high luminosity [53].

Where a is the stochastic term, σ_n the noise term and c the constant term. The constant term includes the heterogeneity of the longitudinal light collection, the crystal-to-crystal intercalibration errors, the leakage of energy from the back of the crystal and geometrical effects. Table 2.1 gives the value of these parameters with the different contributions.

To provide π^0–γ separation a preshower detector (SE) with a thickness less than $2\,cm$ is placed in front of the crystals. The preshower contains lead converters and strip detectors. A schematic view of a preshower is shown in figure 2.15. The typical resolution is $300\,\mu m$ at $50\,GeV$. The endcap preshower covers the region $|\eta| \in [1.65, 2.61]$.

2.7 CMS hadron calorimeter

The hadron calorimeter is a sampling calorimeter: it is made of interleaved scintillator plates and brass or steel absorber plates. It comprises three parts:

- the barrel HB, which covers pseudo-rapidity region $|\eta| < 1.392$.
- the two endcaps HE, which cover the pseudo-rapidity region $|\eta| \in [1.305, 3.0]$.
- the two (very) forward hadron calorimeters, which covers pseudo-rapidity region $|\eta| \in [2.85, 5.19]$. They are denoted as HF.

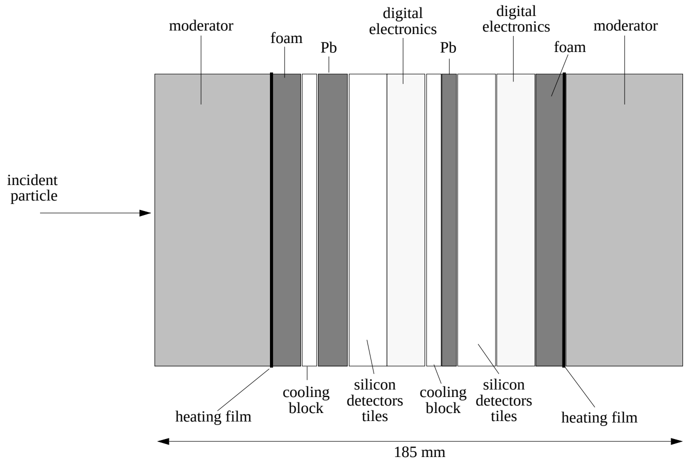

Figure 2.15: Schematic section of the endcap preshower [53].

Scintillators are also placed in the first layers on the muon detector (for $|\eta| < 1.305$): they form the HO (HCAL Outer) system. They are needed because the depth of inner part, 5.12 interaction lengths, is not big enough to detect the tail of the shower.

The barrel part has 17 sampling layers in HB and one layer (two for $|\eta| < 0.348$) in HO. Each endcap has 19 sampling layers in HE. The scintillators of HE, HB, HO are organic scintillators whose light is collected by wavelength shifting fibres (WLS): the primary *UV* photon is converted to lower energy blue photons by the scintillator, then the WLS fibre convert the blue light to green light. The green light is measured by hybrid photodiode (HPD): photons are converted to photoelectrons by a photocathode, the photoelectrons are accelerated by an electric field, accelerated photoelectrons are detected by a pad silicon detector.

HF is different than the other calorimeters. Each HF calorimeter is made of a single brass cylindrical absorber block. Quartz fibres, running parallel to the beam, are embedded inside the absorber. Shower charged particles are detected by the Čerenkov effect[4], which occurs in the quartz fibres. The active part of HF is $2.8\,m$ diameter and $1.65\,m$ length (about 10 nuclear interaction lengths).

The granularity of HB is $\Delta\eta \times \Delta\varphi = 0.087 \times 0.0873$, starting from $\eta = 1.74$ in HE the φ-bin increases by a factor of 2 and η-bin starts to increase. The design resolution of HCAL is:

$$E = 100\%/\sqrt{E} \oplus 5\%$$

The simulated (with GEANT) resolution is shown in figure 2.16. The $1 \sim 2\%$ degradation about $|\eta| = 1.3 \sim 1.4$ corresponds to the crack between HB and HE needed for the cable routing: degradation is due to the small loss of hermeticity and to the energy loss in the cables.

[4]A charged particle travelling in a medium faster than light (in the same medium) emits light, called Čerenkov radiation.

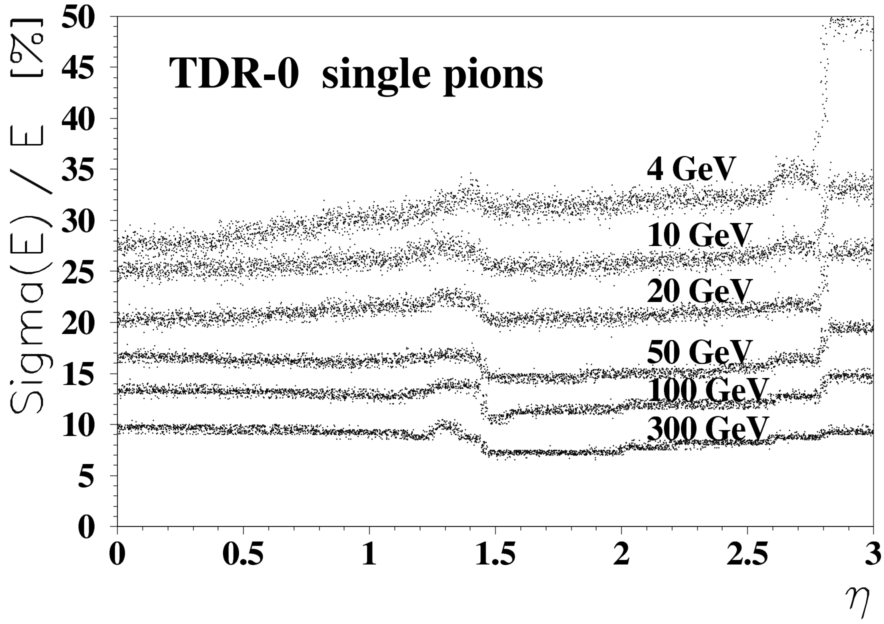

Figure 2.16: HCAL jet energy resolution for a single pion in function of the pseudo-rapidity. [55].

2.8 CMS muon detectors

Muon identifi cation is based on the low interaction of the muons with matter. Muon detectors are placed after the calorimeters which absorb every particle except muons and neutrinos, the latter being not directly detectable. Three technologies are used to detect muons:

- Drift chambers (DT) in the barrel cover region $|\eta| < 1.3$
- Cathode strip chambers (CSC) in the endcaps cover region$|\eta| \in [0.9, 2.4]$
- Resistive plate chambers (RPC) in the barrel and the endcaps cover region $|\eta| < 2.1$ and provide a fast response. At startup they will cover only region $|\eta| < 1.6$

In the endcaps, fours layers of CSC disks, called stations, are interleaved with the three layers of magnet return yoke. A CSC station is made of six layers of CSC chambers. In total the endcaps count 540 chambers. As shown in fi gure 2.17, a CSC is made of two parallel cathodes separated by $9.5\,mm$. In the middle of these two plates, parallel wires are placed every $3.12\,mm$. One cathode face is made of strips orthogonal to the wires and parallel to CMS radius. Henceforth radial position is measured by the wires and φ position by the strips. The chambers are fi lled with a mixture of argon and carbon dioxide. The functional principle of this multiwire proportional chamber [56–58] is the one of proportional counter: a high voltage bias is applied between the cathode and the wires (anodes), a charged muon, passing through the gas ionises it. Resulting electrons drift to the wire. Near the wire, where the electrical fi eld is maximal the electrons are accelerated enough to ionise again the gas, the resulting electrons ionise again the gas

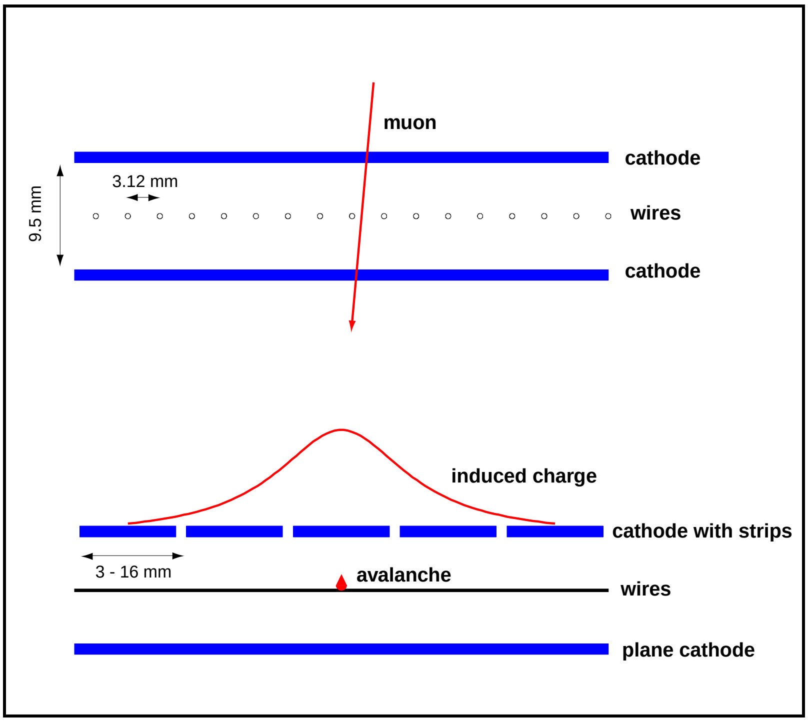

Figure 2.17: Principle of coordinate measurement with a cathode strip chamber: cross-section across wires (top) and across cathode strips (bottom). The small wire spacing allows a fast chamber response, while a track coordinate along the wires can be measured by interpolating strip charges [59].

and so on. The number of Electron-ion pairs increases exponentially, this phenomena is called avalanche. The avalanche is formed in about $1\,ns$. The signal is produced by the cations, which migrate slowly to the cathode.

The barrel drift tube chambers are made of anode wires, about $2.5\,m$ long, placed in the middle of I-profile cathodes as shown in figure 2.18. The cell between two I-profile cathodes forms a tube (with a somewhat rectangular section), these chambers get their "drift tube" name thereafter. The pitch of a cell is $11\,mm \times 41\,mm$. The particle position perpendicular to the wire is given by the position of the cathode collecting the signal and by the drift time of the electrons. The drift tubes are filled with a mixture of argon and carbon dioxide. A DT chamber is made of three Super Layers (SL): two SL to measure the r–φ coordinates and one for the z coordinate. An SL is itself made of four layers of rectangular drift cells staggered by half a cell. Four concentric cylinders made of DT chambers are interleaved with the three barrel magnet return yoke cylinders. In total the whole DT detector contains about $195,000$ sensitive wires. A $100\,\mu m$ spatial resolution is achieved with the entire DT detector.

In the RPC [60] the electric field is generated by two parallel electrode plates separated by a small gap of $2\,mm$. The signal is collected by strips parallel to the electrode. CMS RPC uses actually two pairs of electrodes in order to improve the signal level, this is called a double gap RPC: see figure 2.19. The RPC detector provides a response

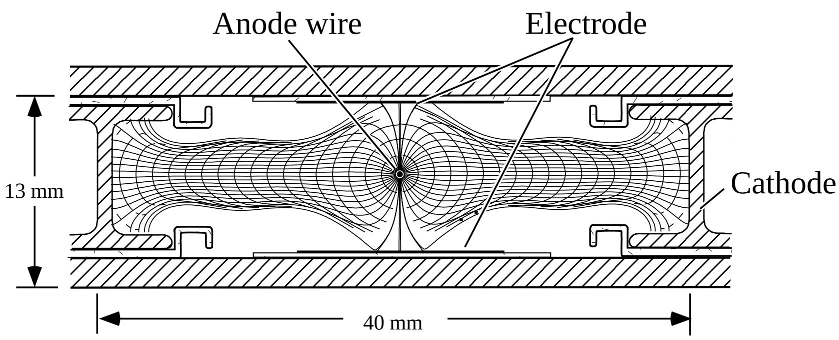

Figure 2.18: Transverse view of the baseline cell; also shown drift lines and isochrones, for a typical voltage configuration of the electrodes (TDR design). [59].

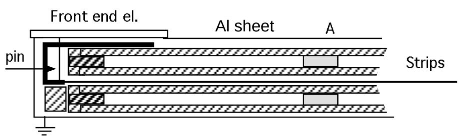

Figure 2.19: Double gap RPC (module type A) [59].

faster than the bunch crossing of 25 ns period. The time resolution of the RPCs is about 3 ns. Thus it allows us to identify without ambiguity the bunch crossing, which the muon originates from. This gives fundamental information for the LV1 trigger. The CSC and the DT chambers are also used for the LV1 trigger.

The muon reconstruction efficiency is expected to be better than 95%. For tracks up to 1 TeV the charge assignment error is less than 0.5% (using tracker information): see figure 2.20. The transverse momentum resolution for muons is defined here by:

$$\frac{\Delta p_t}{p_t} = \frac{1/p_t^{meas} - 1/p_t^{true}}{1/p_t^{true}}$$

Figures 2.21 shows the p_t resolution of the muon detector with and without combination with tracker information.

A flow of 1 $Tbit/s$ of data (after LV1) comes from these different subdetectors. These data must be combined, transported and selected before being stored. These three tasks are the charge of the data acquisition system.

2.9 CMS data acquisition system

Each CMS subdetector has its own data readout. The CMS subdetector readouts pass the data to the global data acquisition system (global DAQ or shortly DAQ). The DAQ [61] has 3 functionalities:

- getting the data from the subdetector readouts

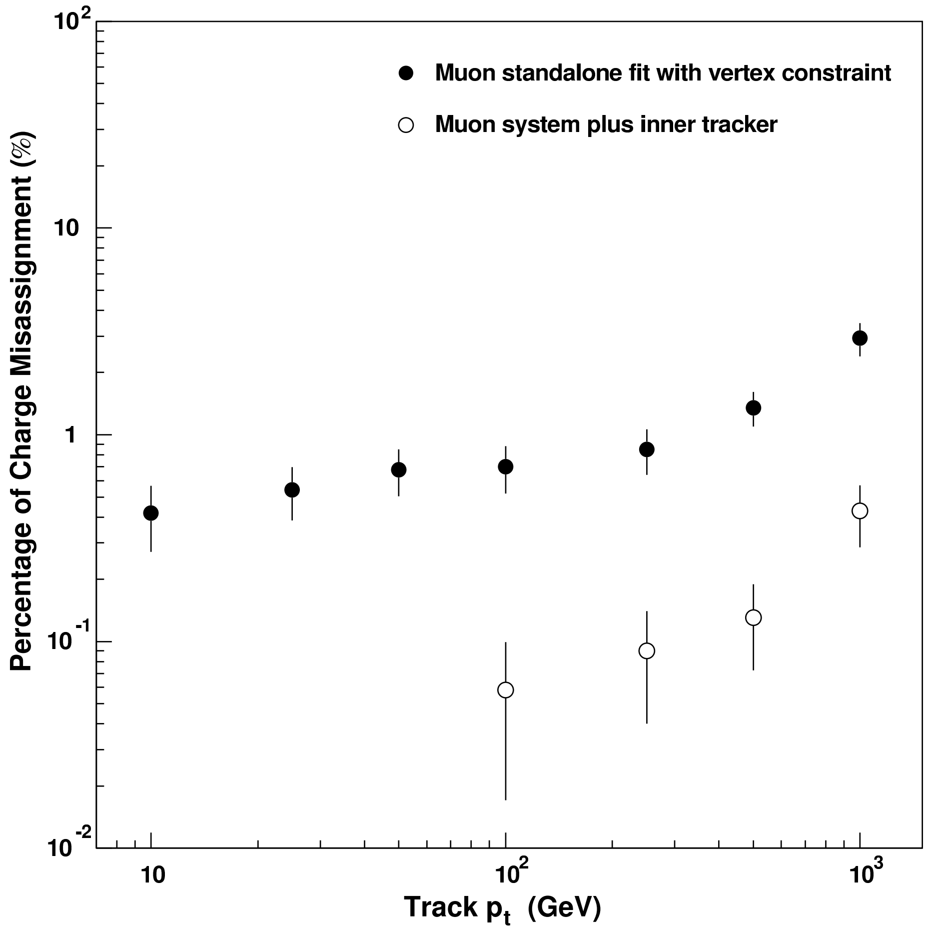

Figure 2.20: Percentage of incorrect charge assignments versus track p_t using both the vertex constrained muon stand-alone track fit and the combined muon system and inner tracker fit. For the combined fit, no misassigned charge is seen for tracks with p_t lower than 100 GeV. [59].

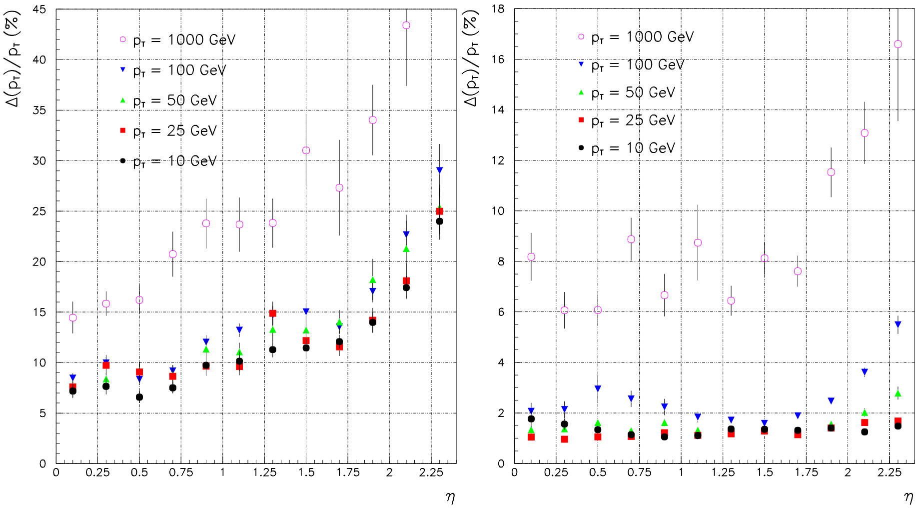

(a) Using only hits from the muon system with a primary vertex constraint

(b) Using the muon system combined with the central tracker

Figure 2.21: Momentum resolution for simulated muon tracks at selected values of transverse momentum. Full digitisation of the detector response was performed for the endcap chambers. [59].

- selecting the events: trigger process
- reorganising the data collected from the various subdetector readout modules into a consistent structure.

At high luminosity ($10^{34}\,cm^{-2}s^{-1}$), at every proton beam bunch crossing, that is every 25 ns, an event representing on average about $680\,kByte$ of data[5] is produced. For time and space reasons, every event cannot be stored or even processed. Therefore events must be selected at an early stage, while all the event data are not yet read. This selection is made in 2 steps by the trigger system:

- at first level, called LV1, the trigger is based on muon, electron, photon and jet identification and also on missing transverse energy. It selects 1 out of 400 events. LV1 uses the detectors with fast response: the three muon detectors, the electromagnetic and hadron calorimeters. Thanks to data buffering, LV1 has $1\,\mu s$ to take a decision. The speed constraints of LV1 are achieved by using custom electronics cards based on programmable chips (FPGAs, ASICs).
- at final level, the high level trigger (HLT) selects 1 out of 1000 events from the ones which have passed LV1. It reconstructs and applies selection criteria in steps. In that way the selection decision is taken as quickly as possible. Two main steps are distinguished: LV2 and LV3. Typcally LV2 uses information from

[5]The event size is rounded to $1\,MByte$ for contengency reason and the DAQ system is therefore designed for a nominal event size of $1\,MByte$.

only the calorimeters and the muon system. LV3 uses information from the every subdetectors including the Tracker. HLT is fulfilled by a computer cluster, the "Filter farm". The Filter farm is composed of on the order of 1000 processors. The processors in the filter farm get the events from the Event Builder. The Event Builder is in charge of collecting the data belonging to the same event from all the different subdetector readout modules.

The DAQ will decouple HLT and event reconstruction from the LV1 trigger. This decoupling is based on buffers and network switches. On LV1 trigger, fragments of different sizes enter in the 512 CMS DAQ inputs. The CMS DAQ will deliver in parallel "reassembled" events to its 512 outputs.

On an LV1 trigger request, the buffers of the CMS DAQ inputs are filled by fragments of an event coming from the detector front-ends: in figure 2.22, each box of the "Readout Systems" receives fragments of the same event. Asynchronously to the trigger, the CMS DAQ collects the event fragments of its input buffers into structures, each structure containing the data of one event. This sorting procedure is called "event building" and is based on the Builder Network. Then the "rebuilt" event goes to the Filter systems which will start to reconstruct the event and apply selection criteria of the HLT step by step in order to reject as early as possible the unwanted events. As soon as the event is known to be rejected, the filtering is aborted. The selected event will come out of the Filter systems fully reconstructed and will be passed to the computer services, which are responsible for monitoring and storage. Actually in addition to the selected events, a few rejected events will be also passed to the computer services for monitoring purpose.

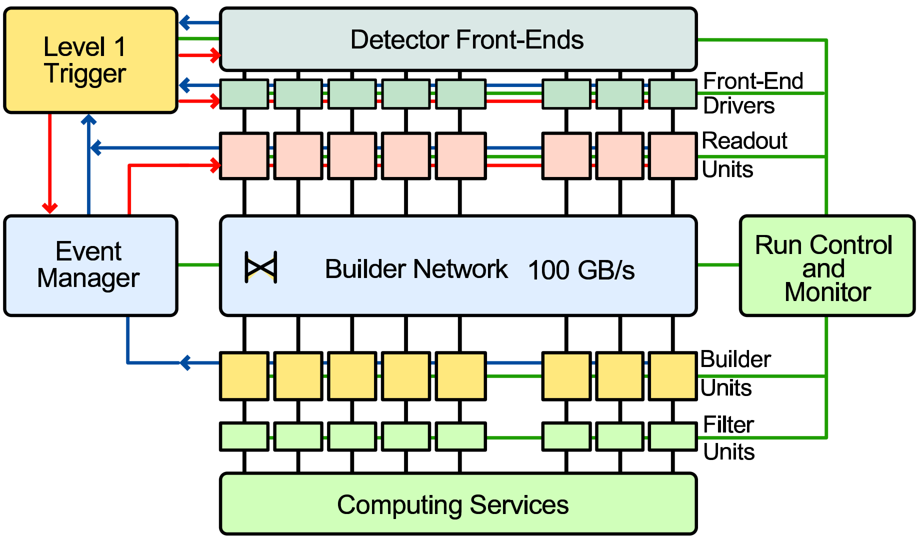

Figure 2.22: CMS DAQ architecture

The interface of the CMS DAQ with the subdetectors is made at the output of the Front-End Drivers (FED). The FEDs concentrate data from the subdetector readouts, the Front-End Systems (FES) in order to deliver event fragments to the CMS DAQ. Every 25 *ns* the LV1 trigger must decide if the event is retained, however 25 *ns* is not enough to take a such decision: several hundred of nanoseconds are needed. Therefore only a parallel trigger processing can achieve this stringent time constraint. This parallelisation is made using a pipeline architecture. When receiving a trigger signal, a FES must deliver the data of the event responsible for the trigger: the time elapsed when a trigger signal is received since the fragment of the triggered event entered in the FES is called *latency*. This latency depends on the time the signal takes to travel from the trigger systems (see fibre length) and on the position of the channel inside the detector (see particle time of flight) and is therefore different for each FES.

Figure 2.23 illustrates the mechanism of detector readout common to every subdetector. This common mechanism is called the *FE model*. The system is synchronised on the LHC clock (bunch crossing “ticks”). The signal[6] of each channel goes into a pipeline. The pipeline can be seen as a programmable delay line for sampled signal: the sampled signal takes a fixed time to pass through the pipeline. The signal sampling, like the trigger, is synchronised with LHC clock. For calorimeters and muon detectors part of the read data goes also to the trigger primitive generator (TPG) and will be used for the LV1 trigger decision. When a trigger arrives from the Timing, Trigger and Control (TTC) link, the pipeline output is read and constitutes the output of the FES. Fragments of several detector channels are multiplexed and dressed up with bunch number, event number, and some additional information before being passed to the DAQ. The length of the pipeline (in other words its delay) must be adjusted to the trigger latency. This pipeline length, which is also called *latency*, is configurable and must be tuned for each FES/channel.

The readout of a channel comprises in addition to the pipeline latency many other parameters like amplifier gains. These parameters must be set up online, for instance before starting a run. They are crucial since the quality, and even the presence, of the detector signals (the channel ADC counts) and therefore of the physics data depend on them. The parameter values must be available together with the physics data for the analysis of the latter. The huge number of detector channels makes the management of these electronics configurations challenging.

[6] digital or analog depending on the subdetector.

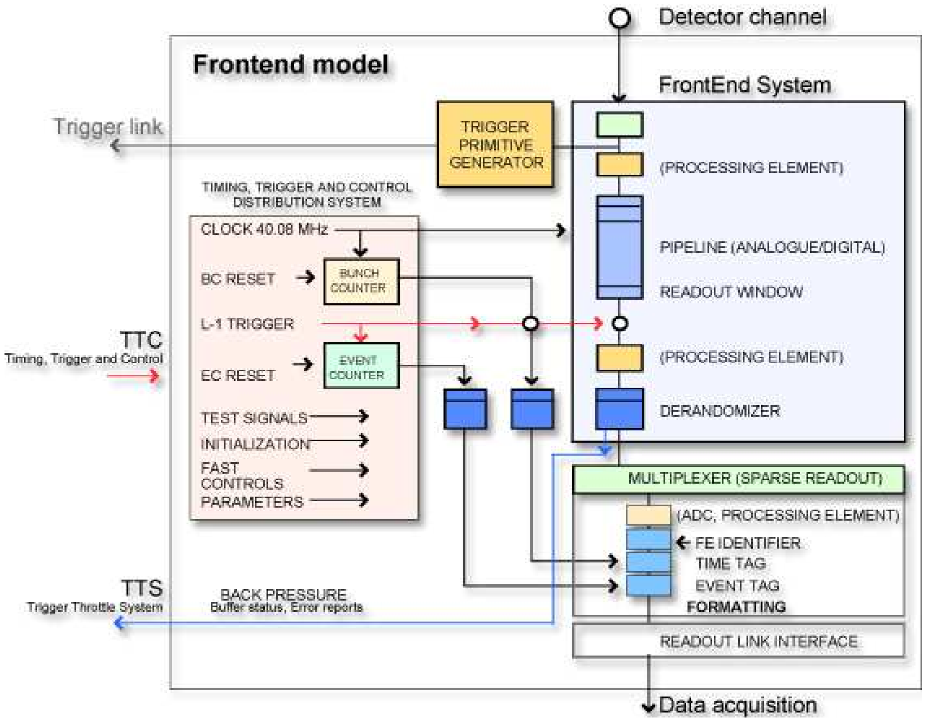

Figure 2.23: Front-End model

Chapter 3

CMS DCS and database

3.1 CMS detector control system overview

3.1.1 Introduction

The controls of an LHC experiment comprise two parts:

- RCMS, the Run Control and Monitoring System
- DCS, the Detector Control System

The RCMS takes care of controlling and monitoring the DAQ and all the task which are specifi c for a run. The DCS takes care of the control and monitoring tasks which must be performed anytime, even outside of a run.

3.1.2 JCOP project

At the beginning of 1998, the Joint Controls Project, shortly JCOP was set up [62–64]. This project team is a collaboration between the four LHC experiments and the CERN controls group from the CERN IT division, IT/CO. It aims to optimise the usage of the limited human resources available to build the LHC experiment DCSs by using common solutions. “The scope of JCOP is to provide a common framework of tools and components to allow the experiments to build their own Detector Control System (DCS) applications. The purpose of the DCS is the initialisation, monitoring and operation of the different sub-detectors. It has also to interact with the Data Acquisition system and external systems such as the CERN infrastructure services and the LHC accelerator” [65].

3.1.3 SCADA

The DCS has tasks similar to the systems used in industry to control assembly lines, chemical plants, nuclear plants, etc. These systems are generally built with commercial off-the-shell software. Such software, which are used to build control systems, is called SCADA, which stands for Supervisory, Controls And Data Acquisition.

Thereby, with the aim to minimise the required human resource, a SCADA system will be used to build the DCS of the LHC experiments. For this, the JCOP team has chosen PVSS II from the Austrian company ETM.

PVSS II has its own database where the controls parameters (temperature, voltage, etc.) are stored. Nevertheless for a very large amount of data, a specialised database manager is needed.

3.2 Introduction to relational databases

A database is "a usually large collection of data organised especially for rapid search and retrieval (as by a computer) " (Myriam-Webster dictionary). There exist two types of databases:

- object oriented database, where data are stored in objects in the sense of object-oriented programming
- relational database, where data are stored in tables

A relational database contains in addition to the data the relationships between them. Two main concepts are used to describe these relationships:

- tables
- and references

Data are organised in tables. The relationships between data are determined by the definition of:

- the set of tables
- the columns of those tables
- the relations between the tables

In a table a special column or set of columns are used to identify a table row. This set of columns is called the primary key and its content defines solely a row.

Relationships between tables are made through references. Rows of a table can refer to a row of another table. To achieve that, the former rows must contain the primary key of the latter. To illustrate this, we will use a simple example of a human resource database. We define:

- a table containing the list of employees: see table 3.1
- a table containing the list of company groups: see table 3.2

Each group has a leader. This relationship is represented in figure 3.1 by an arrow labelled "group leader". This arrow represents also the "reference constraint" which implements this relationship: "column 'group_leader_id' of table 'groups' references column 'user_id' of table 'employees"'.

Other references can be done:

- the referenced column can be any column defined as "unique" instead of the primary key column. A "unique" column is a column, which cannot contain twice the same value.

user_id	firstname	lastname	birthdate	office	phone_extension
65744	John	Smith	12/02/1965	398-5-01	7873
09903	Oliver	Grant	3/08/1970	345-2-03	9094
8778	Michael	Brant	3/05/1956	878-6-08	8778

Table 3.1: “employees” table

group_name	group_leader_id	responsibilities
HR	65744	managing human resources
SA	8778	sales and client relation

Table 3.2: “groups” table

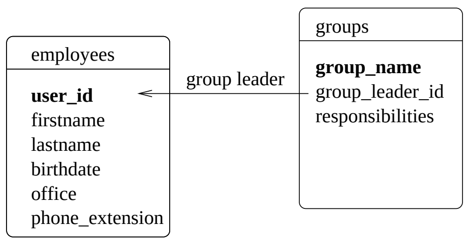

Figure 3.1: The “employees” and “groups” table relationship. The table “groups” refers to the table “employees” through its column “user_id”. The primary keys are represented in bold text.

- instead of a single column, a set of columns can be referenced. In this case each value of the referenced columns will be put in a separate column of the referencing table. One constraint is that the set of referenced columns must identify solely a row.

The database manager takes care of keeping the “uniqueness” constraints fulfilled by issuing error messages on a row insertion, which would violate the constraints. Similarly, it will ensure that the referenced rows actually exist. For instance it will refuse to delete a row which is still referenced by another row.

This reference relationship mechanism will be used to map the hierarchy of the electronics parameter in the FE electronics configuration database.

3.3 Database for electronics configuration

The FE (Front-End) electronics of the CMS subdetectors, especially the read-out electronics, needs to be configured. Because of the number of channels (about $54.5 \cdot 10^6$), the number of FE electronics parameter volume is huge (about $1.6 \cdot 10^6$ for the tracker readout electronics only). A database is obviously required to store these parameters. The electronics configuration influences the physics results and therefore it is needed:

- to keep track of the parameters used for a specific run
- to control the access to the FE electronics parameters stored in the database

Since these requirements are identical to all subdetectors, a general system was designed. The electronics parameters might be obtained from various sources including from some computer processes. Therefore the access to the database must remain open.

The user interface must be well integrated into the control system’s user interface. This means that the user must have the same look and feel as for the rest of the control system.

The FE configuration system, which was developed, is comprised of 3 actors as illustrated in Figure 3.2: the database, the controller and FE supervisor(s). The database stores the parameters, the controller controls the operation and provides the user interface and the FE supervisor(s) access(es) the FE. The controller, as well as the database, can be distributed over many PCs on different platforms. In order to transfer the data in parallel to the electronics, the system can have several FE supervisors.

3.3.1 Download process

On user request, or during an automatic procedure (e.g. start of run, error recovery, calibration process), the controller sends a download command to the FE supervisors (see figure 3.3). Then the FE supervisors fetch the data from the database and download them into the FE electronics. It is possible to ask each FE supervisor to read back the configuration from the electronics and send it back to the database. Then, if some values are outside the limits, an alarm summarising the differences will be sent to the controller.

3.3.2 Alarm handling

The alarm calculation is made inside the database and has been implemented in PL/SQL (procedure language/standard query language). An alarm indicates that one or several

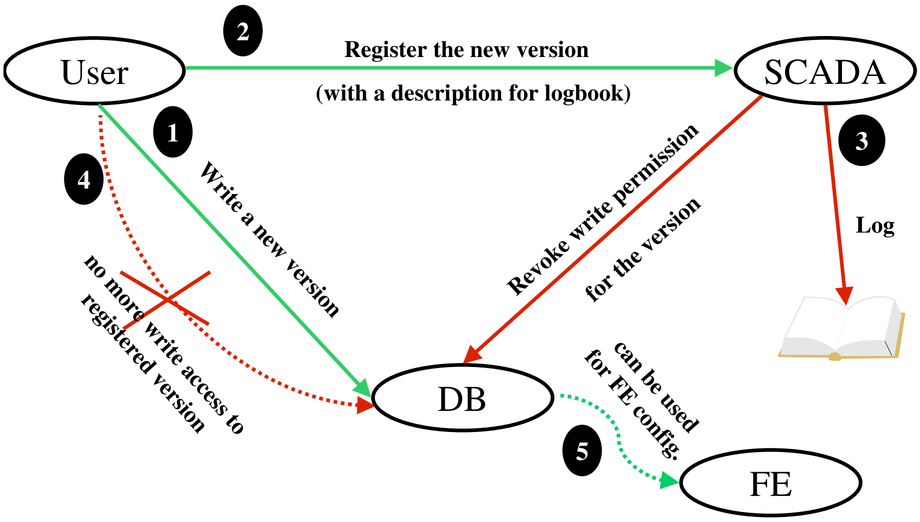

Figure 3.2: Version registration mechanism

values read back from the FE electronics are outside of the range set in the database. If an alarm is triggered for each wrong parameter value, then a general download will lead to an alarm avalanche. To avoid this, the alarm is triggered only when all the parameters have been read back. Once the FE supervisors have read back all the parameters, they set the state in the "download_state" table to "uploaded". This triggers (through an Oracle trigger mechanism) the verifi cation of every parameter stored back in the database versus its predefi ned range. From this check a summary alarm message is formed. If only a few parameters are out of range, they are all mentioned in the message, otherwise only some of them are mentioned as examples and the total number of out-of-range parameters is given.

3.3.3 Access control

In order to keep the history of the data used for a confi guration, versioning of the stored parameters and a registration mechanism have been developed. The FE electronics parameters, and also calibration constants, may be calculated by some process, which is independent of the SCADA. Before a confi guration set can be used for a run, it should be registered using the SCADA. Figure 3.2 describes this registration mechanism. The user, or process, can create a new version of the parameters in the database. As long as the version is not registered the parameter values can be modifi ed. At registration time, the SCADA logs the description of the new confi guration and revokes the write permission on the registered confi guration set. This write permission revocation is done using the database fi ne grain access control provided by the Oracle package "dbms_rls". It is only from that time that the parameter of the new version can be used to confi gure the FE electronics. In this way, all versions used for confi guration will be kept unchanged and can be consulted during data analysis.

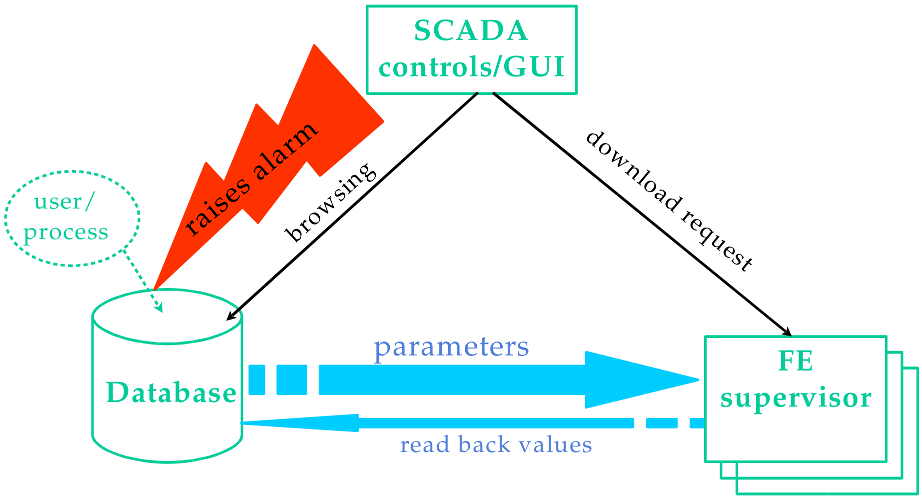

Figure 3.3: FE electronics confi guration mechanism.

3.3.4 Database model

Each electronic device type is represented by a table. This table contains the device parameters. In the example of the CMS Tracker described in section 3.2, the database table named APV contains all the parameters of the APV readout chips: see fi gure 3.4. A device can be part of a higher-level device (e.g. a chip is part of a board). Such membership relationships are specifi ed in the database by a standard relational database "reference constraint" between the device and the subsystem. A "controlled by" relationship or any N-to-1 relationship is represented by such a constraint.

The parameter versions are managed by a specifi c table, typically called "version", which contains the list of all available versions. A version is identifi ed by two numbers: the major and the minor version ids. The whole set of parameters of major versions $M.0$, where M is the major version number and 0 the minor version number, is stored in the database. On the other hand, for a minor version an incremental storage is done: only parameters of version $M.m$, $m > 0$ which differs from version $M.0$ are stored. Data access speed and storage space are optimised.

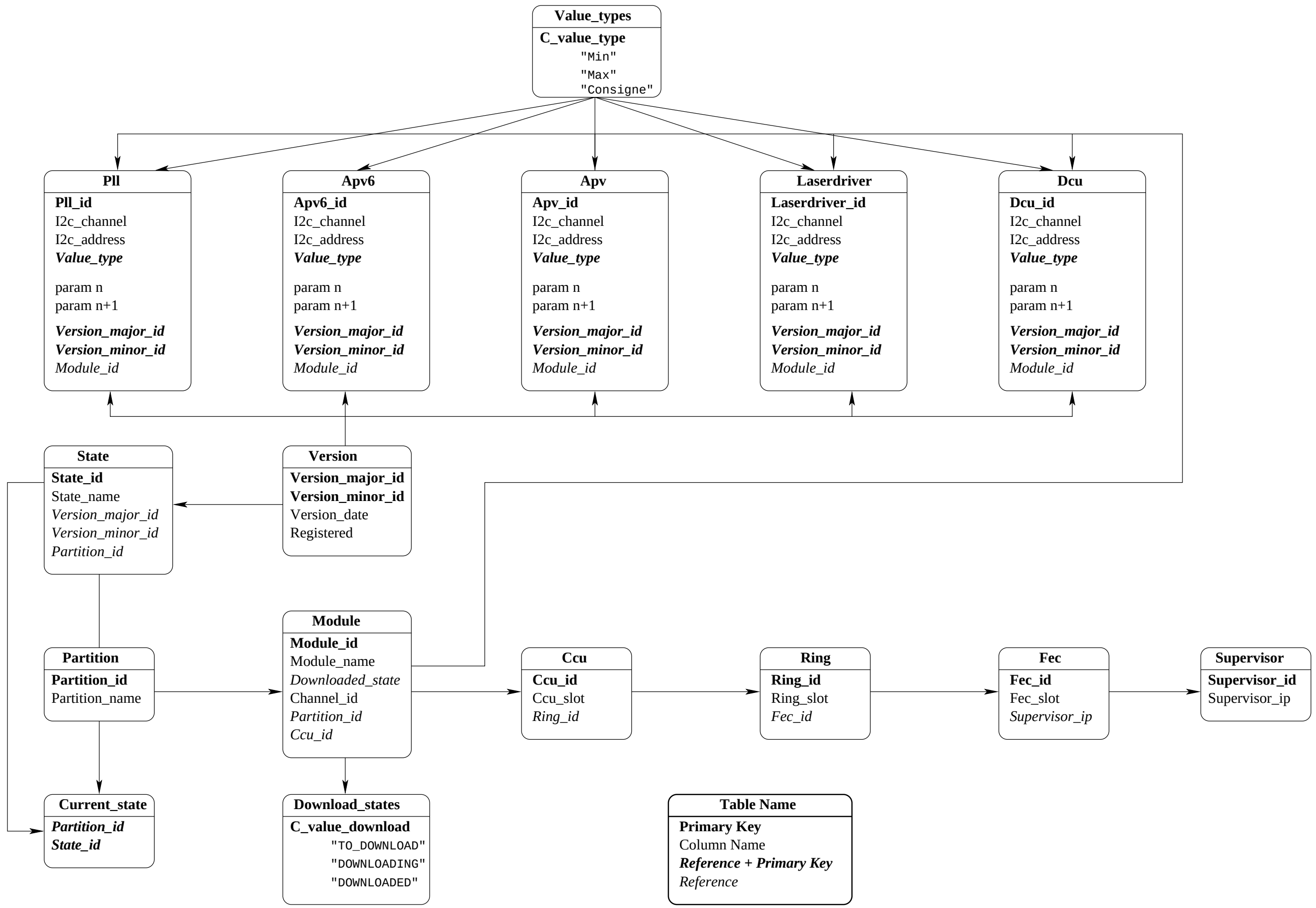

Figure 3.4: Tracker FE electronics database structure.

The version table is composed of a minimum of five columns: one for the major id, one for the minor id, one for the version creation date, one for the description and one which specifies if the version has been registered. Each row of device type tables contains the values of one device for a specific parameter version. The row includes the version ids, which refer ("reference constraint") to the version table. Actually if a device contains versioned parameters and version-independent parameters, the device type table can be split into two tables: one for the versioned parameters and one for the version independent parameters. Finally, in order to use the alarm mechanism, the device type table must have a "device_type" column which specifies if the row contains set values, the minimum allowed values, the maximum allowed values or the monitored values. The "value_type" column and the version table are optional and are not needed if alarming or versioning are not required.

3.3.5 Implementation

Code specific for the database has been implemented in PL/SQL as stored procedures. A stored procedure is a subroutine whose code is stored in the database. It is executed in the database. These subroutines can be organised, as it has been done in packages. Use of stored procedures facilitates maintenance by keeping code dependent on data structure together with the data. In addition it has some benefits on the performance.

It was originally decided that the FE electronics configuration was part of the DCS. In this context the so called controller had to be developed using the tools of the DCS, that is the PVSS II SCADA. In the future the responsibility for the FE electronics configuration may be transfered to the Run Control, in which case the controller will be implemented using the Run Control tools.

For the user interface, I have developed a set of PVSS II panels: for version creation, for version registration, for database browsing, etc. These panels can be used as complex widgets. The database-browsing panel, called DBNav, is a generic user interface for Oracle 8i databases. It is able to discover itself the structure of the database and display it in a tree. These panels are based on two underlying PVSS II script libraries which can be used directly to develop custom scripts or panels.

3.4 A Java interface for the PVSS II SCADA system

3.4.1 PVSS II C++ API

The SCADA PVSS II product provides an Application Programming Interface (API) for C++ programming. This API gives full access to the PVSS II functionalities. Nevertheless its usage is more difficult than the usual way to build PVSS II applications, which uses the PVSS II C-like script language. In particular the necessity to call in a loop a “dispatch” function makes the programming of PVSS II C++ application difficult. The Java API, which I will describe here, combines the flexibility of the C++ API with the ease of use of the scripting language.

3.4.2 PVSSJava, a Java API for PVSS II

The alarm system described in 3.3.2 needs to access PVSS II from the Java programming language. Furthermore, in the case of the Tracker, the FE supervisor had been implemented in Java. For this reasons a complete Java API for PVSS has been developed. This API is based on the PVSS C++ API and on the Java native interface, JNI. The so called *PVSSJava* interface [66] is based on a Java library bundled with a shared library. The shared library, written in the C++ language, is linked with the PVSS II API libraries in order to access PVSS II. It has been provided for Linux and Windows operating systems.

The PVSSJava interface offers two operating modes: a local mode and a server mode. In the local mode, the user program is directly linked to the PVSS II API libraries, which implies that the PVSS II API libraries must be installed on the machine hosting this program. In the server mode, a JavaManager server runs as a PVSS II API manager on a machine running PVSS II. Then clients, which are user applications, can remotely access PVSS II via this server using RMI (Remote Method Invocation)[1]. The client code is then no longer specific to an operating system and can be run on any system supporting Java. The client can even run in a web browser as an Applet: this gives a powerful way to build a web interface to a PVSS II system. The use of RMI is transparent to the programmer; changing the access mode of an application from "local" to "remote client" just requires to change one line of code, which actually specifies the access type and the server location.

3.4.3 Usage of the PVSSJava interface

Most of the functionality of PVSS II is provided with the PVSSJava interface. The missing ones are the multi-language support, which is of no use for LHC applications, and the possibility to modify archived values (equivalent to the "dpSetTimed()" script function). The PVSSJava interface allows us also to call Java code from PVSS and for instance open a Java window from a PVSS II graphical user interface. Conversely a PVSS II user interface window (called "PVSS panel") can be opened from a Java program, although this is not so recommended since this is based on undocumented features of PVSS.

The PVSSJava interface has been used for the CMS FE electronics configuration system, but also for other applications like the CERN Gamma Irradiation Facilities (GIF) [67] in order to provide a web interface for the control system and for the LHC Alarm SERvice project (LASER) [68] to connect PVSS II control systems to a Java based alarm system.

3.5 Front-End electronics configuration system usage

3.5.1 Electronics-specific part

Two parts are specific to the front-end. The first part is the database content: typically each device will have a table which will contain its parameters. A general database scheme is given as a template. The other specific part is the *FE supervisor*. The FE supervisor is the software that fetches the data from the database and downloads it to the front-end electronics. It receives commands from the SCADA system. This part needs to know how to access the specific front-electronics hardware. It can get the data from the database using a standard interface like JDBC, as it has been done for the Tracker (see next section) or with a more Oracle-specific interface like OCI or Pro*C or in XML format (provided as standard by Oracle 8i). There is actually one part of

[1] RMI is a method to access Java applications remotely.

the FE supervisor which is generic: the interface to PVSS. This generic part has been developed as a library for C/C++ and Java.

3.5.2 CMS tracker front-end electronics and its parameters

The Tracker readout is based on custom chips called APV (stands for "Analogue Pipeline – Voltage mode"). An APV embeds a preamplifier, a shaper, an analog memory, a deconvolution filter (APSP) and a multiplexer for 128 channels. The memory consists of an array of 128x160 capacitors. This memory will store the signal during the LV1 latency (up to 3.2 *us* as already mentioned). On the LV1 trigger, samples from the memory pass through the APSP filter. The 128 channel output is multiplexed to 1 output channel. The level of the 128 consecutive samples corresponds to the peak amplitude of either the amplifier output signal or APSP filter output depending on the operation mode: the former is called "peak mode", the latter is called "deconvolution mode" [69]. Outputs of the APVs are multiplexed 2 by 2: the 128 samples of each of the 2 APVs are interleaved in order to give a signal with 256 samples. This multiplexing is done by a chip called the APVMUX. Parameters of the APV and APVMUX can be changed online. Examples of APV parameters are:

- the latency, which corresponds to the LV1 latency
- the amplifier parameters
- the APSP filter parameters (in principle two capacitances)

The Tracker FE has in its final design about 80,000 APV readout chips of which each has about 20 parameters. Therefore each version of parameters will contain several Mbytes. With the expected number of versions we arrive at the order of GBytes. The Tracker is organised in modules. Each module has 2 to 6 APVs, 1 PLL chip and 1 channel multiplexer APVMUX. Chips, called CCUs, control the APVs. CCUs[5] communicate through a Token Ring controlled by a FEC[4] board. In the current prototypes the FECs are PCI cards hosted in a PC, finally they should be VME cards. The FE supervisor described above has been called in the specific case of the Tracker FEC supervisor. Figure 3.5 shows the control system of the tracker FE electronics with each of its components. Because they are put in chain, the control modules will receive the trigger signal at different times: see the signal propagation time. In addition to the APV latency, which can be set with 50 *ns* granularity, each PLL has a delay which allows us to set the read out latency with a finer granularity. Therefore the difference between the timestamp of the data read out of an APV and the time of a LV1 trigger depends on two parameters:

- the APV latency, which is the delay of the APV pipeline (see section 2.9)
- the PLL delay

The quality of the detector signal depends obviously on these two parameters: they set the position of the time window, in which the signal is read out. Figure 3.6 shows an example of "delay curves", which represents the ADC count (average in the reading window) versus the read out delay setting. These curves are used to calibrate the latency and the PLL delay. The two curves correspond to two of the six detector modules which were installed in the beam. The effect of an APV latency shift from its optimal value is shown in figure 3.7. In this figure the signal over noise ratio (S/N) distribution is

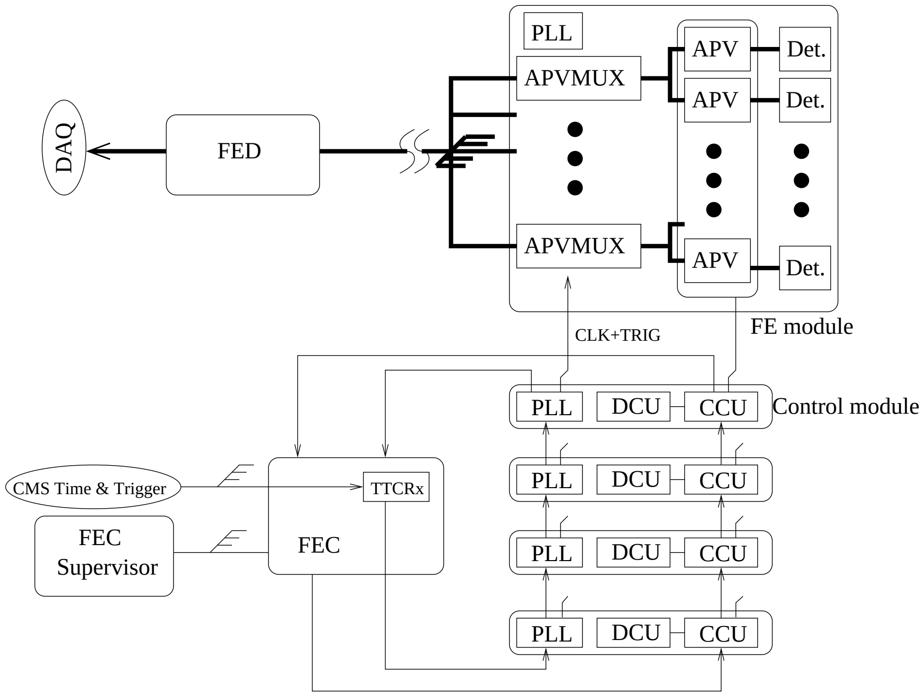

Figure 3.5: Tracker front-end electronics and its controls. The bold lines correspond to the physics data flow: they are produced by the detectors (Det.) and go to the CMS DAQ system. Each Control module is responsible for a FE module (only one is represented in this figure). Each FED concentrates data of 32 APVMUXs. Each FE module can contain from 1 up to 3 APVMUXs.

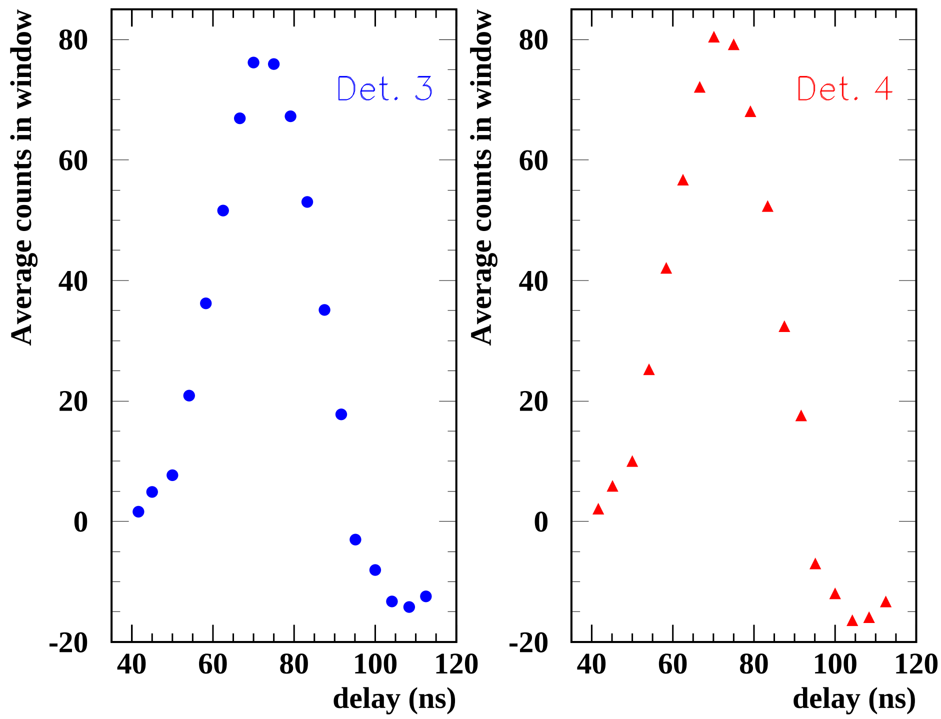

Figure 3.6: Delay curves for two modules plotted during the October 2001 beam test.

represented. The S/N is lower for a $-50\,ns$ shift (right plot) than for a $+50\,ns$ shift (centre plot) because of the asymmetry of the delay curve (see figure 3.6, Det. 3).

3.5.3 FEC supervisor

Java DataBase Connectivity (JDBC) was used to access the database. The choice of JDBC was mainly based on the ease of use of this interface.

3.5.4 Database structure

The hierarchy of all FE electronics is shown in figure 3.8. This hierarchy is reflected in the database through "reference constraints" (see section 3.2). For each item in figure 3.8 a table is defined in the database. The setup has been used successfully in the tracker beam test which took place at CERN in October 2001. Figure 3.9 shows the FE configuration in the context of DCS. During this beam test, PVSS II was also controlling a HV power supply and was monitoring the humidity and the temperature around the detector. A PLC was used to interlock the high voltage depending on the detector temperature. In case of interlock, the PLC was notifying PVSS II in order to generate an alarm. An electronics logbook using an Oracle database with a user interface in PVSS II and a web interface was also been developed for this beam test. Finally a communication between the DAQ and SCADA was implemented in order to synchronise them.

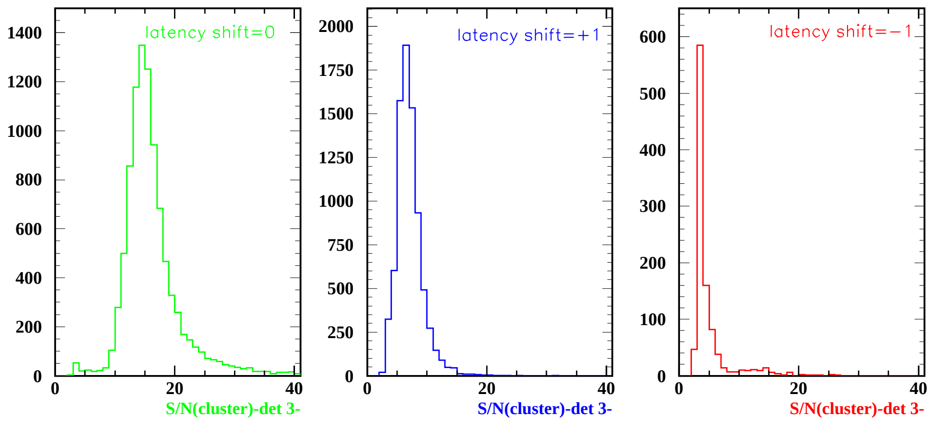

Figure 3.7: Effect of delay shift on S/N distributions. A latency shift of 1 corresponds to a 50 *ns* shift. Oct. 2001 beam test.

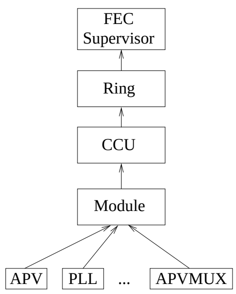

Figure 3.8: Tracker FE electronics hierarchy

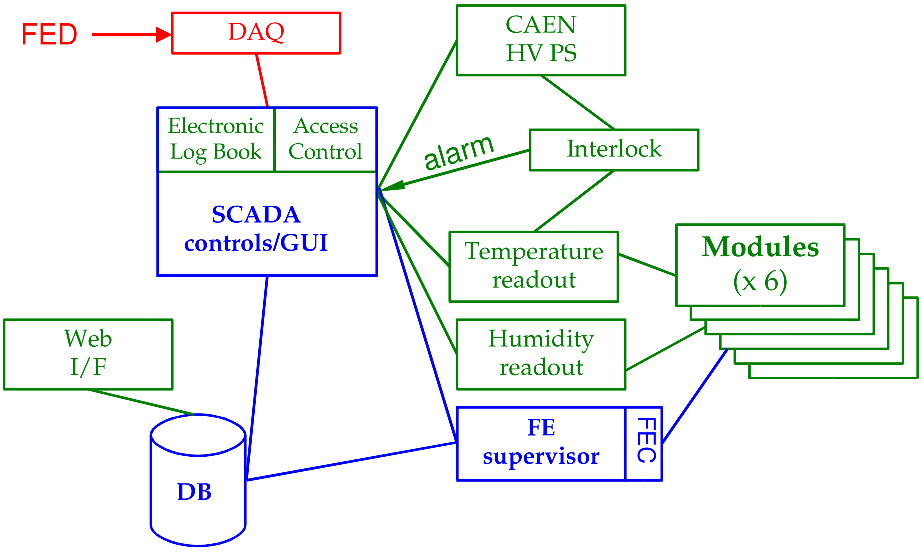

Figure 3.9: Tracker DCS overview. The supervision of the DCS is made by a PC running PVSS II ("SCADA" box), which provides also the user interface. The FE chips are controlled and monitored through the FEC, which is a PCI card plugged into a PC running Linux ("FE supervisor" box). The FE configuration is stored in an Oracle DB managed by a PC running Linux ("DB" box).

3.6 CMS Tracker beam test DCS and run control

The integration of the FE electronics configuration system with DCS was tested at the CMS tracker beam test. The control was based on the tools foreseen for the final CMS DCS.

3.6.1 Tracker DCS overview

In addition to the control of FE electronics, the Tracker beam test required other features:

- High-Voltage used for detector bias
- Temperature alarm
- Humidity monitoring

3.6.2 Controls of High-Voltage power supply

OPC (Object Linking and Embedding for Process Controls) has become a de facto standard to interface control system software to control hardware like PLCs. By defining an interface, based on client-server paradigm, prevents the need of a specific driver for each software/hardware combination. Indeed hardware products need only to be delivered with an OPC driver, called an OPC server and then can be controlled by any software compliant with OPC. OPC is based on the Microsoft Distributed Component Object Model (DCOM) and thus is mainly dedicated to Windows platforms.

The bias HV is provided by a CAEN power supply SY127, connected via proprietary CAENET protocol to an ISA card (CAEN A303A) plugged into a DCS supervision PC. At that time, a CAEN OPC server was not yet available for the old SY127 power supply. A custom OPC server, which I developed, was used to interface the power supply to the SCADA. The user interface for the power supply control was made using PVSS SCADA features.

3.6.3 Temperature alarm

To limit radiation damage, the CMS silicon microstrip tracker must be kept at $-10^{o}C$ during running. When not operated, the temperature can go up above zero for short periods during maintenance. Therefore the tracker will be equipped with numerous temperature sensors for monitoring purposes. Some of these sensors will be used for raising alarms and taking automatic actions (e.g. electronics power-off) in case of a cooling problem. As a system test, a temperature alarm and interlock system was used for the beam test. This system uses a programmable controller NETMASTER from Elsist based on a Dallas TINI module. The TINI module contains a Java virtual machine and the controller can be programed in Java. It has an Ethernet connection which is used for the communication. A $Pt\,100$ sensor is read and monitored by the controller. The alarm decision is taken by the controller and sent to a client running on a PC via the Ethernet connection and using the TCP/IP protocol. The client/PVSS connection was implemented using the PVSSJava interface.

3.6.4 Humidity monitoring

Humidity monitoring was done by legacy software implemented in C language, which wrote the humidity data into files. An existing web server based on a Java servlet gave access to the data stored in the files. This servlet provided the display of the humidity versus time. An interface to the SCADA system based on a PVSS C++ API interface was developed in order to transfer humidity measurements into the SCADA online. This interface, called HummidPVSS, was implemented as a library to link to the legal C application. The modification made to the legacy software code is reduced to the insertion of one call to the new library. This library has been designed such that it is robust against PVSS connection lost and it reconnects automatically. If PVSS connection is not available, the humidity read program can still be started, the connection to PVSS being automatically established as soon it is available. PVSS panels with humidity trending plots were also developed.

3.6.5 Run controls

Although the final CMS Run Controls (RC) will not be implemented using PVSS, for practical reasons the run control of the beam test setup, I implemented, was developed using the same software tools as the DCS. The communication with the DAQ control was implemented using the Distributed Information Management System (DIM) [70, 71], a robust and easy to use network transparent inter-process communication system which was used in the DELPHI and BaBar experiments. It will also be used for the LHC experiments.

Figure 3.10 shows the RC panel. It allows the selection of the run type: physics or calibration, and the versions of the FE electronics configuration to be used. Some DAQ options are also set via the RC interface:

- the maximum number of events per spill
- the number of events after which the run must be stopped (also possible on user request)
- if the data must be saved on disk

Each run is logged into a Oracle database with the version of the electronics configuration used, the type of run, a description entered by the user at run start-up and the start and stop time.

When the user starts a run from the RC interface:

- he is requested to enter a run description
- the electronics configuration is downloaded: the RC sends a request to the FEC supervisor and waits for the successful completion (or failure) of the downloading
- the run number, run type, run description, electronics configuration number and date is entered in Oracle DB
- a run start request is sent to the DAQ control with the type of run and the run number. The run number is generated by the RC

During the run, the DAQ sends regularly the event count to the RC for display purposes.

After a user request to stop the run:

- a stop request is sent to the DAQ control
- the time stamp of the run end is written into the Oracle DB

It is possible to suspend the run: clicking on "Pause" sends a suspend request to the DAQ control. The run could then be resumed on user request.

Conclusion

A general FE electronics configuration system was designed. It was tested with great success during a Tracker beam test. The database designed, with the versioning mechanism, has also been adapted to the ECAL electronics configuration. The FE configuration system was integrated with the DCS framework in such a way that the user had a homogeneous interface to the DCS, whether he was controlling a high voltage power supply or configuring the FE electronics. Nevertheless the dependence on the DCS tools is limited and adapting the system for another environment, such as the run control one, can be done with a minimal effort.

The FE electronics configuration is a key part of the detector read-out chain. This read-out will deliver the data, which will certainly lead to the discovery of the Higgs particle.

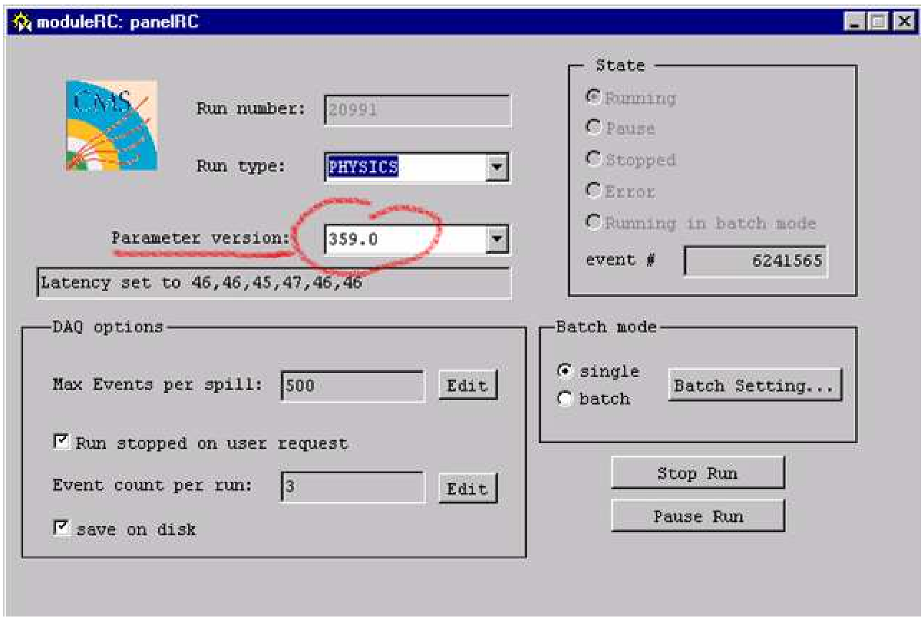

Figure 3.10: Test beam run control panel

Chapter 4

4 b-jet final state MSSM Higgs boson channel

4.1 Introduction

4.1.1 Higgs boson production cross section at LHC

At the LHC pp collider, the standard model Higgs boson is mainly produced in the gluon fusion channel, $pp \to gg \to H$. The Feynman diagrams contributing at leading order to this process are [38, 72]:

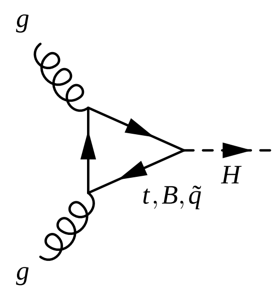

This is still the main Higgs boson production process in the MSSM for low $tan\beta$ values. However, the production associated with two b quarks of the pseudo-scalar Higgs boson A and the heaviest Higgs boson H, $pp \to gg \to A/H\, b\bar{b}$ (see figure 4.1) , are enhanced by a factor $(\tan\beta)^2$ for A and $(\cos\beta)^{-2}$ for H: table 1.3 shows the Higgs boson coupling with heavy quark pairs with their dependence on $\tan\beta$. Therefore for $\tan\beta \gtrsim 10$, these Higgs bosons are mainly produced in association with two b quarks. In this study radiative corrections to the Yukawa coupling will not be taken into account. These corrections depend on many SUSY parameters: $m_{\tilde{b}_1}, m_{\tilde{b}_2}, m_{\tilde{g}} m_{\tilde{t}_1}, m_{\tilde{t}_2}, \mu$. For a detailed description of these corrections see [73].

Figure 4.2 and 4.3 show the production cross section for two values of $\tan\beta$, for the two CP-even states h and H and for the pseudoscalar A. It can be seen on these figures that at $tan\beta = 1.5$ gluon fusion is the dominant Higgs boson production process, while at $tan\beta = 30$ it is the process associated with 2 b-jets.

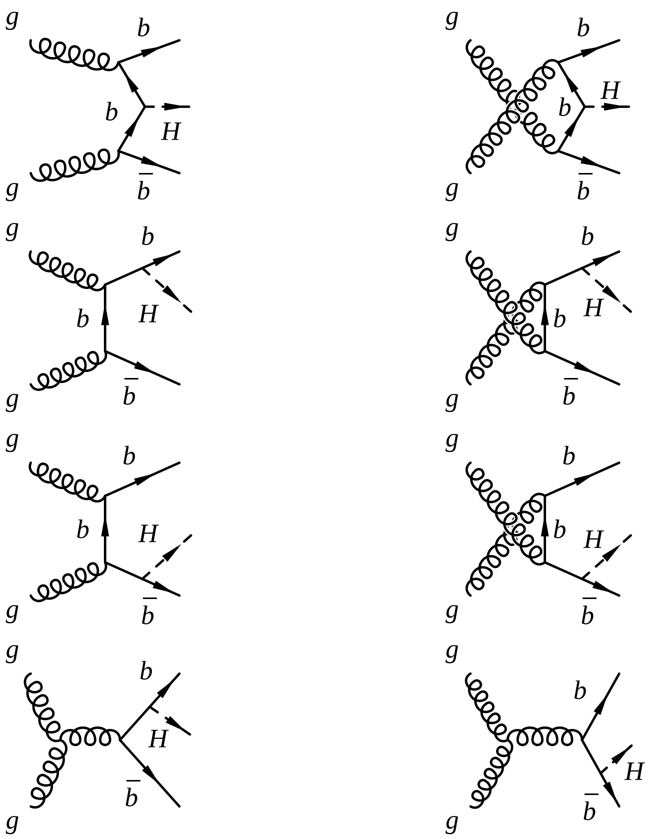

Figure 4.1: Feynman diagrams contributing at tree level to MSSM Higgs boson production associated with 2 *b*-jets.

However, the leading order calculation of $gg \to H/Ab\bar{b}$ is heavily dependent on the scale choice, which means that the uncertainties on this cross-section are quite large. This behaviour is due to a term in $\log \frac{m_{H/A}}{m_b}$ appearing from the exchange of a virtual b-quark. Considering the process $b\bar{b} \to H$ and using b distribution functions with a proper treatment of double counting circumvents this problem [74–77]: the logarithm terms are intrinsically resumed in the heavy quark distribution function. Nevertheless this calculation requires an approximation on the kinematics: b quarks are assumed to be massless and to travel predominantly in forward and backward direction. This approximation can lead to an overestimate of the cross-section [78]. In this study we will use the cross-sections from the leading order full $gg \to H/Ab\bar{b}$ process calculation computed with hqq program [38, 78, 79] with Yukawa coupling evaluated at b pole mass.

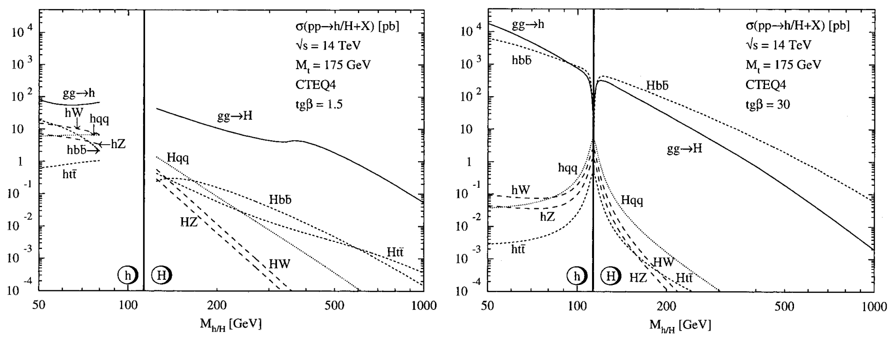

Figure 4.2: Lighter (h) and heavier (H) CP-even MSSM Higgs boson production cross section at LHC [40]. Cross sections are shown for two different $\tan\beta$ values.

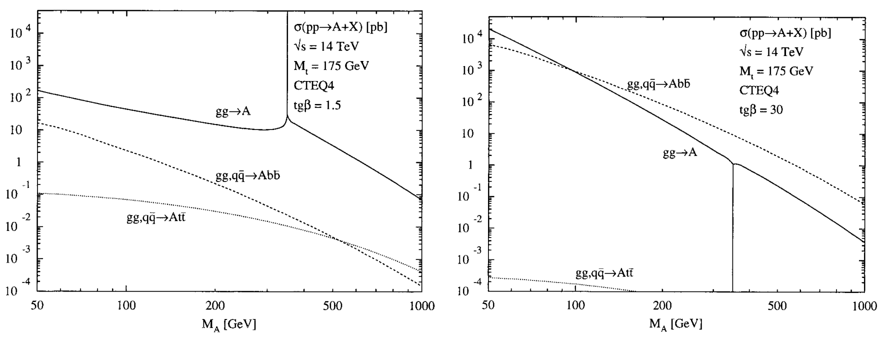

Figure 4.3: pseudo-scalar MSSM Higgs boson cross-section at LHC [40]. Cross-section are shown for two different $\tan\beta$.

4.1.2 MSSM Higgs boson decay

Figure 4.4 shows the branching ratio of the various decay channels of H and A in no stop mixing scenario for high $\tan\beta$ ($\tan\beta = 40$). If the mass threshold for decays into neutralinos is not yet reached then $\sim$ 90% of the H/A Higgs bosons decay into a $b\bar{b}$ pair.

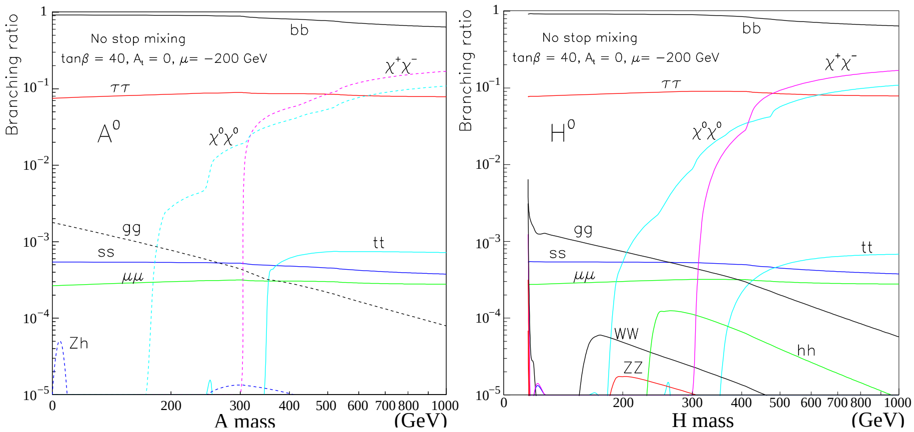

Figure 4.4: A/H MSSM Higgs boson decay branching ratios [80, 81].

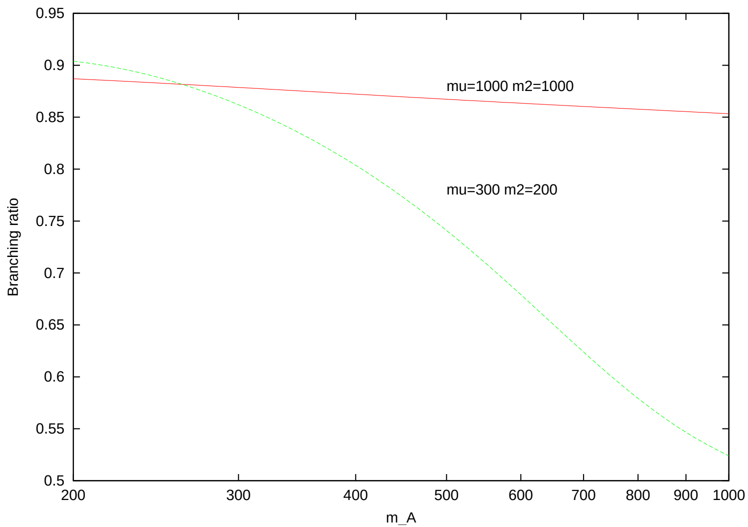

Figure 4.5: $H \rightarrow b\bar{b}$ branching ratio in maximal mixing scenario with $tan\beta = 30$. This plot compares two choices of (μ, M_2) pair. The decrase with the Higgs boson mass in the case $M_2 = 200$ is due to the decay in neutralinos.

Once the mass threshold has been passed, the decay to neutralinos can be important and the $b\bar{b}$ branching ratio is decreasing [82]. Figure 4.5 compares the $b\bar{b}$ decay branching ratio for a moderate neutralino mass (with higgsino parameter $m_2 = 200\,GeV$) and for a high neutralino mass (with higgsino parameter $m_2 = 1000\,GeV$).

In this study we will consider the maximal mixing scenario with $\mu = M_2 = 1000$ and $M_{SUSY} = M_{\tilde{g}} = M_Q = M_U = M_D = 1\,TeV$, as in [32], avoiding this way decays in gauginos.

In this section, we propose to study the A/H Higgs boson channel with the Higgs boson produced with two associated b-jets and the Higgs boson decaying in 2 b-jets, that is with a final state made of 4 b-jets. In the studied $(m_A, \tan\beta)$ region A and H Higgs boson have almost the same mass and the two masses cannot be distinguished.

4.2 Simulation tools and analysis methods

4.2.1 CMS detector simulation

In this study, the CMS detector response will be simulated with the "fast simulation" package CMSJET [83]. CMSJET simulation is parametrised according to the full CMS simulation (CMSIM [84]) itself based on Geant [85]. Simulation of the electromagnetic and hadron calorimeters (for jet reconstruction) and of the tracker (for track impact parameters used in b-tagging) are used.

The details of the detector response parametrisation can be found in [83].

4.2.2 Jet reconstruction

The modified UA1 jet-finder algorithm implemented in CMSJET [83, 86, 87] is used to reconstruct the jets.

- Calorimeter cells with a transverse energy deposit above a threshold $E_t^{calo\ threshold}$ depending on the calorimeter (HCAL, ECAL or HE) and muons above a threshold $E_t^{muon\ threshold}$ are used as seeds. For muons, the energy obtained from the generation is used, muon chambers are not simulated. A hit will be defined as a calorimeter cell where some energy has been deposited.

- These seeds are ordered according to decreasing E_t.

- Preclusters of seeds are built the following way: at start up there is no precluster. The seed list is scanned starting from the first element, if the seed is inside one or several precluster cones, then it is assigned to every one of these preclusters[1], otherwise a new precluster is formed and this seed is assigned to it. The energy-momentum four-vector of the precluster is the sum of the energy-momentum four-vectors of the seeds which were assigned to it; it is updated each time a hit is assigned to the precluster. The precluster cone is defined as the set of momenta P such that $\Delta R = \sqrt{\Delta\varphi^2 + \Delta\eta^2} \leq \Delta R^{jet\ reconstruction}$, where $\Delta\varphi$ is the angle in the transverse plane between P and the precluster momentum and $\Delta\eta$ is the pseudo-rapidity difference between the P and the precluster momentum.

[1] Actually a hit can be assigned to a maximum of 3 preclusters, if it is inside to more than 3 preclusters, then it is assigned in priority to precluster built in first.

Parameter	value
$E_t^{ECAL\,threshold}$	$0.5\,GeV$
$E_t^{HCAL\,threshold}$	$1.0\,GeV$
$E_t^{VFCAL\,threshold}$	$1.0\,GeV$
$E_t^{muon\,threshold\,a}$	0
$E_t^{precluster\,threshold}$	$5.0GeV$
$\Delta R^{jet\,reconstruction}$	0.4
$\alpha_{overlap}$	75%

[a] Muon chambers are not simulated, momentum from generation is taken as such from generation.

Table 4.1: Jet finding algorithm parameters.

- Hits which were not selected as seeds but are inside one or several preclusters are assigned to them (still to a maximum of 3 preclusters) in order to form the clusters.

- Clusters with transverse energy below a threshold, $E_t^{precluster\ threshold}$, are discarded.

- Overlapping clusters are merged if they share more than $\alpha_{overlap}$ of the transverse momentum of one of the precluster, otherwise they are split.

The values for the jet finding algorithm parameters which were used are listed in table 4.1.

4.2.3 Jet energy correction

CMSJET does not calibrate jets. Therefore the reconstructed jet energy distribution is shifted toward lower values: energy deposited outside the reconstruction cone is systematically discarded.

To recover from this jet energy bias, a scale factor depending on the measured jet energy and pseudo-rapidity can been applied to the jet four-momentum absolute values.

This scale factor has been parametrised with a polynomial in 10 different $|\eta|$ bins in the$|\eta| \in [0,2.5]$ range. Jets outside of this pseudo-rapidity range will be used only to select events and a bias on their energies is not penalising.

A simulation of the signal ($A/H b\bar{b} \to \bar{b}b\bar{b}b$), for $m_A = 600\,GeV$, with initial and final state radiation switched off were used to calculate the scale factors, $C(E,\eta)$. With real data, jet energy calibration will be done with events like γ-jet, Z^0-jet and top decay exploiting the W boson and top masses [61]. The $C(E,\eta)$ factor was defined as the ratio of the mean value of the parton energy over the mean value of the reconstructed jet energy. $C(E,\eta)$ versus E obtained from this simulation has been fitted by a polynomial $P_\eta(E)$ in each η bin for $E \in [50,500\,GeV]$. $C(E,\eta)$ is then defined as:

$$
\begin{aligned}
C(E,\eta) &= P_\eta(50\,GeV) && \text{for } E \leq 50\,GeV \\
C(E,\eta) &= P_\eta(E) && \text{for } E \in [50,500\,GeV] \\
C(E,\eta) &= P_\eta(500\,GeV) && \text{for } E \geq 500\,GeV
\end{aligned}
$$

4.2.4 Identifying bottom jets

Identifying *b*-jets among jets of other flavors is called *b-tagging*. This is done by exploiting the relatively long lifetime of the bottom hadrons: at rest the mean lifetime is about $1.5 \cdot 10^{-12}s$, i.e. $c \cdot \tau \simeq 0.5\,mm$ [88], see table 4.2. A *b*-particle with a momentum $|\vec{p}| = 100\,GeV$ will flight on average about $0.9\,cm$ in the lab frame. This means that two vertices can be distinguished: the first one being where the *b*-particle has been produced, that is the collision vertex, the second one being where the *b*-particle has decayed.

particle	mean lifetime at rest (τ in ps)	$c \cdot \tau$ at rest (mm)	mean decay length for a particle with a momentum $p = 100\,GeV$ (mm)
B^+	1.674 ± 0.018	0.502	9.51
B^0	1.542 ± 0.016	0.462	8.75
B_s^0	1.461 ± 0.057	0.438	8.16
Λ_b^0	1.229 ± 0.080	0.368	6.54
$B^+/B^0/B_s^0/b-baryon/CP\ conjugates$ admixture at high energy (LEP, Tevatron, Sp$\bar{\text{p}}$S)	1.564 ± 0.014	0.474	$\sim$ 8.8 (assumes an average mass of $5.4\,GeV$)

Table 4.2: mean lifetimes and decay lengths of *b* mesons and baryons [88].

The long lifetime of the bottom particles can be exploited to identify *b*-jets.

To *b*-tag a jet, we must look at the tracks it is made of and identify if they are coming from a bottom particle decay. The impact parameter can be used as a criterion to identify a track as coming from a bottom particle decay. As shown in figure 4.6 the 3-D impact parameter of a track is the shortest distance of the primary vertex to the reconstructed track. Tracks coming from the primary vertex will have an impact parameter within the detector resolution, while tracks from a bottom particle decay will have a significant non-zero impact parameter. A sign can be defined for the impact parameter. If the point of the track closest to the primary vertex is in front (resp. behind) of the latter relative to the jet direction, then a positive (resp. negative) sign is assigned to the impact parameter. As the measurement resolution of the impact parameter depends strongly on the momentum, a better criterion to identify a track as coming from the decay of a bottom particle is the impact parameter significance. The impact parameter significance, denoted $\sigma(ip)$, is defined as the ratio of the measured impact parameter by its measurement error. There are two different ways to use this impact parameter significance criterion:

- a threshold can be applied on the impact parameter significance: track with an impact parameter significance above this threshold are assigned as *b*-tracks, the others as non-*b*-tracks [89].

- or a probability to come from the decay of a bottom particle, called *b*-probability, can be assigned to each track according to the value of their impact parameter.

In the former case, a jet is tagged as a bottom jet if it contains at least a certain number (typically 2 or 3) of *b*-tracks. This method is called *track counting method*. In the latter case the probability that the jet is a *b*-jet can be derived from the *b*-probabilities of the individual tracks. The jet is then tagged as a *b*-jet if its *b*-probability is greater than a given value.

The impact parameter can be also defined as the *z*-component (longitudinal) of the 3-D impact parameter, or as the projection of the 3-D impact parameter in the *xy*-plane (transverse impact parameter). The transverse impact parameter has the advantage of not requiring the reconstruction of the primary vertex and it is not affected by event pile-up.

Jets can also be tagged by reconstructing the secondary vertex.

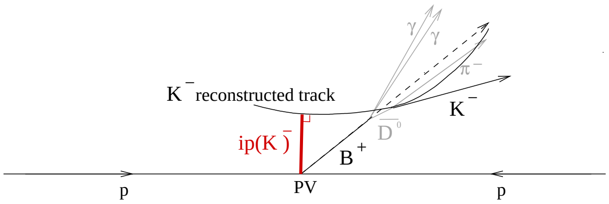

Figure 4.6: impact parameter. The distance $ip(K^-)$ is the impact parameter of the K^- track.

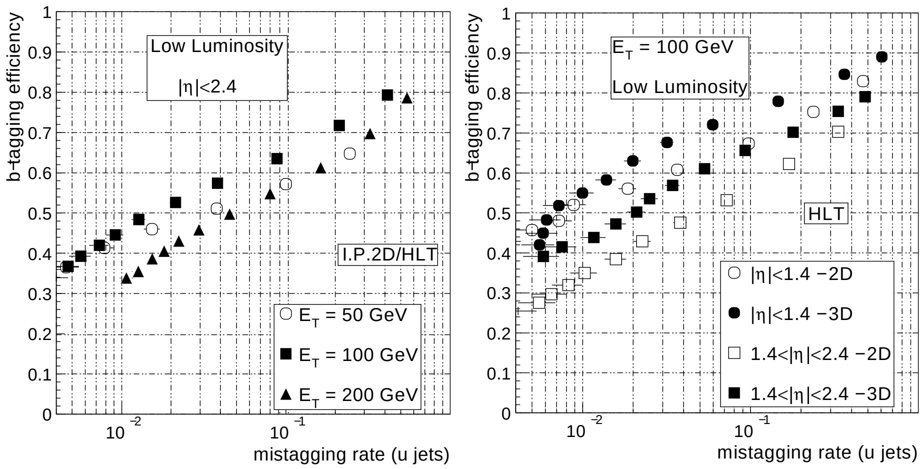

Figure 4.7: *b*-tagging performance of CMS at low luminosity. *b*-tagging efficiency versus *u*-mistagging is plotted for different transverse energy and different pseudo-rapidity regions. *xy* and 3-D *b*-tagging are compared on the right plot [61].

To evaluate the tagging quality we define two quantities:

- the *b*-tagging efficiency, ε_b: the probability to tag a real *b*-jet as a *b*-jet. The estimator of this quantity is:

$$\hat{\varepsilon}_b = \frac{\text{number of tagged real-b jets}}{\text{number of real-b jets}}$$

Trigger	95% efficiency value	threshold on measured E_t
single jet	177 GeV	135 GeV
three-jet	86 GeV	104 GeV
four-jet	70 GeV	85 GeV

Table 4.3: Jet LV1 trigger E_t thresholds [61].

- the mistagging probability, ε_{non-b}: the probability to tag a non-b-jet as a b-jet. The estimator of this quantity is:

$$\hat{\varepsilon}_{non-b} = \frac{\text{number of tagged non-b jets}}{\text{number of non-b jets}}$$

It can be convenient to distinguish:

- the u-mistagging probability, ε_u: the probability to tag a u-jet as a b-jet
- the c-mistagging probability, ε_c: the probability to tag a c-jet as a b-jet

Indeed the latter is much higher to the former due to the lifetime of charm hadrons.

Figure 4.7 shows the tagging performance of CMS detector calculated from a full detector response simulation. In principle if 1% of u-mistagging probability is tolerated, the tagging efficiency averaged over the full detector acceptance is better than 58% using a xy impact parameter b-tagging (see left plot). However we can see on the right plot that b-tagging is worse in forward region of the detector than in central region. The right plot shows also that by using 3-D impact parameter instead of 2-D one gains 10% of efficiency. A 2D b-tagging can be performed already by the High Level Trigger.

4.2.5 Inclusive b-trigger simulation

The four-b final state MSSM A/H Higgs boson channel can be triggered at level one by the jet trigger, mainly by the single jet trigger. The foreseen CMS LV1 trigger thresholds are shown in table 4.3. The LV1 trigger jet thresholds are defined by their 95% efficiency values, $E_t^{95\%}$. This value means that for a n-jet trigger, the LV1 threshold on measured E_t of the nth-highest-E_t jet will be set such that 95% of the events containing n jets with a transverse energy E_t^{gen} greater than $E_t^{95\%}$will pass the trigger. The jet definition used to calculate E_t^{gen} is defined, at generation level, as the set of particles inside a cone of size $\Delta R = 0.5$. The measured E_t thresholds corresponds to the transverse energy values of jets reconstructed after full simulation of the detector response and after a scale calibration. This jet calibration, which is described in [61], consists of scaling the jet four-momentum norm according to its transverse energy and pseudo-rapidity by a factor $E_t^{gen}/E_t^{measured}$.

B-tagging at HLT is required for this four-b channel. The Data acquisition and high-level trigger TDR [61] proposes for HLT inclusive b-jet trigger:

- at least one jet tagged as follow,
- for jets with $E_t < 80\,GeV$, 2 tracks with 2-D impact parameter significance (see 4.4.3) $\sigma(ip) > 1.5$

- for jets with $80 < E_t < 150\,GeV$, 2 tracks with 2-D impact parameter significance $\sigma(ip) > 2.0$
- for jets with $E_t > 150\,GeV$, 2 tracks with 2-D impact parameter significance $\sigma(ip) > 2.5$

To meet the bandwidth constraints, the HLT will require an additional E_t cut on the leading jets. A $5\,Hz$ rate can be obtained by applying a cut of $160\,GeV$ on the measured E_t of the 2^{nd} highest-E_t jet [61]. The other $5\,Hz$ stream menu proposed in [61] with a cut at $237\,GeV$ on the measured E_t of the highest E_t jet will not be considered. It should be noted here that such a single jet cut would be rather penalising for this channel for Higgs boson masses below $\sim 500\,GeV$.

The trigger has been included in the simulation by using the impact parameter significance given by the FATSIM [90] part of CMSJET and using the E_t obtained from CMSJET as "measured" E_t. The LV1 trigger with single jet, three jets and four jets were included. For HLT the impact parameter trigger has been implemented using the three E_t regions and the threshold on the second highest-E_t jet was applied. Trigger simulations must be a bit pessimistic because the threshold on measured E_t of the LV1 and HLT are given for calibrated jets and they were applied on uncalibrated ones. The trigger efficiency will be discussed in 4.4.4.

4.3 Event reconstruction

4.3.1 Signal topology

In this study the signal was generated with Pythia 6.203 [91] using the $gg \to Hb\bar{b}$ process.

Figure 4.8 shows the topology of a typical event for a Higgs boson mass, $m_A = 600\,GeV$: transverse momenta p_t of the four partons are plotted versus the angle in the transverse plane φ and the pseudo-rapidity η. This plot is done at parton level with *final and initial state radiation turned off*. In this event the two back-to-back ($\Delta\varphi = 3.23$) high-p_t jets are coming from the Higgs boson decay, the two soft ones from the Higgs boson production $b\bar{b}H$.

Looking at the distribution of the $\Delta\varphi$ angle in the transverse plane between the two partons produced in the Higgs boson decay, it can be seen that for most of the events the two partons are back-to-back: the most probable $\Delta\varphi$ angle value is 3.10 ± 0.03. However the angular distribution is rather broad: for 50% of the events this angle is less than 2.9. This distribution is wide because —in spite of the Higgs boson mass— there is enough energy to give transverse momentum to the Higgs boson. This can be seen on the p_t distribution of the produced Higgs boson in figure 4.9.

Because its decay $b\bar{b}$ products are light compared to the Higgs boson mass, they are expected to have a large momentum and this is confirmed by their p_t distribution shown in figure 4.11 (a).

On the other hand the two other b-jets being produced together with a heavy particle, should be soft (that is with a relatively low transverse momentum in the c.m.). This is verified on their p_t distribution shown in figure 4.11 (b).

Figures 4.12 and 4.13 show the corresponding jet transverse momentum distributions after detector response simulation. To identify which jets are coming from Higgs boson decay and which ones are coming from Higgs boson production, the jets have been matched with the partons the following way (subroutine QJMAT of CMSJET):

- the algorithm loops over the jet list (p_t ordered) starting from the highest-p_t one
- if a b-quark is inside the cone $\sqrt{\Delta\varphi^2+\Delta\eta^2} \leq 0.4$ around the jet axis, then the jet is marked as a b-jet and is matched with this quark. If there are several such $b-$quark then the highest-p_t one is selected
- if there is no such b-quark then the jet is matched with the highest-energy quark inside the cone

Once a jet has been matched with a b-quark, then the generator particle history listing (PYLIST) is consulted to find out the origin of the quark. The shown histograms corresponds to 10^5 generated events and are rescaled to represent te expected number of events with 60 fb^{-1}. Only events whose four b-jets (from Higgs boson production and decay) have been reconstructed with the jet algorithm within the detector acceptance, have been retained: without final and initial state radiation 37% of events would have their four jets reconstructed with the jet algorithm within the detector acceptance, but with final and initial state radiation this rate falls down to 29%.

The distributions of the parton transverse momentum for the same events is also shown (in dashed line) in figures 4.12 and 4.13 .

Concerning the pseudorapidity distributions, the soft jets should be rather affected by the collision boost and therefore have a wide-spread pseudorapidity distribution: the distribution obtained from the generations presented in figure 4.14(b) shows that the most probable value of $|\eta|$ is 2.35 and that 50% of the events have one of the jets coming from the Higgs boson production with $|\eta| \geq 2.4$. Conversely, the jets from the Higgs boson decay should be less affected by the longitudinal boost and therefore be more central (that is a narrower distribution centred on $\eta = 0$). Figure 4.14(a) shows the pseudo-rapidity distribution for these jets: the distribution is centred at 0, as expected, with a variance of 1.28, 95% of the events have at least one jet produced in the Higgs boson decay with $|\eta| \leq 2.4$, i.e. within the pseudo-rapidity region where impact parameters, needed for b-tagging, can be measured with the tracker. Figure 4.15 and 4.16 show the same distributions but after detector response simulation and jet reconstruction (solid line plots). The pseudo-rapidity distribution of the Higgs boson decay jets is barely affected by the detector response and the initial and final state radiation: see figure 4.15. The distribution of the b-jets associated to Higgs boson production is cut by the detector acceptance. The two peaks cannot anymore be distinguished, this shape change is due to the missing events, those which do not have their four jets detected by the calorimeters: figure 4.16 shows the jet pseudo-rapidity distribution. The parton pseudo-rapidity distribution for the same events is superposed onto the plot (in dashed line).

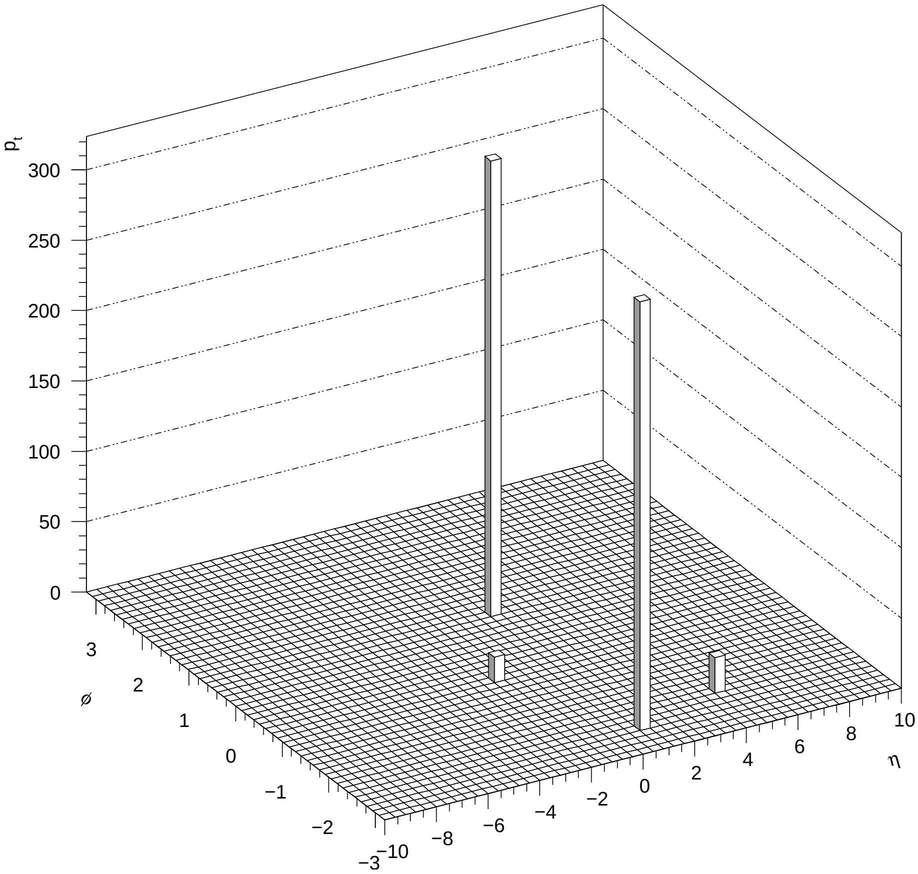

Figure 4.8: Example of an event topology. This figure shows the P_t of the final state b-partons of a $b\bar{b}H/A$ event generated without initial and final state radiation versus (φ, η). $m_A = 600\,GeV$

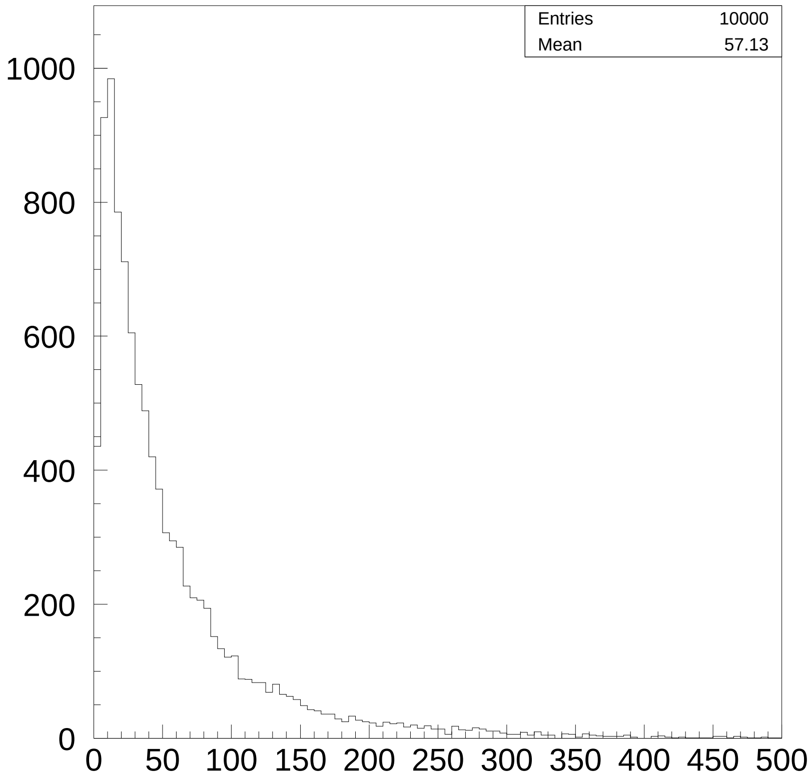

Figure 4.9: Transverse momentum distribution of the Higgs boson generated with Pythia. $m_A = 600 GeV$

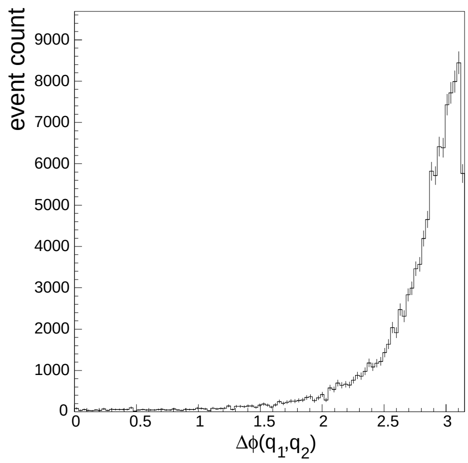

Figure 4.10: Angle φ in transverse plane between the two decay products of the Higgs boson ($A/H \to b\bar{b}$), at parton level, without initial and final state radiations. $m_A =$ 600GeV

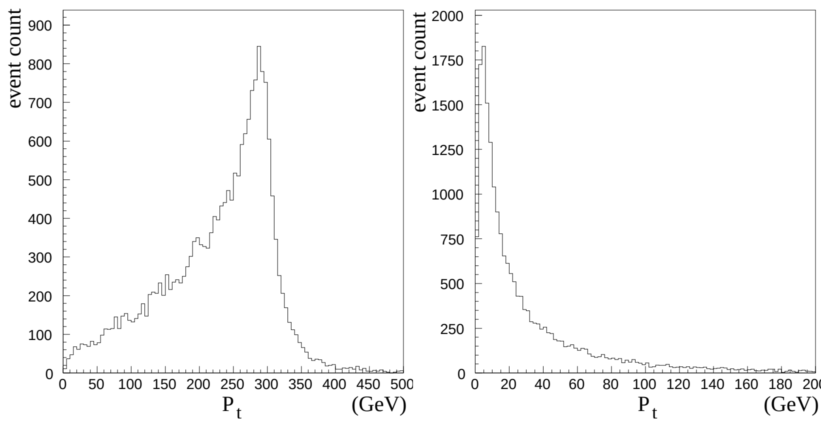

(a) Products of Higgs decay

(b) Partons associated to Higgs production

Figure 4.11: Transverse momentum distribution of the four $b-$partons of the $A/Hb\bar{b}$ signal for $m_A = 600GeV$.

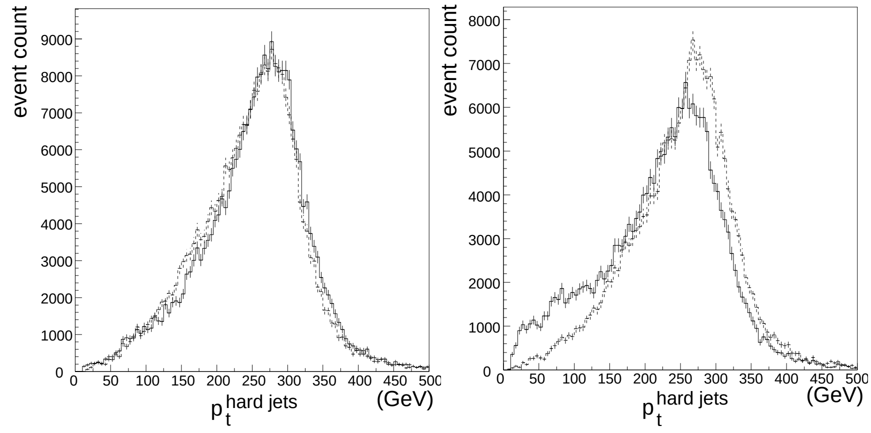

(a) without initial and final state radiations (b) with initial and final state radiation

Figure 4.12: Transverse momentum distribution of the jets produced in Higgs boson $H \rightarrow b\bar{b}$ decay obtained with the detector simulation for $m_A = 600\,GeV$. The jets have been identified as such by matching them to the partons as described in the text. The distributions include the 2 jets without distinction. Dashed curves correspond to p_t distributions of the matched partons. Scale and missing-E_t (see section 4.3.3) correction have been applied on the jets.

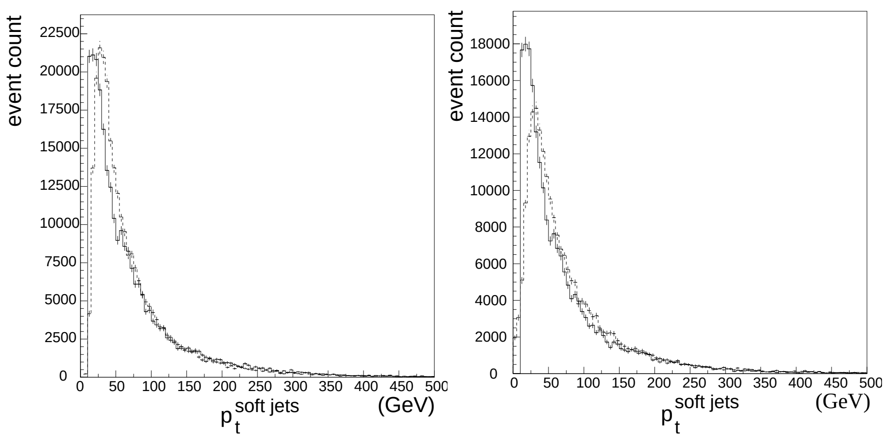

(a) without initial and final state radiations (b) with initial and final state radiation

Figure 4.13: Transverse momentum distribution of the jets associated to the Higgs boson production obtained in $b\bar{b}H/A$ final states with the detector simulation for $m_A = 600\,GeV$. Dashed curves correspond to the p_t distribution of the matched partons. The distributions include the 2 jets without distinction. Scale and missing-E_t (see section 4.3.3) correction have been applied on the jets.

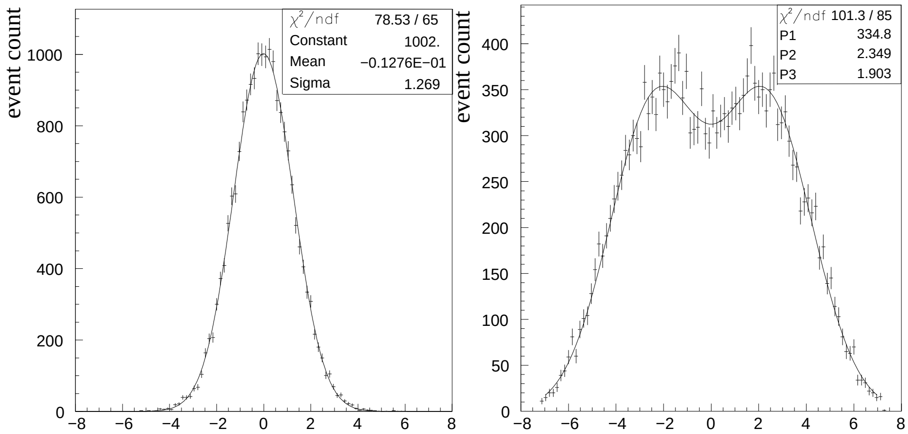

(a) b-partons produced in the Higgs boson decay

(b) b-partons associated to Higgs boson production in $b\bar{b}H$ final states

Figure 4.14: Pseudo-rapidity distribution of the four $b-$partons of the $b\bar{b}H/A$ signal for $m_A = 600\,GeV$. Final and initial state radiation are switched off. The distribution (a) is fitted by a Gaussian, the distribution (b) is fitted by the sum of a Gaussian and its symmetrical against the y-axis: $P_1 \cdot (e^{-\frac{1}{2}(\frac{x-P_2}{P_3})^2} + e^{-\frac{1}{2}(\frac{x+P_2}{P_3})^2})$.

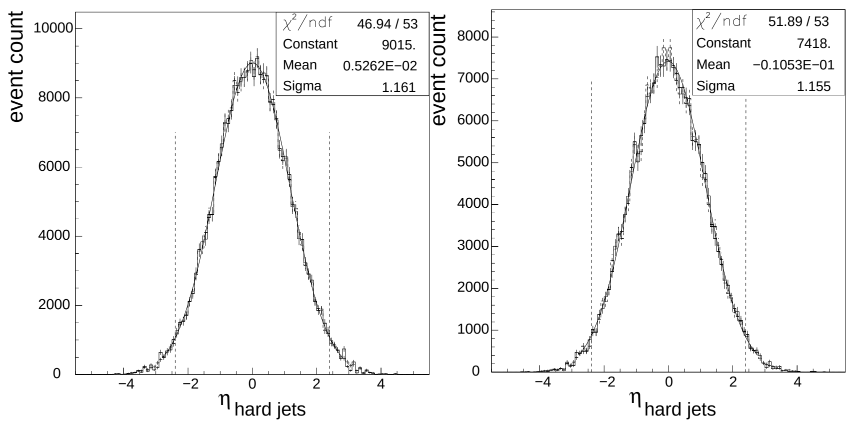

(a) without initial and final state radiations

(b) with initial and final state radiation

Figure 4.15: Pseudo-rapidity of the jets produced in the $A/H \to b\bar{b}$ decay obtained with the detector simulation. Fluctuations around $\eta = 3$ correspond to the transition between HE and HF calorimeters. Dashed curves correspond to the η distribution of the matched partons. Jet η distributions have been fitted within $\eta \in [-2.8, 2.8]$ and are thus limited to a region covered by HB and HE. $m_A = 600\,GeV$. Scale and missing-E_t (see section 4.3.3) correction have been applied on the jets.

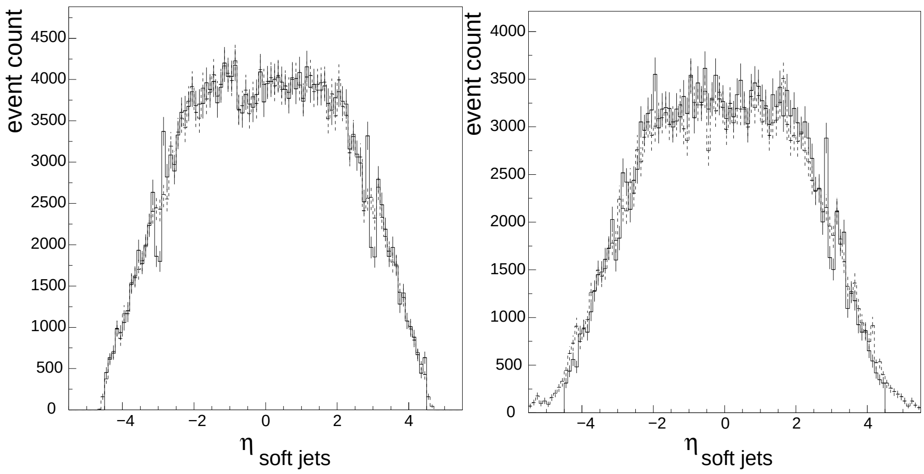

(a) without initial and fi nal state radiations

(b) with initial and fi nal state radiation

Figure 4.16: Pseudo-rapidity of the jets associated to the Higgs boson production obtained with the detector simulation. Dashed curves correspond to the η distribution of the matched partons. The distributions include the 2 jets without distinction. Fluctuation around $\eta = 3$ corresponds to the transition between HE and HF calorimeters. $m_A = 600\,GeV$. Scale and missing-E_t (see section 4.3.3) correction have been applied on the jets.

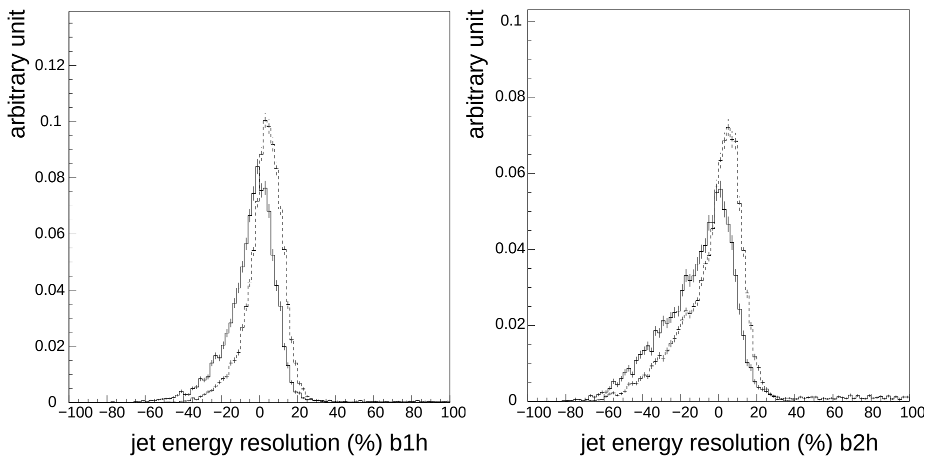

(a) higher p_t jets of the two

(b) Lower p_t jet of the two

Figure 4.17: Jet resolution for the jets produced in the Higgs boson$\rightarrow b\bar{b}$ decay with jet correction described in section 4.2.3. In dashed line, without initial and final state radiation, in solid line with them. $m_A = 600\,GeV$

4.3.2 Jet resolution

Figure 4.17 shows the jet energy resolution for the two jets coming from Higgs boson decay. The jet energy resolution is defined as:

$$\frac{jet\ energy - quark\ energy}{quark\ energy}$$

Same plots are shown in figure 4.18 without the jet correction.

4.3.3 Higgs boson mass reconstruction

The criterion for signal presence in this study will be based on the distribution of the reconstructed Higgs boson mass. The reconstructed Higgs boson mass is the invariant mass of the two jets, which are believed to come from the Higgs particle decay. The signal significance, $S/\sqrt{B}$ will be calculated in the mass window which maximises this ratio. We will consider in this section Higgs bosons with a mass $m_A = 600\,GeV$.

The reconstructed mass distributions before any cut and correction is compared to the real Higgs boson mass distribution (due to natural width and generated with Pythia) in figure 4.19. The natural width (FWHM of a Breit-Wigner distribution) —obtained from the fit shown in figure 4.19(a)— is $19.1\,GeV$. A Gaussian with the same FWHM would have a variance $\sigma = 19.1/2.355 = 8.11$. On the other hand, after the detector response simulation, with the initial and final state radiation included and before any cut and correction, the FWHM of the reconstructed mass is $212 \pm 25\,GeV$. This width comes from:

- detector resolution

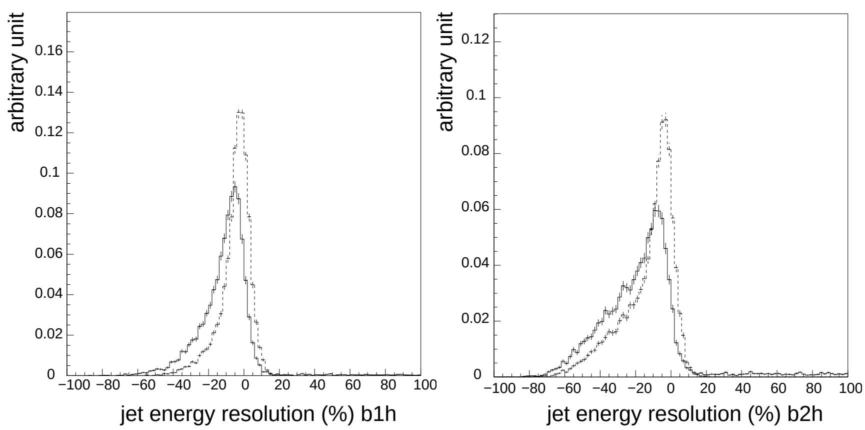

(a) higher p_t jets of the two

(b) Lower p_t jet of the two

Figure 4.18: Jet resolution for the jets produced in Higgs boson decay without jet correction described in 4.2.3. In dashed line, without initial and final state radiation, in solid line with them. $m_A = 600\,GeV$

- initial and final state radiations as already shown in figure 4.19(b)
- semi-leptonic decays of b's, escaping ν's diminishing systematically the measurable jet E_t

When the selection cuts described in section 4.4 are applied then the mass resolution is improved: the low-mass tail is cut by the transverse momentum cuts. Figure 4.20 show the mass resolution after the cuts. Because without jet correction the jet energies are lower, the p_t used to plot the mass distribution without jet correction are lower than the one given in section 4.4: $180\,GeV$ instead of $200\,GeV$ on the second highest p_t-jet. This cut value have been optimised to get the best statistical significance when no jet correction is applied. The mass resolution is 10.23% and the mass mean is $530.7\,GeV$. The mass distribution have been fitted by a sum of three Gaussians. The Gaussian containing the upper mass tail have been discarded and the mass mean has been defined as the mean of the distribution composed of the two remaining Gaussians. The resolution is defined as the RMS of this distribution divided by its mean. When jet corrections are applied (see figure 4.21) the mass mean is getting closer to the $600\,GeV$ Higgs boson mass: $571\,GeV$ has been obtained. The mass resolution is also improved.

Missing energy, due to semileptonic decays of bottom particles contributes also to the reconstructed mass width. Figure 4.23 shows the contribution to the mass resolution of events with different missing energy; by comparing the four histograms of this figure one see that the distribution of the reconstructed Higgs boson mass is shifting toward lower values when the missing energy is increasing. Therefore, events with missing energy contributes to the lower tail of the reconstructed Higgs boson mass. It must be noted that for the plots of figure 4.23 the missing transverse momentum cuts are applied on the generated values and not on the measured ones. A simple correction is applied to recover from this resolution loss when the missing energy is mainly due to the semileptonic decay of a single b:

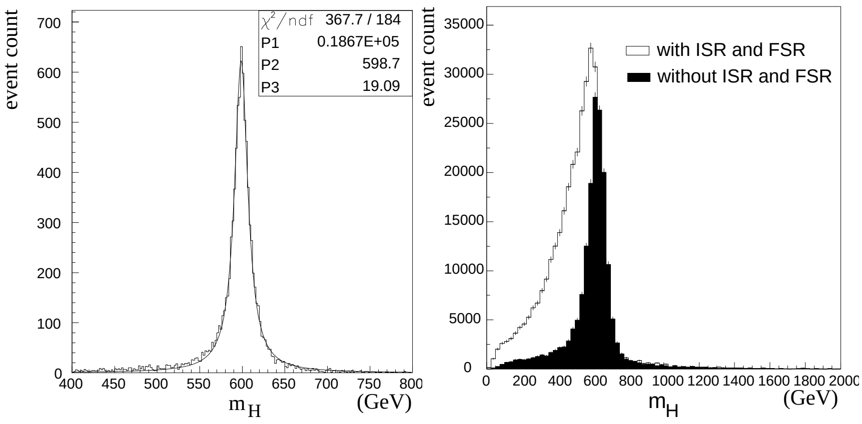

(a) from generation, $m_A = 600\,GeV$ (b) from detector simulation, $m_A = 600\,GeV$

Figure 4.19: Higgs boson mass distribution. The distribution of figure a is fitted with a Breit-Wigner functions: $P_1 \frac{P_3}{(X-P_2)^2+(P_3/2)^2}$. Except the requirement to have at least four jet, no cut is applied. No jet correction is applied.

- if the $\Delta\varphi$ angle in (x,y)-plane between the missing energy and a b-jet is less than $\Delta\varphi^{cut}_{miss} = 0.9$ then the following correction is applied
- the projection on the jet direction of the transverse missing momentum is added to the jet transverse momentum, we get p_t^{corr}.
- the jet momentum is scaled up in order that its transverse momentum is equal to p_t^{corr}. We get $p^{corr} = p \cdot \frac{p_t^{corr}}{p_t}$.

The correction is only applied if the measured missing energy is greater than $30\,GeV$. Indeed below this value the missing energy resolution is too poor to apply the correction. Figure 4.22 shows the reconstructed Higgs boson mass after the missing energy correction: this correction improves the mass resolution from 9.79% to 8.67%. The mass mean goes to $601\,GeV$.

The reconstructed mass distribution contains still a tail toward high-masses, which is explained by combinatorial background, that is, by a bad choice of the 2 jets to reconstruct the mass. It is hard to improve this jet selection without introducing a bias, which will increase the number of background events whose reconstructed mass is close to the Higgs boson mass.

In summary the jet correction applied improves the mass resolution from 10.23% to 8.67%, and recentres the mass distribution peak to about the input Higgs boson mass.

4.4 Selection and triggering

4.4.1 Channel signature

Because of the high mass of the Higgs boson and low mass (compared to the Higgs boson) of the b quarks, the b-jets associated to its production will be soft, and for the

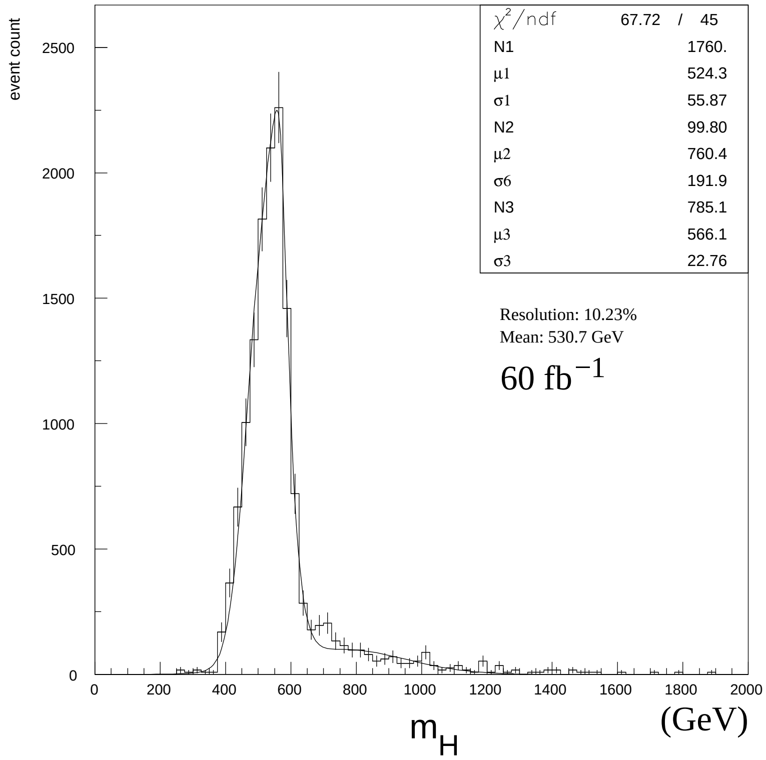

Figure 4.20: Reconstructed Higgs boson mass before any jet correction. The distribution is fitted by a sum of three Gaussians, $N_i e^{-\frac{1}{2}\left(\frac{x-\mu_i}{\sigma_i}\right)^2}$. Resolution and mean have been calculated with Gaussians $i = 1$ and $i = 3$. $\mathcal{L} = 60\, fb^{-1},\ m_A = 600\, GeV,\ \tan\beta = 100$.

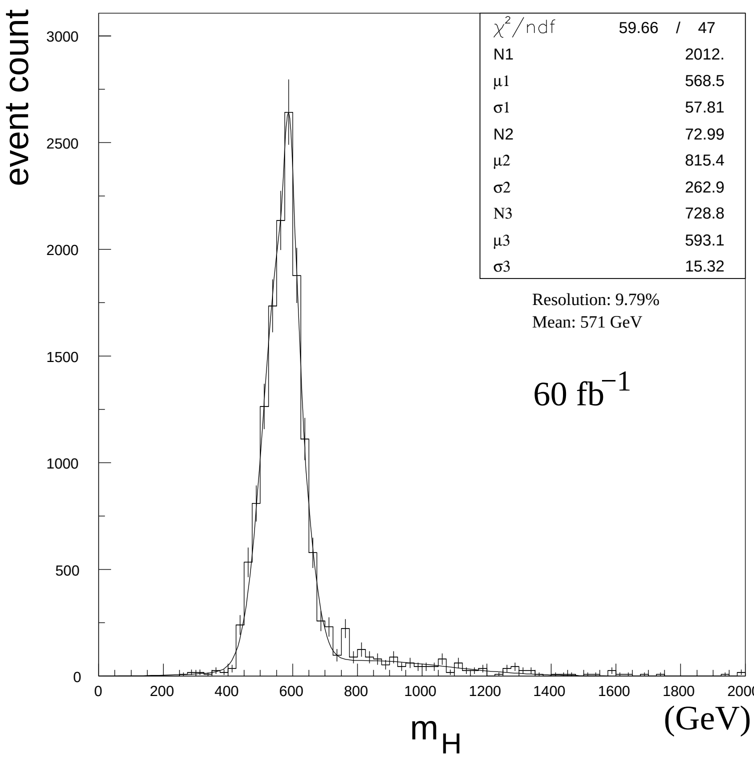

Figure 4.21: Reconstructed Higgs boson mass after jet energy scale correction. The distribution is fitted by a sum of three Gaussians, $N_i e^{-\frac{1}{2}\left(\frac{x-\mu_i}{\sigma_i}\right)^2}$. Resolution and mean have been calculated with Gaussians $i = 1$ and $i = 3$. $\mathcal{L} = 60\,fb^{-1},\ m_A = 600\,GeV,\ \tan\beta = 100$.

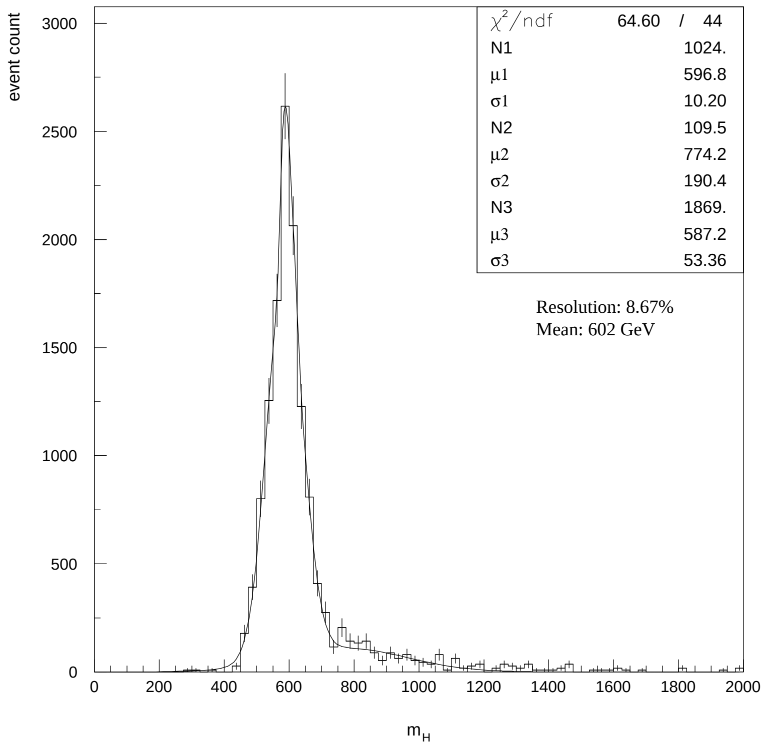

Figure 4.22: Reconstructed Higgs boson mass after jet energy scale correction and missing energy correction. The distribution is fitted by a sum of three Gaussians, $N_i e^{-\frac{1}{2}\left(\frac{x-\mu_i}{\sigma_i}\right)^2}$. Resolution and mean have been calculated with Gaussian $i = 1$ and $i = 3$. $\mathcal{L} = 60\, fb^{-1}$, $m_A = 600\, GeV$, $\tan\beta = 100$.

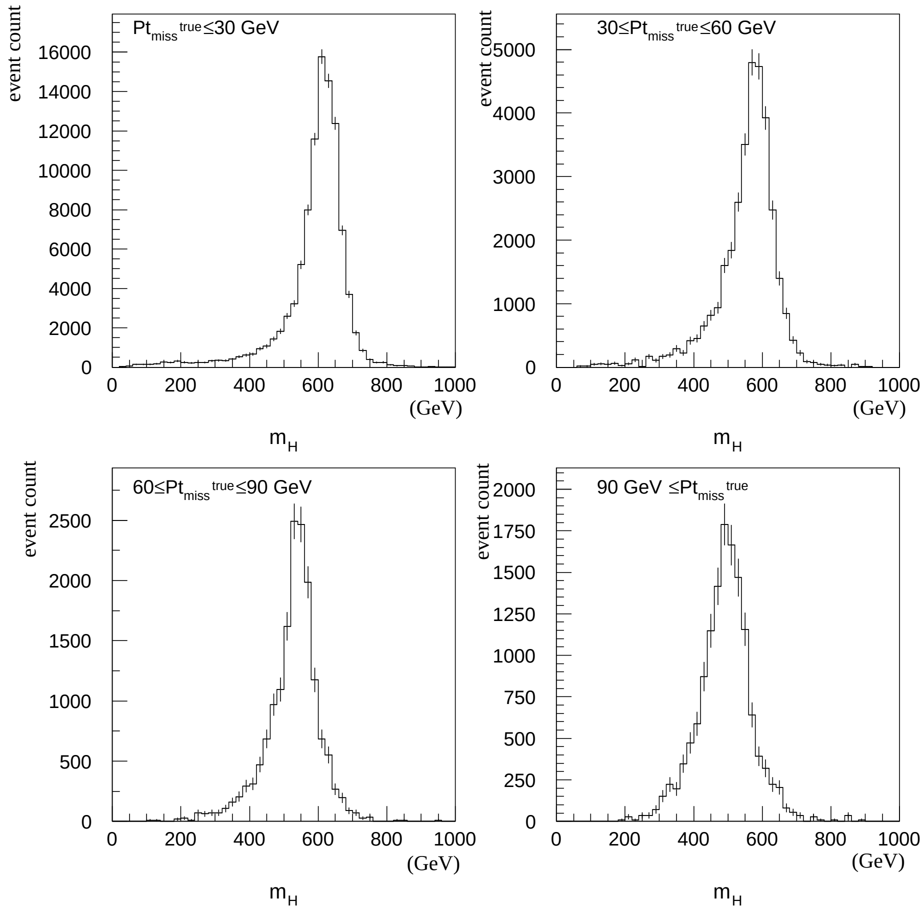

Figure 4.23: Effect of mising energy on reconstructed mass resolution. These plots represent the distribution of the invariant mass of the two jets coming from the Higgs boson decay according to the generation information (jets matched with partons) after different cuts on the true missing p_t (obtained from generation). The input A mass is $600\,GeV$. Final and initial state radiations have been switched off. No cut is applied except the requirement of having at least four jets. Jet energy scale correction has been applied while no missing energy correction has been applied.

same reason, the products of the Higgs boson decay will be hard. The signature of the process is:

2 soft b-jets + 2 hard b-jets,

the 2 hard jets coming from the Higgs boson decay and the 2 soft jets coming from the associated Higgs boson production mechanism $pp \to b\overline{b}H/A$. The kinematics will be treated in more details in section 4.4.3.

4.4.2 Generation of backgrounds

Backgrounds come mainly from QCD events. Events with four real-b jets will be classified as "irreducible". Other backgrounds are events with less than four b-jets but with some jets mistagged as b-jets. Backgrounds have been generated with Pythia 6.203 [91] in shower approximation from the $2 \to 2$ processes:

- $q_i q_j \to q_i q_j$
- $q_i \overline{q}_i \to q_k \overline{q}_k$
- $q_i \overline{q}_i \to gg$
- $q_i g \to q_i g$
- $gg \to q_k \overline{q}_k$
- $gg \to gg$

i, j, k indexes denoting the quark flavour. Irreducible backgrounds and reducible backgrounds were produced together including any QCD multijet background with a least four jets of any flavour.

We are aware that Pythia may underestimate the background cross-section because of the shower approximation . However it has been shown in [92] that for $t\overline{t}b\overline{b}$ events with,

- four b-quarks in the $|\eta| < 2.5$ region
- one b-quark of the top decay with a transverse momentum greater than $15\,GeV$
- two b-quarks coming from initial and final state radiation with $p_t > 30\,GeV$

Pythia was *overestimating* the cross section compared to CompHEP (initial and final state radiation included) by 6%. It is only when the transverse momentum cut on the b-quarks coming from initial and final state radiation are increased that Pythia underestimates the background. For instance when this cut is increased to $50\,GeV$, then the CompHEP cross-section is 1.19 times higher than Pythia one and for a $200\,GeV$ cut it is 6.73 times higher. Since we are requiring two hard b-jets and two other jets with a low p_t cuts ($20\,GeV$), we can expect that Pythia does not underestimate significantly the background. However a proper check with every background would be needed to be sure of this assertion.

The total cross-section of the background processes is very high. The generation of the backgrounds has been weighted (the weights depending on the transverse momentum in the center of frame of the main process, $\hat{p}_t$) in order to get a similar statistics in the whole relevant $\hat{p}_t$ range. In addition, a cut at $\hat{p}_t \geq 50\,GeV$ has been applied. Even with this Monte-Carlo generation optimisation, a lot of background events must be generated: about 150 million events were generated.

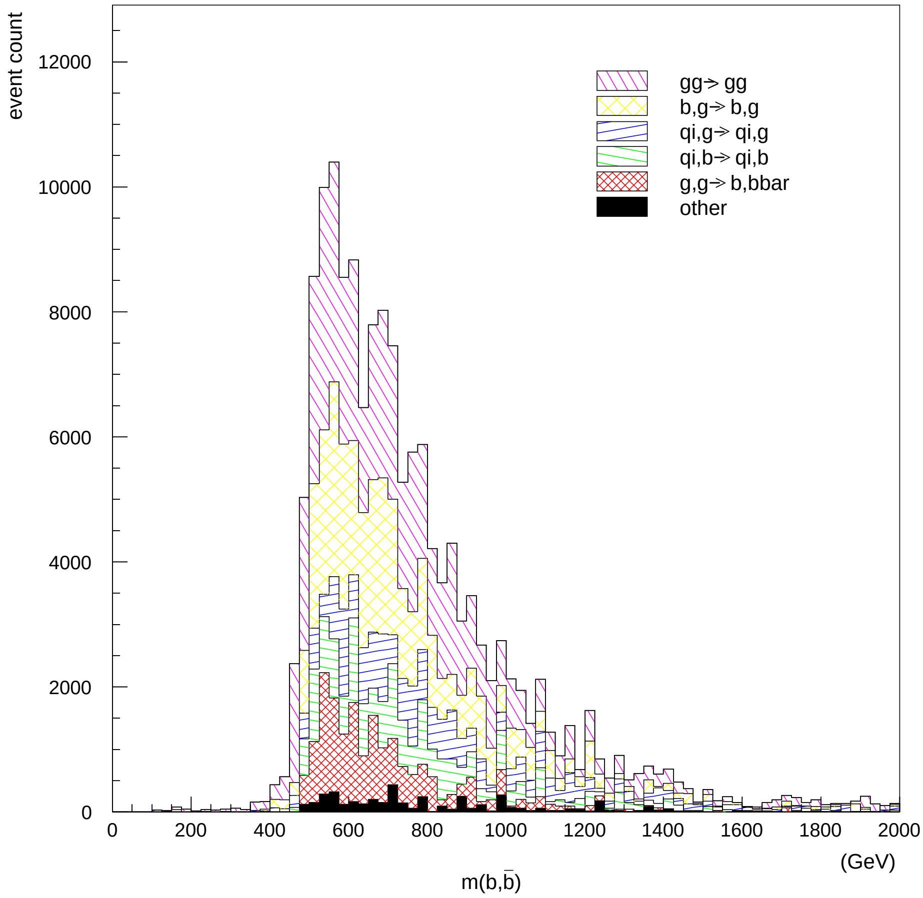

Figure 4.24: Composition of the background after all the selection cuts according to the various main $2 \to 2$ generation processes. The distribution of the mass of two highest-p_t jet system is shown. The QCD events with at least four jets of any flavor are included. $\mathcal{L} = 60\,fb^{-1}$.

Figure 4.24 shows the composition of the background surviving after the selection cuts according to the main $2 \to 2$ process. The main contributions come from $gg \to gg$, where the two final state gluons splits into $b\bar{b}$ pairs, and from $gb \to gb$. Figure 4.25 shows the composition of the background according to the number of *b*-jets. Here are considered jets that have been reconstructed from the detector response simulation. They are identified as *b*-jet by matching them with the *b*-partons of the generation with the procedure described in section 4.3.1. These histograms are obviously subject to matching errors. The reducible background with two or three *b*-jets is dominant.

4.4.3 Extracting the signal

As already said, the signature of the process is:

2 soft b-jets + 2 hard b-jets,

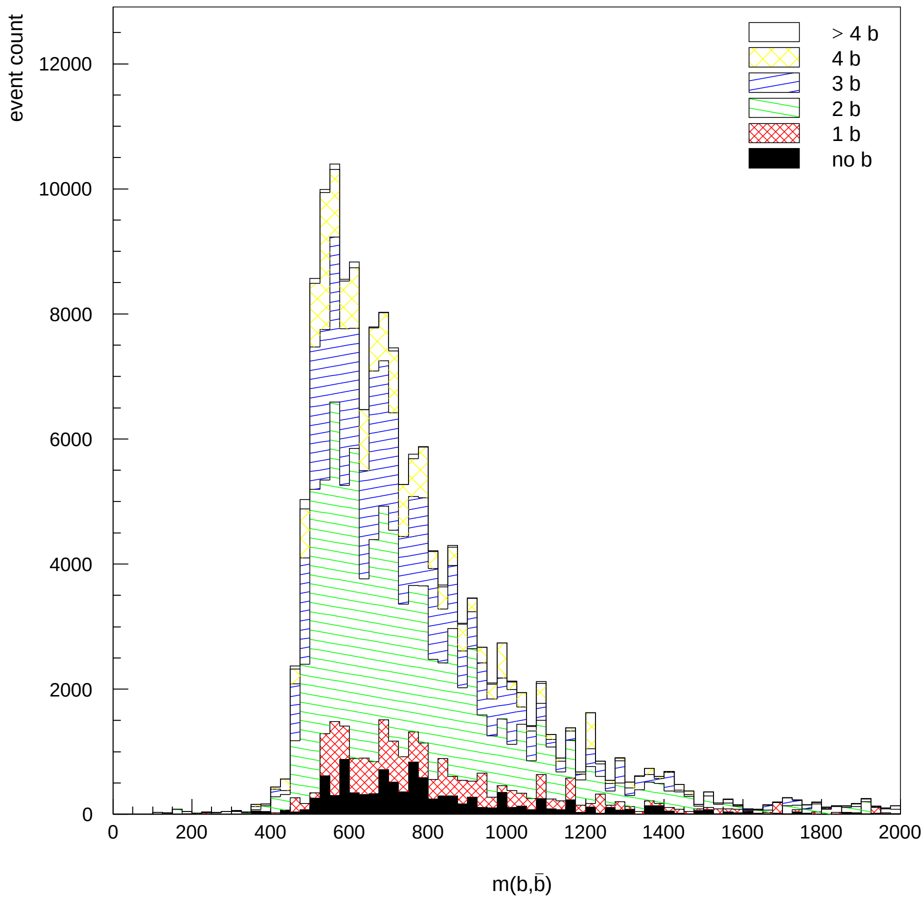

Figure 4.25: Composition of the backgrounds after all the selection cuts according to the number of b-jets. The distribution of the mass of two highest-p_t jet system is shown. $\mathcal{L} = 60\,fb^{-1}$.

with the 2 hardest jets coming from the Higgs boson decay and the 2 softest jets coming from the Higgs boson production.

At least three b-tagged jets are requested in the analysis. B-tagging of soft jets being less efficient than for hard jets, the b-tagging requirement of the former jets should be less stringent than for the latter. Tagging a third jet implicitly requires to have 4 jets in the event —but not necessarely in the *b*-tagging acceptance ($|\eta| < 2.4$)— since in QCD events b-jets are coming in pairs . Therefore tagging a 4^{th} jet will surely improve the tagging purity, but at the expense of statistics due to the acceptance and the tagging efficiency. Because the jets 3 and 4 are rather soft ($\langle E_t \rangle \simeq 30\,GeV$), the efficiency loss is too big and tagging a 4^{th} jets degrades the significance too much. Concerning the kinematics, hard P_t cuts must be applied to the two highest-p_t jets . Applying cuts on η on the hardest jets does not really help.

To fix ideas we will first look for a fixed Higgs boson mass, $m_A = 600\,GeV$, then we will deal with the full $m_A \in [300, 800\,GeV]$ mass range.

Kinematical cuts

The kinematics does not depend on $\tan\beta$.

Jet n will denote the n-th highest-P_t jet. Jet 1 and jet 2 are used to reconstruct the Higgs boson mass.

The cuts applied on the transverse momentum (corrected with scale correction and missing energy correction) of the four leading jets are:

- $P_{t_1} \geq 220\,GeV$
- $P_{t_2} \geq 220\,GeV$
- $P_{t_3} \geq 20\,GeV$
- $P_{t_4} \geq 20\,GeV$

These kinematical cuts reject the backgrounds by a factor $1.2 \cdot 10^7$, while 9.6% of signal passes the cuts. Table 4.4 summarises the effects of this selection. The samples used to calculate figures given in this table are statistically independent from the ones used to optimise the cuts. In that way these figures are not sensitive to statically insignificant features of the sample used to obtain the values of the cuts.

Selection	Signal acceptance (cumulative)	Background rejection (cumulative)	S/B (full mass range)	$S/\sqrt{B}$ in optimal mass window
none	100.00%	1	1.96e-10 ±8.1E-13	
At least 4 jets (Pt>10GeV) in the detector acceptance($\|\eta\| \leq 4.5$)	56.48% ±0.42%	4.28E+03 ±2.8E+02	4.73E-07 ±2.0E-09	1.57E+00 ±2.7E-01
Pt(jet1)>220GeV	36.29% ±0.31%	1.77E+06 ±4.8E+04	6.60E-05 ±1.6E-06	7.78E+00 ±2.2E-01
Pt(jet2)>220GeV	19.07% ±0.20%	5.97E+06 ±2.9E+05	1.12E-04 ±5.4E-06	8.73E+00 ±4.6E-01
Pt(jet3)>20GeV	18.10% ±0.19%	6.33E+06 ±3.2E+05	2.24E-04 ±1.3E-05	8.43E+00 ±4.5E-01
Pt(jet4)>20GeV	13.00% ±0.16%	8.33E+06 ±4.8E+05	2.12E-04 ±1.4E-05	6.70E+00 ±3.8E-01
deltaR(jet2,jet3)>1.	9.61% ±0.13%	1.21E+07 ±8.3E+05	2.27E-04 ±1.8E-05	5.89E+00 ±4.1E-01
jets to tag in tagging η acceptance	8.38% ±0.12%	1.77E+07 ±1.5E+06	2.90E-04 ±2.7E-05	6.66E+00 ±5.7E-01
b-tagging of 1 jet	5.11% ±0.09%	1.75E+08 ±4.5E+07	1.75E-03 ±4.8E-04	2.63E+01 ±1.4E+01
b-tagging of 2 jets	3.13% ±0.07%	3.06E+09 ±8.1E+07	1.87E-02 ±8.1E-04	2.78E+01 ±1.2E+00
b-tagging of 3 jets	1.45% ±0.04%	3.04E+10 ±1.0E+09	8.62E-02 ±5.1E-03	4.18E+01 ±2.7E+00
LV1 trigger	1.45% ±0.04%	3.04E+10 ±6.6E+08	5.37E-02 ±2.5E-03	4.18E+01 ±2.7E+00
HLT trigger	1.42% ±0.04%	3.06E+10 ±1.0E+09	8.49E-02 ±5.1E-03	4.09E+01 ±2.7E+00
without DR cut	1.70% ±0.05%	1.89E+10 ±4.8E+08	6.28E-02 ±3.0E-03	3.84E+01 ±2.0E+00

Table 4.4: Selection of the signal . These figures correspond to an integrated luminosity of 60 fb^{-1} at LHC and $m_A = 600\,GeV$, $\tan\beta = 100$.

B-tagging

Previous studies [2,93,94] were assuming a global b-tagging efficiency and mistagging probability independent of the transverse energy and of the pseudorapidity. This analysis uses a b-tagging counting algorithm based on track transverse impact parameters obtained from a fast simulation of the CMS tracker [95]

Figure 4.26 shows the tagging performance (from fast simulation) in the case of the topology of our channel and its backgrounds. We have focused our interest on the selection of the signal events and rejection of background events. Therefore the tagging efficiency for signal sample versus the mistagging probability for background samples was plotted (for the four highest-p_t jet). In our selection at least three b-tagged jets are required, but they are not necessarely the three highest-p_t jets: for instance it can be the two highest- p_t jets and the fourth highest-p_t one.

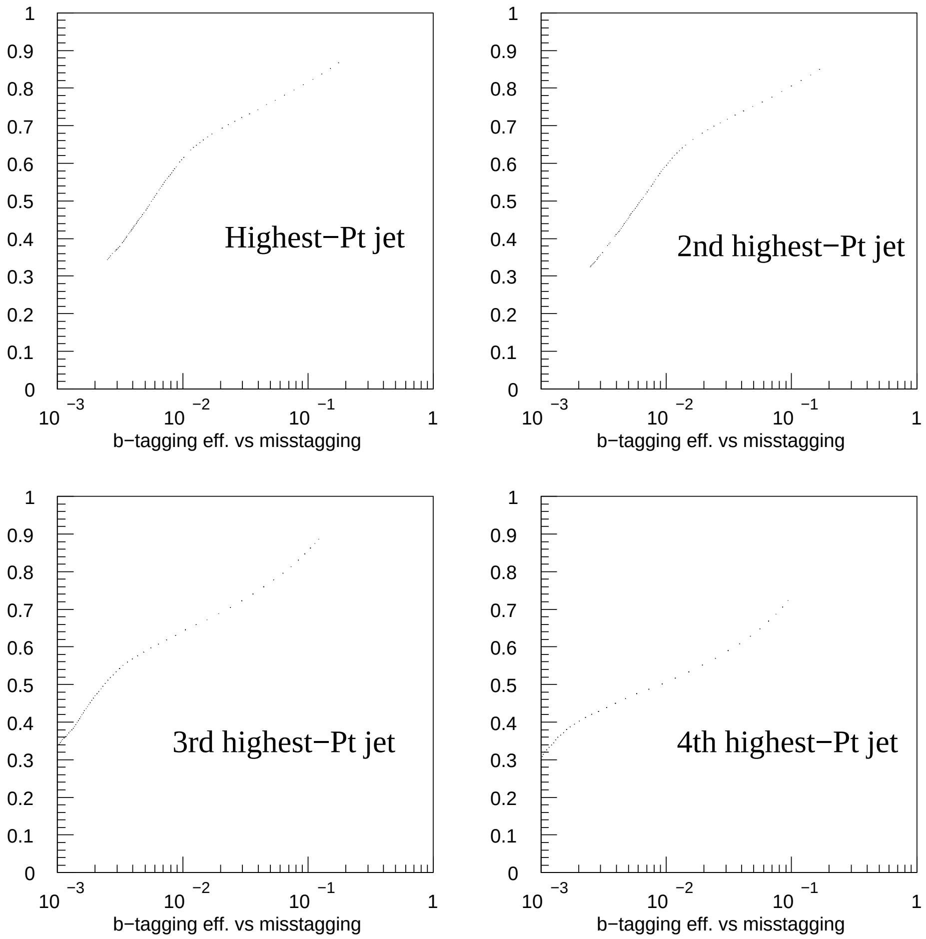

Figure 4.26: b-tagging performance for the four highest-p_t jets of the studied channel.

B-tagging rejects backgrounds by a factor 2500 and has signal efficiency of 15% (for a 600 GeV Higgs boson). The signal acceptance and background rejection can be found in table 4.4.

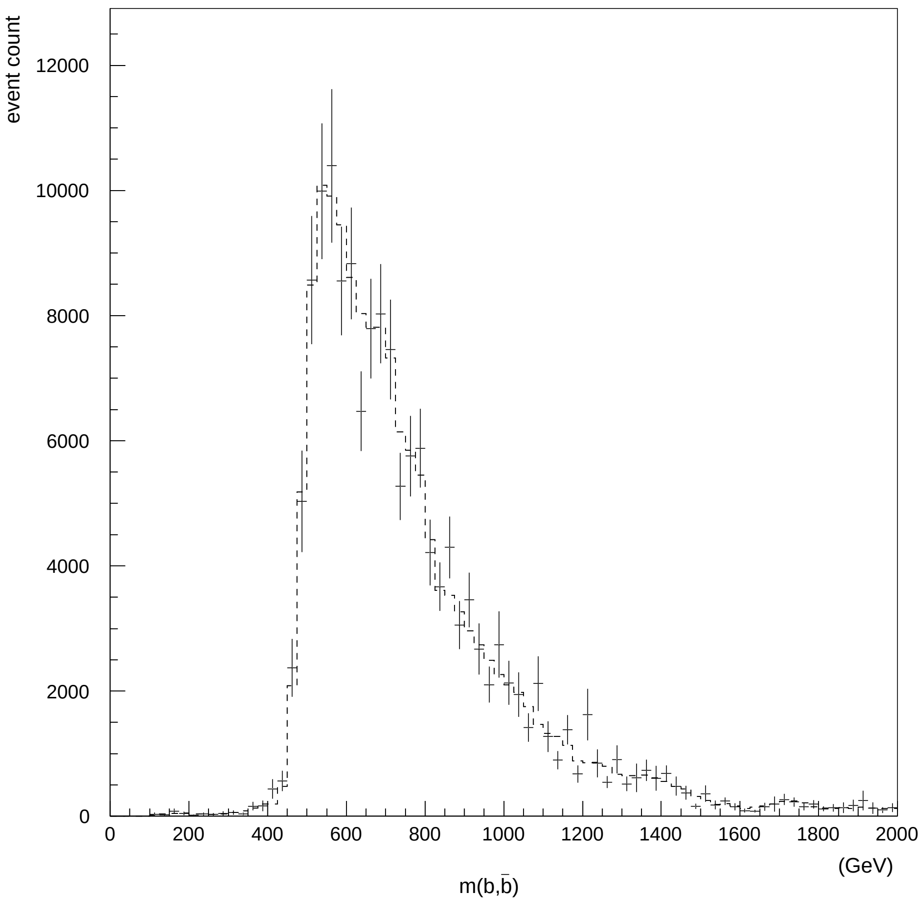

Figure 4.27: Mass distribution of the two highest-p_t jet system for the backgrounds and, in dashed line, smoothed parametrisation of the background shape.

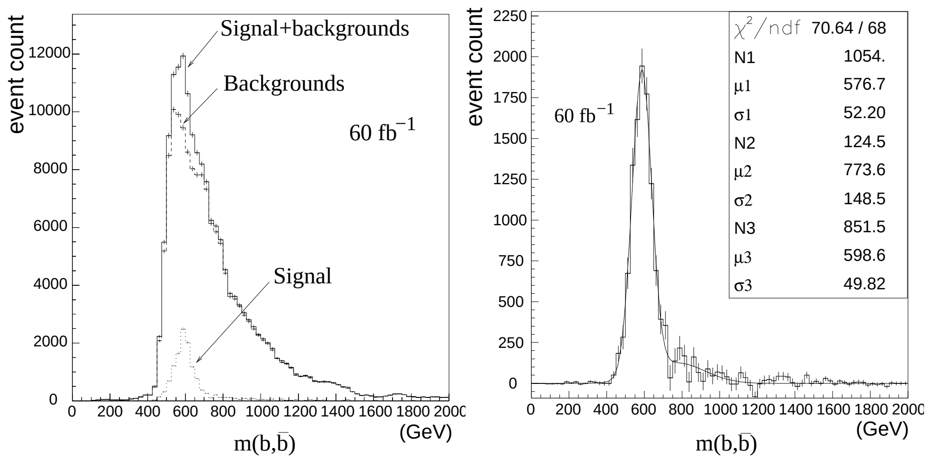

(a) Signal and background

(b) Signal after background substraction

Figure 4.28: Reconstructed Higgs boson mass for $m_A = 600\,GeV$, $\tan\beta = 100$. The event count corresponds to a $60\,fb^{-1}$ integrated luminosity. The fi gure on left shows the signal and the backgrounds. The fi gures on right shows the distribution of the signal (with the backgrounds) after subtraction of the background parametrisation. The right histogram has been fi tted with a sum of three Gaussians $N_i e^{-\frac{1}{2}\left(\frac{x-\mu_i}{\sigma_i}\right)^2}$.

	trigger efficiency			
mA	LV1		HLT	
300	33.2%	±0.3%	4.5%	±0.1%
400	68.9%	±0.5%	20.2%	±0.2%
600	87.5%	±0.6%	57.3%	±0.4%
800	91.8%	±0.6%	73.2%	±0.5%

Table 4.5: Trigger efficiency. HLT efficiency is given relative to the number of events passing the LV1 trigger.

Figure 4.28 shows the reconstructed Higgs boson mass distribution for signal and backgrounds. Since there is much less statistics in the Monte-Carlo simulation than what is expected for 3 years of low luminosity run, the reconstructed Higgs boson mass for the backgrounds has been parameterised: see figure 4.27. The background distribution of figure 4.28 has been generated according to this parametrisation. Statistics of signal and background distribution of figure 4.28 and the error bars corresponds to the expected statistics for a 60 fb^{-1} integrated luminosity.

4.4.4 Trigger efficiency

Trigger efficiencies of LV1 and HLT are shown for different assumptions on m_A in table 4.5. As it can be seen in table 4.6, the LV1 trigger has no effect on the significance. This is because LV1 threshold is superseded by the offline cuts. However for more sophisticate analysis where no sharp threshold is applied on the two leading jets it can have some effect.

The HLT is much more critical. This is due to the E_t threshold at $160\,GeV$ on the two leading jets. For masses below $\sim 400\,GeV$ this threshold just cuts off the mass distribution peak leaving only the upper tail. In general the b-tagging cuts at trigger level (HLT) are more safer than just E_t threshold cuts since they do not bias the mass distribution.

	no trigger constraints			LV1			HLT		
m_A	$S/\sqrt{B}$	S/B	$\tan\beta \mid S/\sqrt{B}=5$	$S/\sqrt{B}$	S/B	$\tan\beta \mid S/\sqrt{B}=5$	$S/\sqrt{B}$	S/B	$\tan\beta \mid S/\sqrt{B}=5$
300	167.6 $\pm$8.9	0.153 $\pm$.011	17.3	169.7 $\pm$8.8	0.158 $\pm$0.011	17.2	80.0 $\pm$6.8	0.141 $\pm$0.015	25.0
400	111.1 $\pm$7.6	0.275 $\pm$.028	21.2	111.1 $\pm$7.6	0.275 $\pm$0.028	21.2	96.5 $\pm$7.6	0.282 $\pm$0.033	22.8
600	41.8 $\pm$2.7	0.190 $\pm$0.019	34.6	41.8 $\pm$2.7	0.190 $\pm$0.019	34.6	40.9 $\pm$2.7	0.186 $\pm$0.019	35.0
800	16.6 $\pm$0.9	0.103 $\pm$0.009	54.8	16.6 $\pm$0.9	0.103 $\pm$0.009	54.8	16.6 $\pm$0.9	0.103 $\pm$0.09	54.8

Table 4.6: Effect of trigger efficiency on signal significance. $\tan\beta$ corresponds to $tan\beta = 100$. The $\tan\beta$ value giving a $5\cdot\sigma$ signal significance is also given. The signal significane is calulated within the mass window which optimizes it. The S/B ratio is calculated within this mass window.

A $5 \cdot \sigma$ significance is required to claim a discovery. Let's look for which $(m_A, \tan\beta)$ region we can get such a significance.

Conclusions

Figure 4.29 shows the $5 \cdot \sigma$ significance contour which was obtained for the $pp \rightarrow \phi bb \rightarrow bbbb, \phi = A, H$ channel. The uncertainties on the cross-section of the signal and of the backgrounds are rather large and the radiative corrections have a big effect on the signal cross-section [32]. Therefore it is hard to have a strong conclusion on the expected significance at this stage.

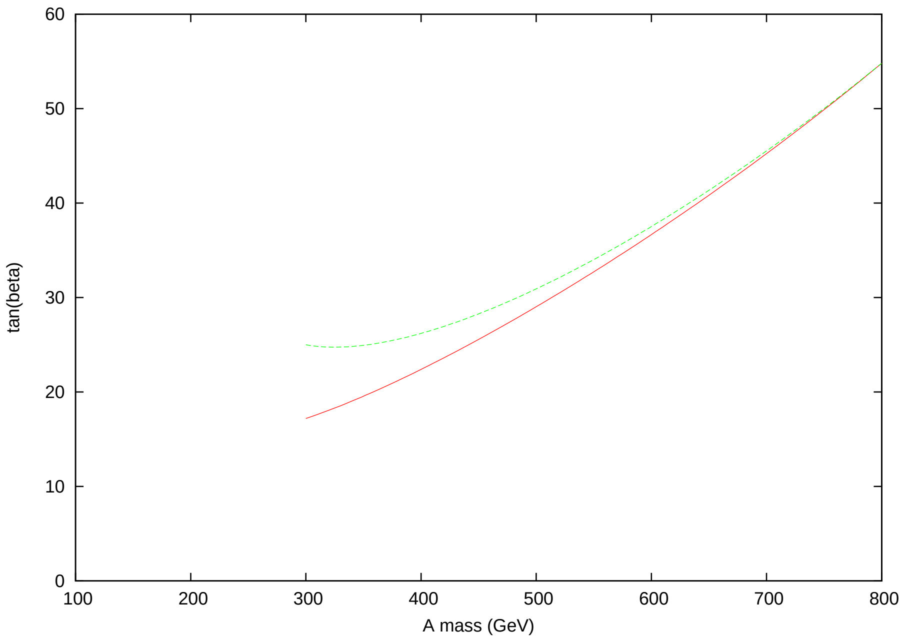

Figure 4.29: MSSM Higgs boson discovery contour for the process $pp \rightarrow b\bar{b}H/A$ with $H/A \rightarrow b\bar{b}$. The significance is greater than $5 \cdot \sigma$ for the region above the curves. The solid curve is assuming a 100% efficient HLT , while the dashed one takes into account the HLT.

Every QCD multi-jet backgrounds with at least four jets, of any flavour, have been taken into account. However the backgrounds have been generated in shower approximation from $2 \rightarrow 2$ processes, the other jets coming from the initial and final state radiations. In the future, more sophisticated Monte-Carlo generators producing the four jets with a full matrix calculation, like ALPGEN [96], should be used.

The $5 \cdot \sigma$ signal significance contour given in figure 4.29 assumes a perfect knowledge of the background shape. We will certainly not have this knowledge, especially in the first years of run, and therefore the limiting quantity will not be the statitics but the S/N ratio: at $600\,GeV$ mass at the $5 \cdot \sigma$ limit ($\tan\beta = 35$) the S/N ratio is only 1.04%. Moreover the signal is located at the maximum of the background distribution as a consequence of the background suppression kinematical cuts. For those reasons, a very good understanding of the backgrounds will be needed to exploit this channel and the $5 \cdot \sigma$ contour shown in figure 4.29 will be rather shrink once the background uncertainties will be included.

The results which are obtained for this channel are less conclusive than the ones for the $A/H \to \tau\tau$ mode, which is more promising in the relevant $(m_A, \tan\beta)$ region as the backgrounds to $b\bar{b}H/A \to b\bar{b}\tau^+\tau^-$ are smaller and much easier to reduce and control. However this four-b channel can be a cross-check for the discovery once it is known which Higgs boson masses must be looked at. It could also be used in combination with the $\tau\tau$ mode to calculate the coupling of the Higgs with the $b\bar{b}$ pair or get the relative $A/H \to \tau\tau$ branching ratio.

Recent calculations [97] lead to a cross-section of the process $gb \to Hb$ an order of magnitude higher than the cross-section of the $gg \to Hbb$ process. Thus, the three b-final state channel might be an alternative to the one studied here although backgrounds with three jets must be much more important than with four jets.

Conclusions

Two aspects of the CMS experiment were covered in this thesis: the Front-End electronics configuration and the observability of the *A*/*H* Higgs bosons in the four-*b* final state.

A Front-End electronics configuration system for the CMS subdetectors was developed and was tested with great success. It has been integrated in the DCS framework, but can be also easily adapted for use within another framework as the Run Control and Monitoring System.

The study of the observability of the *A*/*H* Higgs in four-*b* final state pointed out the importance of an efficient *b*-tagging with a low mistagging probability and of an accurate jet reconstruction. The irreducible backgrounds —events with four *b*-jets— represent only 12% of the backgrounds which pass all selection cuts. 72% of the backgrounds have one or two mistagged jets.

For a pseudoscalar Higgs mass $m_A = 400\,GeV$, a significance of at least $5 \cdot \sigma$ is expected for $\tan\beta > 25$ (trigger efficiency included). The significance diminishes with the *A* mass because of the cross-section decrease: for $m_A = 600\,GeV$, a $5 \cdot \sigma$ significance is reached for $\tan\beta = 35$. Those significances include only statistical errors. For $m_A = 600\,GeV$ and $\tan\beta = 35$ —corresponding to a significance of $5 \cdot \sigma$— the signal over backgrounds ratio S/N is only 1.04% . Therefore, this study lead to the conclusion that this channel does not extend the $(m_A, \tan\beta)$ discovery region already covered by the $H/A \rightarrow \tau\tau$ mode.

The four-*b* channel can still be used as a confirmation in case of a Higgs discovery at high $\tan\beta$ value ($\tan\beta \gtrsim 25$) and also to calculate, in combination with the $\tau\tau$ channel, the *A*/*H* Higgs boson coupling with $b\bar{b}$ pairs.

List of Figures

Bibliography

[1] J. F. Gunion, H. E. Haber, F. E. Paige, W.-K. Tung, and S. S. D. Willenbrock, "Neutral and charged Higgs detection: heavy quark fusion, top quark mass dependence and rare decays," *Nucl. Phys.* **B294** (1987) 621.

[2] J. Dai, J. F. Gunion, and R. Vega, "Detection of neutral MSSM Higgs bosons in four-b final states at the Tevatron and the LHC: An update," *Phys. Lett.* **B387** (1996) 801–803, `hep-ph/9607379`.

[3] H. Muirhead, *The Physics of elementary particles*. Pergamon Press, 1965.

[4] "Noether, Amalie Emmy," in *Britannica Student Encyclopedia 2003 Encyclopædia Britannica Online*. Feb. 18, 2003. `<http://search.eb.com/ebi/article?eu=337119>`.

[5] J. F. Cornwell, *Group theory in physics. An introduction*. Academics Press. Harcourt Brace & Co, Publishers, 1997.

[6] S. Sternberg, *Group theory and physics*. Cambridge – University Press, 1994.

[7] "Lagrange, Joseph-Louis," in *Britannica Student Encyclopedia 2003 Encyclopædia Britannica Online*. 18 Feb, 2003. `<http://search.eb.com/ebi/article?eu=297324>`.

[8] C.-N. Yang and R. L. Mills, "Conservation of isotopic spin and isotopic gauge invariance," *Phys. Rev.* **96** (1954) 191–195.

[9] F. Halzen and A. D. Martin, *Quarks and leptons*. John Wiley and sons, 1984.

[10] A. Salam and J. C. Ward, "Electromagnetic and weak interactions," *Phys. Lett.* **13** (1964) 168–171.

[11] S. Weinberg, "A model of leptons," *Phys. Rev. Lett.* **19** (1967) 1264–1266.

[12] S. L. Glashow, "Partial symmetries of weak interactions," *Nucl. Phys.* **22** (1961) 579–588.

[13] J. Goldstone, "Field theories with 'superconductor' solutions," *Nuovo Cim.* **19** (1961) 154–164.

[14] J. Goldstone, A. Salam, and S. Weinberg, "Broken symmetries," *Phys. Rev.* **127** (1962) 965–970.

[15] P. W. Higgs, "Broken symmetries, massless particles and gauge fields," *Phys. Lett.* **12** (1964) 132–133.

[16] P. W. Higgs, "Broken symmetries and the masses of gauge bosons," *Phys. Rev. Lett.* **13** (1964) 508–509.

[17] P. W. Higgs, "Spontaneous symmetry breakdown without massless bosons," *Phys. Rev.* **145** (1966) 1156–1163.

[18] Q. Ho-King and P. X. Yem, *Elementary particles and their interactions*. Springer, 1998.

[19] N. Cabibbo, "Unitary symmetry and leptonic decays," *Phys. Rev. Lett.* **10** (1963) 531–532.

[20] N. Cabibbo and L. Maiani, "Origin of the weak-interaction angle. II," *Phys. Rev.* **D1** (1970) 707–718.

[21] M. Kobayashi and T. Maskawa, "CP violation in the renormalizable theory of weak interaction," *Prog. Theor. Phys.* **49** (1973) 652–657.

[22] P. X. Y. Ho Kim Quang, *Elementary particles and their interactions : concepts and phenomena*. Berlin: Springer, 1998.

[23] M. Carena, "The Standard Model and beyond: the Minimal SUSY extension." Fermilab academics lecture. `http://fnth37.fnal.gov/carena/`, May-June, 2001.

[24] J. Wess and B. Zumino, "Supergauge transformations in four-dimensions," *Nucl. Phys.* **B70** (1974) 39–50.

[25] J. Wess and J. Bagger, *Supersymmetry and Supergravity*. Princeton Series in Physics. Princeton University Press, 1983.

[26] Y. A. Golfand and E. P. Likhtman, "Extension of the algebra of Poincaré group generators and violation of P invariance," *JETP Lett.* **13** (1971) 323–326.

[27] A. Salam and J. Strathdee, "Supergauge transformations," *Nucl. Phys.* **B76** (1974) 477–482.

[28] S. Ferrara, J. Wess, and B. Zumino, "Supergauge multiplets and Superfi elds," *Phys. Lett.* **B51** (1974) 239.

[29] S. Ferrara and B. Zumino, "Supergauge invariant Yang-Mills theories," *Nucl. Phys.* **B79** (1974) 413.

[30] J. Wess and B. Zumino, "Supergauge invariant extension of Quantum Electrodynamics," *Nucl. Phys.* **B78** (1974) 1.

[31] **Higgs Working Group** Collaboration, M. Carena *et al.*, "Report of the Tevatron Higgs working group," `hep-ph/0010338`.

[32] M. Carena and H. E. Haber, "Higgs boson theory and phenomenology," *Prog. Part. Nucl. Phys.* **50** (2003) 63–152, `hep-ph/0208209`.

[33] J. F. Gunion, H. E. Haber, G. L. Kane, and S. Dawson, "The Higgs hunter's guide,". SCIPP-89/13.

[34] H. E. Haber and Y. Nir, “The decay $Z \to A^0A^0$ neutrino anti-neutrino and $e^+e^- \to A^0A^0Z$ in two Higgs doublet models,” *Phys. Lett.* **B306** (1993) 327–334, hep-ph/9302228.

[35] T. Hambye and K. Riesselmann, “Matching conditions and Higgs mass upper bounds revisited,” *Phys. Rev.* **D55** (1997) 7255–7262, hep-ph/9610272.

[36] LEP electroweak Higgs working group, “Status of Winter 2003,” http://www.cern.ch/lepewwg. LEPEWWG/2003-01 (April 2003).

[37] ALEPH, DELPHI, L3 and OPAL collaborations, The LEP working group for Higgs boson searches, “Search for the Standard Model Higgs boson at LEP,”. ALEPH 2002-024 CONF 2002-013, DELPHI 2002-088-CONF-621 L# Note TN721, LHWG Note/2002-01.

[38] M. Spira, “MSSM Higgs boson production at the LHC,” hep-ph/9711407.

[39] V. Drollinger, *Reconstruction and analysis methods for searches of Higgs bosons in the decay mode* $H^0 \to b\bar{b}$ *at hadron colliders*. PhD thesis, University of Karlsruhe, 2001.

[40] M. Spira, “QCD effects in Higgs physics,” *Fortsch. Phys.* **46** (1998) 203–284, hep-ph/9705337.

[41] R. Kinnunen, “Higgs physics at the LHC,” in *Hamburg 2002, Supersymmetry and unification of fundamental interactions. Conf. proceedings, vol. 1* 26-41*, Helsinki Inst. of Phys. Jun, 2002.

[42] S. Abdullin *et al.*, “Summary of the CMS discovery potential for the Higgs boson,” tech. rep., CERN, 2003.

[43] S. Lethi, *Prospects for the Detection of Neutral MSSM Higgs bosons Decaying into Tau Leptons in the CMS Detector*. PhD thesis, University of Helsinki, 2001. Report Series in Physics, HU-P-D93.

[44] R. Kinnunen and D. Denegri, “Study of $H,A \to \tau\tau \to h^{\pm} + h^{\pm} + X$ in CMS.” CMS NOTE 1999/037, 1990.

[45] R. Kinnunen and A. Nikitenko, “Study of $H,A \to \tau\tau \to l + \tau\text{jet} + E_T^{miss}$.” CMS NOTE 1997/106, 1997.

[46] Bellucci, *MSSM neutral Higgs boson searches at CMS in the* $\mu\mu$ *channel*. PhD thesis, Universita degli studi di Firenze, December, 2001.

[47] M. Bisset, F. Moortgat, and S. Moretti, “Triplepton + top signal from chargino-neutralino decays of MSSM charged Higgs bosons at the LHC.” CMS NOTE 2003/004, 2003.

[48] F. Moortgat, “Observability of MSSM Higgs bosons decaying to sparticles at the LHC.” presented at the 36th Rencontres de Morions, QCD and High Energy hadronic interactions, Les Arcs, France, 2001.

[49] S. Abdullin, D. Denegri, and F. Moortgat, “Observability of MSSM Higgs bosons via sparticle decay modes in CMS.” CMS NOTE 2001/042, 2001.

[50] R. Kinnunen and A. Nikitenko, “Study of $h \to \tau\tau$ with hadronic tau decays in CMS.” 2003.

[51] **CMS** Collaboration, “CMS TDR 5,” Tech. Rep. CERN/LHCC 98-6, CERN, 1998.

[52] **CMS** Collaboration, “Addendum to the CMS tracker TDR,” Tech. Rep. CMS/2000-006, CERN/LHCC 2000-016, CERN, 2000.

[53] **CMS** Collaboration, “CMS TDR 4,” Tech. Rep. CERN/LHCC 97-33, CERN, 1997.

[54] J.-L. Faure, *CMS Electromagnetic calorimeter parameters*. `https://edms.cern.ch/file/109171/1/poster-gen-a4.pdf`.

[55] **CMS** Collaboration, “CMS TDR 2,” Tech. Rep. CERN/LHCC 97-31, CERN, 1997.

[56] A. H. Walenta, J. Heintze, and B. Schürlein, “The multiwire drift chamber, a new type of proportional wire chamber,” *Nuclear Instruments and Methods* **92** (1971), no. 3, 373–380.

[57] F. Sauli, “Principles of operation of multiwire proportional and drift chambers,”. CERN-77-09.

[58] G. Charpak and F. Sauli, “Multiwire proportional chambers and drift chambers,” *Nucl. Instrum. Meth.* **162** (1979) 405–428.

[59] **CMS** Collaboration, “CMS TDR 3,” Tech. Rep. CERN/LHCC 98-6, CERN, 1997.

[60] R. Bouclier, G. Charpak, and F. Sauli, “Parallel plate proportional counters for relativistic particles,”. Presented at ECFA Study Week on the 300-GeV Accelerator, Tirrenia, Italy, Sep 13-18, 1971.

[61] **CMS** Collaboration, “CMS TDR 6.2,” Tech. Rep. CERN/LHCC 2002-26, CERN, 2002.

[62] “Report from the working group on common projects in the fi eld of software/computing and trigger/DAQ at LHC,” 12 Dec, 1997. `http://itco.web.cern.ch/itco/Projects-Services/JCOP/-JcopDocuments/thursdayprop.html`.

[63] D. Myers, “LHC experiments – Joint controls project initial project plan,” Jan., 27, 1998. `http://itco.web.cern.ch/itco/Projects-Services/JCOP/-JcopDocuments/initialPP.html`.

[64] “The LHC experiments’ Joint Controls Project, JCOP,” in *ICALEPS 1999 proceedings*. 1999.

[65] JCOP, “LHC experiments’ Joint Controls Project revised mandate,” tech. rep., CERN, 22 Feb., 2000. CERN-JCOP-2000-001 `http://itco.web.cern.ch/-itco/Projects-Services/JCOP/JcopDocuments/revisedmandate4.pdf`.

[66] P. Gras, “A PVSS-Java interface.” `http://www.cern.ch/pgras/pvssjava`.

[67] "The Gamma Irradiation Facility." http://www.cern.ch/ESS/GIFProject/index.html.

[68] "LHC Alarm SERvice (laser) project." http://www.cern.ch/proj-laser.

[69] G. Hall, "The deconvolution method of pulse shaping." http://cmstrackercontrol.web.cern.ch/CMSTrackerControl/-documents/Geoff/Deconvolution_summary.pdf.

[70] C. Gaspar and M. Donszelmann, "DIM: a distributed information management system for the DELPHI experiment at CERN,". Prepared for 8th Real-Time Computer Applications in Nuclear, Particle and Plasma Physics (RT 93), Vancouver, British Columbia, Canada, 8-11 Jun 1993.

[71] C. Gaspar, "DIM." http://www.cern.ch/dim.

[72] D. Rainwater, M. Spira, and D. Zeppenfeld, "Higgs boson production at hadron colliders: Signal and background processes," hep-ph/0203187.

[73] M. Carena, "MSSM Higgs boson phenomenology at the Tevatron collider." CERN-TH/98-262, FERMILAB-PUB-98/250-T, 1998.

[74] D. A. Dicus and S. Willenbrock, "Higgs boson production from heavy quark fusion," *Phys. Rev.* **D39** (1989) 751.

[75] D. Dicus, T. Stelzer, Z. Sullivan, and S. Willenbrock, "Higgs boson production in association with bottom quarks at next-to-leading order," *Phys. Rev.* **D59** (1999) 094016, hep-ph/9811492.

[76] F. Maltoni, Z. Sullivan, and S. Willenbrock, "Higgs-boson production via bottom-quark fusion," hep-ph/0301033.

[77] R. V. Harlander and W. B. Kilgore, "Higgs boson production in bottom quark fusion at next-to-next-to-leading order," hep-ph/0304035.

[78] M. Spira, "Higgs and SUSY particle production at hadron colliders," hep-ph/0211145.

[79] M. Spira, "hqq, $qq, gg \to h, a + qq$ LO cross section calculation,". Code available at http://www.desy.de/~spira.

[80] D. Denegri, V. Drollinger, R. Kinnunen, K. Lassila-Perini, S. Lehti, F. Moortgat, A. Nikitenko, S. Slabospitsky, and N. Stepanov, "Summary of the CMS discovery potential for the MSSM SUSY Higgses," *CMS note* (Nov, 2001). CMS NOTE 2001/032.

[81] A. Djouadi, J. Kalinowski, and M. Spira, "HDECAY: A program for Higgs boson decays in the standard model and its supersymmetric extension," *Comput. Phys. Commun.* **108** (1998) 56–74, hep-ph/9704448.

[82] A. Djouadi, "Impact of the SUSY decays on the search for the MSSM Higgs bosons at the LHC," *Mod. Phys. Lett.* **A14** (1999) 359–368, hep-ph/9903382.

[83] S. Abdullin, "CMSJET,". CMS TN/94-180.

[84] CMS detector simulation software group, *CMS simulation package CMSIM*. `http://cmsdoc.cern.ch/cmsim/cmsim.html`.

[85] Application software – group computing and network division – CERN, *Geant, detector description and simulation tool*. CERN program library long writeup W5013.

[86] B. Flaugher and K. Meier, "A compilation of jet fi nding algorithms,". Publ. in Proc. of DPF Summer study on high energy physics, research directions for the Decade, Snowmass, CO, Jun 25 - Jul 13, 1990. Ed. by Edmond L. Berger. Publ. by World Scientifi c (1992). 808 p.

[87] **UA1** Collaboration, G. Arnison *et al.*, "Hadronic jet production at the CERN proton - anti-proton collider," *Phys. Lett.* **B132** (1983) 214.

[88] **Particle Data Group** Collaboration, K. Hagiwara *et al.*, "Review of particle physics," *Phys. Rev.* **D66** (2002) 010001.

[89] R. Kinnunen and D. Denegri, "B-tagging with impact parameter in the CMS tracker," in *Proceedings of 31st annual conference of the Finnish Physical Society, Helsinki, Finland*. March, 1997.

[90] V. Drollinger, V. Karimaki, S. Lethi, N. Stepanov, and A. Khanov, "Upgrade of the fast Tracker response simulation, the FATSIM utility," Tech. Rep. CMS IN 2000/034, CMS, 2000.

[91] T. Sjostrand, L. Lonnblad, and S. Mrenna, "PYTHIA 6.2: Physics and manual," `hep-ph/0108264`.

[92] D. Cavalli *et al.*, "The Higgs working group: Summary report," `hep-ph/0203056`.

[93] **ATLAS** Collaboration, "ATLAS TDR 15," Tech. Rep. CERN/LHCC/99-15, CERN, May 25, 1999.

[94] E. Richter-Was and D. Froidevaux, "MSSM Higgs searches in multi-b-jet fi nal states at the LHC," *Z. Phys.* **C76** (1997) 665–676, `hep-ph/9708455`.

[95] V. Drollinger, V. Karimaki, S. Lehti, S. N., and K. A., "Upgrade of Fast Tracker Response Simulation, the FATSIM utilisty." 2000.

[96] M. L. Mangano, M. Moretti, F. Piccinini, R. Pittau, and A. D. Polosa, "ALPGEN, a generator for hard multiparton processes in hadronic collisions," `hep-ph/0206293`.

[97] J. Campbell, R. K. Ellis, F. Maltoni, and S. Willenbrock, "Higgs boson production in association with a single bottom quark," `hep-ph/0204093`.

Acknowledgments

This thesis could not have been completed without the assistance of a large number of people. First and foremost, thanks are due to my thesis supervisor, Thomas Müller, who always backed me up and let me free to organise my research as I wished. Many thanks to Sergio Cittolin who made me part of his group for the first two years as part of the CERN Doctoral Student program. I have really enjoyed working in his group and I take this opportunity to thank all my colleagues of the CERN CMD group for their kindness.

I am very grateful for the tremendous help my CERN supervisor, Wolfgang Funk, has always afforded me. Many thanks also to Christian Weiser for his guidance and advice in my physics analysis work. Many thanks, Christian, for the help you have provided me throughout my analysis and for the time you spent in carefully checking through my manuscript. Your reading allowed me to improve the quality of my dissertation.

I express all my gratitude to Daniel Denegri for his time and help with my analysis, and the care he took in reading my manuscript. Many thanks, Daniel, for your encouragement in my physics analysis. Thanks a lot for having agreed to be my "Korreferent".

I would also like to express special thanks to Volker Drollinger. He was the one who first introduced me to the World of Pythia and CMSJET. He gave me precious advice throughout my analysis. Thanks to Günter Quast for the advice he gave me and for his many encouragements while I was writing my dissertation.

I thank the Tracker group people I worked with and with whom I spent a great time: Patrice Siegrist, Frédéric Drouhin, Laurent Gross, Laurent Mirabito, Nancy Marinelli, Andromachi Tsirou, Piero Giorgio Verdini, Damien Vintache.

I also thank Abdelhak Djouadi, Michelangelo Mangano, Torbjörn Sjöstrand and Michael Spira for the help they provided me in understanding the phenomenology of the physics channel I studied.

Many thanks to everyone who has helped me in the course of this work: Salavat Abdullin, Paul Burkimsher, Eric Cano, Mike Clayton, Jim Cook, Mikhail Dubinin, Clara Gaspar, Frank Glege, Manuel Gonzalez Berges, Ritva Kinnunen, Hervé Milcent, Filip Moortgart, Steve Murray, Alexandre Nikitenko, Klaus Rabbertz, Marcel Stanitzki, Nikita Stepanov, Wayne Salter, Paris Sphicas. Finally, thank you to everyone who helped me in some way and whose name is not mentioned here.

I am very grateful to my family and to all of my friends for their support during all this time.